TEM STUDY OF NANOSTRUCTURED COLD CATHODE DIAMOND FIELD EMITTER TIPS

By

Travis Charles Wade

Dissertation

Submitted to the Faculty of the

Graduate School of Vanderbilt University

in partial fulfillment of the requirements

for the degree of

DOCTOR OF PHILOSOPHY

in

Interdisciplinary Material Science

December, 2011

Nashville, Tennessee

Approved:

Professor Norman H. Tolk

Professor Jim L. Davidson

Professor Charles M Lukehart

Professor Greg Walker

Professor Weng P. Kang

Professor Kalman Varga

TABLE OF CONTENTS

LIST OF FIGURES

LIST OF TABLES

ACKNOWLEDGMENTS

Generous financial support was provided by the National Science Foundation's Integrative Graduate Education and Research Traineeship (IGERT) program. Without the salary support and travel funds provided, I likely would not have discovered the research collaborators that were so essential to the success of this investigation. The administrative staff and Sarah Satterwhite in particular, have gone to great lengths to ensure that resources were always available to support me and to keep me abreast up new opportunities. My efforts have been funded by the US Department of Defense Extreme Light Source program in collaboration with the University of Florida. Following that, the Army Research Office (ARO) provided support.

The Davidson and Kang research labs at Vanderbilt provided all the materials studied in this work and could not have been done without them. The decades of diamond growing experience and the established production lines in place enabled a never ceasing supply of new material to study.p

I am thankful for the ongoing collaboration with Oak Ridge National Laboratory enabling access to state of the art Transmission Electron Microscopy (TEM) and Focused Ion Beam (FIB) facilities via the SHaRE program. Research at the SHaRE User Facility is supported by the Scientific User Facilities Division, Office of Basic Energy Sciences, U.S. Department of Energy, under Contract DE-AC05-00OR22725 with UT-Battelle, LLC. Support at ORNL has been generously provided by Dr. Larry Allard, Dr. Kinga Unocic, Dr. Jim Bentley, and Dorothy Coffey. Kinga in particular has been remarkably selfless in her willingness to work long and odd hours to get results. Collaboration with Oak Ridge National Lab scientists has been supported by the SHaRE facility funded by the Scientific User Facilities Division, Office of Basic Energy Sciences, U.S. Department of Energy.

The entire research direction of transmission electron microscopy has been supported and guided by Professor James Wittig. His experience with interpretation of results and willingness to share precious instrument time dramatically enhanced the scope and accuracy of this work. The professional connections introduced to me by Dr. Wittig will undoubtedly serve for years to come.

I would like to thank Dr. William Hofmeister and Dr. Lino Costa at the University of Tennessee Space Institute for assistance in exploring alternative methods for removal of array tips from the substrate. Although we did not meet with success by their laser etching methods, the generosity and skill of these scientists furthered my own creativity and motivation as well as teaching me about new tools and methods.

Research into the electron emission from tips performed by Dr. Charlie Brau and Dr. Jonathan Jarvis has been enlightening and informative. Complementing my study of the emitter's physical structure, their study of the electron beam dynamics completes the "holistic" study of these diamond field emission tips. Collaboration with them has been a constant source of inspiration and direction.

I owe great credit to my supportive wife, Ellin, without whom this dissertation would have taken a great deal longer to complete. I owe her a great debt for her willingness to accept the tasks that I neglect in favor of my work, as well as her instrumental part in caring for our son, Mason.

Editorial assistance has been graciously provided by my colleagues Stephanie Gilbert, Justin Gregory, and Ian McFadden.

I have enjoyed the rare opportunity to have two fine advisors, Dr. Jim Davidson and Dr. Norman Tolk, who complement each other well and have formed an effective and balanced collaboration. Dr. Davidson's efforts to teach me persuasive speaking and the art of "word-smithing" will serve me well for a long time to come. He has been always a teacher of the unspoken ways in which people work together and how we should carry ourselves. Dr. Tolk's model of fervent dedication and a balanced life provide me the inspiration to follow in his footsteps to the best of my ability.

CHAPTER 1

INTRODUCTION

Although diamond has proven to be an excellent electron field emitter with orders of magnitude more current at lower fields than competing technologies, fabrication yield of ultra-sharp diamond pyramidal tips (~5nm tip radius) has been a persistent issue. Irregularities in emission behavior between tips have historically been attributed to anomalies in the fabrication process which results in "sharp" or "less sharp" diamond tips. However, differences are observed in electron emission thresholds even between tips that appear by conventional analysis to be equally well formed. By enabling nanoscale analysis of the emitter surface and sub-surface, the methods developed herein permit analysis of diamond tip structure and provide a basis for optimization of field emitter properties.

Analysis of field emitter nanostructure has the primary benefit of offering feedback to the fabrication process which has not existed before. Prior to this work, poorly emitting tips lacked any explanation unless it was due to dramatic geometric irregularity. Here, we have observed that some of the brightest tips are not the sharpest ones, that low nucleation densities are not a major detractor to emission, and that even tips which are primarily not diamond in content are capable of emitting adequately. Most importantly, methods for analysis of tip structure have been developed to enable a systematic optimization of emitter structure for current and future fabricators. This dissertation contains the first transmission electron microscopy cross-sections of diamond cold cathode field emitters.

These preliminary observations correlate previously unknown diamond cold cathode emitter nanostructure with emission behavior. Correlating structures to emission is expected to be an ongoing process as each phase of technological development introduces new growth chemistries, geometries, and emitter configurations. As emitter requirements transform over time, the important attributes to be optimized will also likely change, making the methods for inspection of these structures more important than ever.

CHAPTER 2

APPLICABLE PHYSICS, LITERATURE REVIEW, HISTORY

2.1. PROPERTIES OF DIAMOND

The term “diamond” refers to the cubic crystalline form of carbon, with a sp^3-tetrahedral hybridized cubic structure, space group O_h^7Fd3 m. CVD-produced diamond materials span a continuum in grain sizes, morphologies, defect structures and concentrations, and properties. Careful control of growth conditions can manipulate the grain size to vary continuously from barely displaying evidence of crystallinity to single domains of nearly perfect gem size single crystals.

2.1.1. Physical

Diamond is the hardest of all natural materials. The hardness of any given material is usually determined by pressing a carefully shaped indenter onto a surface under a load, resulting in a permanent plastic deformation. The indenter must be at least as hard as the substance being indented; for measuring the hardness of diamond, only a diamond indenter is useful. Even then, the indenter itself becomes misshapen after several uses and must be replaced. The applied force on the indenter is divided by area of the impression left on the surface, and so hardness is expressed in units of pressure.

The Mohs hardness scale assigns the hardness of materials based on a scale of 1-10, with each number represented by a known/defined material. On the Mohs scale, 10 represents diamond, but this extreme hardness is not adequately represented due to the non-linearity of the scale. The Mohs scale gives the impression that #9, corundum (also called sapphire), is nearly as hard as diamond, when in reality, there is a 4x increase in hardness between corundum and diamond.

The carbon-nitrogen bond is thought to be stronger than the hybridized carbon-carbon bond of diamond [1]. If so, a material that could possibly be harder than diamond is C_3N_4 [2]. The in-plane doubled bonded C=C bonds of graphite are also stronger that the C-C bonds of diamond. The atomic density of diamond is an unequalled $1.76x10^{23}$ atoms/cm^3.

Diamond has stimulated much interest in the field of tribology, the study and application of friction [3-5]. CVD grown diamond-like carbon (DLC) films have attracted an overwhelming interest from both industry and the research community. These films offer a wide range of exceptional physical, mechanical, biomedical and tribological properties that make them scientifically very interesting and commercially essential for numerous industrial applications.

Mechanically, certain DLC films are extremely hard (as hard as 90 GPa) and resilient, while tribologically they provide some of the lowest known friction and wear coefficients. Because of their excellent chemical inertness, these films are resistant to corrosive and oxidative attacks. The combination of such a wide range of outstanding properties in one material is rather uncommon, so DLC can be very useful in meeting the multifunctional application needs of advanced mechanical systems. In fact, these films are now used in numerous industrial applications, including razor blades, magnetic hard discs, critical engine parts, mechanical face seals, scratch-resistant glasses, invasive or implantable medical devices, optical windows, and microelectromechanical systems (MEMs) [6].

Recent systematic studies of DLC films have confirmed that the presence or absence of certain elemental species, such as hydrogen [7], nitrogen, sulfur, silicon, tungsten, titanium and fluorine [8], in their microstructure can also play significant roles in their properties.

2.1.2. Chemical

An unterminated diamond surface has a propensity to form π bonds between adjacent carbon atoms. Once formed, it is energetically difficult to break these bonds. When the diamond surface is reconstructed with these π bonds, other prospective chemical bonds (almost always of lower energy than the π bonds on the diamond surface) cannot chemically bond to its surface. For decades, miners have exploited diamond’s low surface energy by washing diamond containing gravel over a grease table. Most materials are readily wet by the water and flow over the table, but diamond’s hydrophobicity results in it sticking to the grease at the bottom of the table.

The high atomic density and low surface energy of diamond results in a surface that is biologically inert. For this reason, diamond has excited much interest as a material for biomedical applications. Orlando Auciello and Steven Prawer have been particularly interested in cybernetic implants in the eye, where even small amounts of scar tissue or tissue irritation would cause immense problems.

2.1.3. Electronic

Diamond's potential as an electronic material has become legendary by virtue of its wide band gap (5.5eV), high carrier mobility, breakdown field, saturation velocity, and thermal conductivity. If this potential can be realized, diamond is ideally suited as the material for devices which operate at high temperatures, voltages, power levels, and frequencies, as well as in high-radiation environments. The electrical resistivity of natural diamond is as high as 10^{15} ohm-cm and that of homoepitaxial CVD diamond films is equally high. The potential of diamond as a material for solid state devices has been the subject of a number of reviews [9-13].

As a semiconductor, the properties of diamond (except for electron mobility) are virtually unexcelled. Of semiconductors currently in use, only germanium (Ge) and indium antimonide (InSb) exhibit superior hole mobilities. Even then, these materials exhibit poor saturated hole velocities and low dielectric strength.

A complete description of the energy bands of the diamond crystal [14] can be obtained by solving the Schrodinger equation.

$$-\frac{\hbar^2}{2m}\sum_i \nabla_i^2\psi - \frac{\hbar^2}{2}\sum_\alpha \frac{1}{M_\alpha}\nabla_\alpha^2\psi + \frac{1}{2}\sum_i\sum_j \frac{e^2}{r_{i\,j}}\psi + U_0(R_\alpha)\psi + U'(r_i, R_\alpha)\,\psi = E\psi \qquad \textit{Eq 2-1}$$

Where r_i and R_α denote, respectively, the coordinates of the electrons and of the nuclei (i = 1, 2…; α = 1, 2…), ψ is the wave function of the crystal, and E denotes the total energy of the crystal. The first term in Eq 2-1 corresponds to the kinetic energy of the electrons, and the second term corresponds to the kinetic energy of the nuclei. The factors associated with ψ in the following terms on the left-hand side of Eq 2-1 correspond, respectively, to the following: the potential energy of the interaction between the electrons, the potential energy of the interaction of the nuclei, and the potential energy of the interaction between the electrons and the nuclei. An analytical solution remains incomplete, but approximate solutions exist that introduce a number of simplifying assumptions.

The first significant approximation is the division of atomic cores (nuclei) from their electrons. Nuclei are assumed to be stationary and energy exchange between the electron and nucleus are prohibited. Electron motion is restricted to the field of fixed nuclei. In this approximation R_α is not a variable, but the fixed coordinates of atoms in the lattice. Terms in the summation in Eq 2-1 that depend only slightly on the coordinates of the electrons and which are small in comparison with their kinetic energy are neglected.

The second significant approximation consists of replacing the exact configurational interaction between electrons with an average effective field. In this approximation, interaction of each electron with the remaining electrons is replaced with a sum of potential terms. Eq 2-1 decomposes into:

$$-\frac{\hbar^2}{2m}\nabla^2\psi(r) + [U(r) - E]\psi(r) = 0 \qquad \textit{Eq 2-2}$$

In Eq 2-2, the potential energy U(r) depends on all remaining N electrons and can only be solved by the simultaneous solution of N equations. This would be a hopelessly difficult situation but for a saving property of crystals, namely symmetry. It follows that the potential energy of the electron has the same symmetry as the crystalline atomic lattice. According to Bloch's theorem, the solution of $\psi_k(r)$ in Eq 2-2 has the form:

$$\Psi_k(r) = e^{ikr}u_k\,(r) \qquad \textit{Eq 2-3}$$

where $u_k(r)$ is a periodic function with the period of the lattice and k is the wave vector. Substitution of Eq 2-3 into Eq 2-2 yields:

$$-\frac{\hbar^2}{2m}\nabla^2 u - \frac{\hbar^2}{2m}2ik\nabla u + \left[U(r) + \frac{\hbar^2 k^2}{2m} - E\right]u = 0 \qquad \textit{Eq 2-4}$$

Eq 2-4 allows evaluation of energy E in terms of wave vector k. From here, it is meaningful to construct the model of the electronic structure in terms of the wave vector k, or k-space. The band structure of diamond in k-space is shown in Figure 2-1.

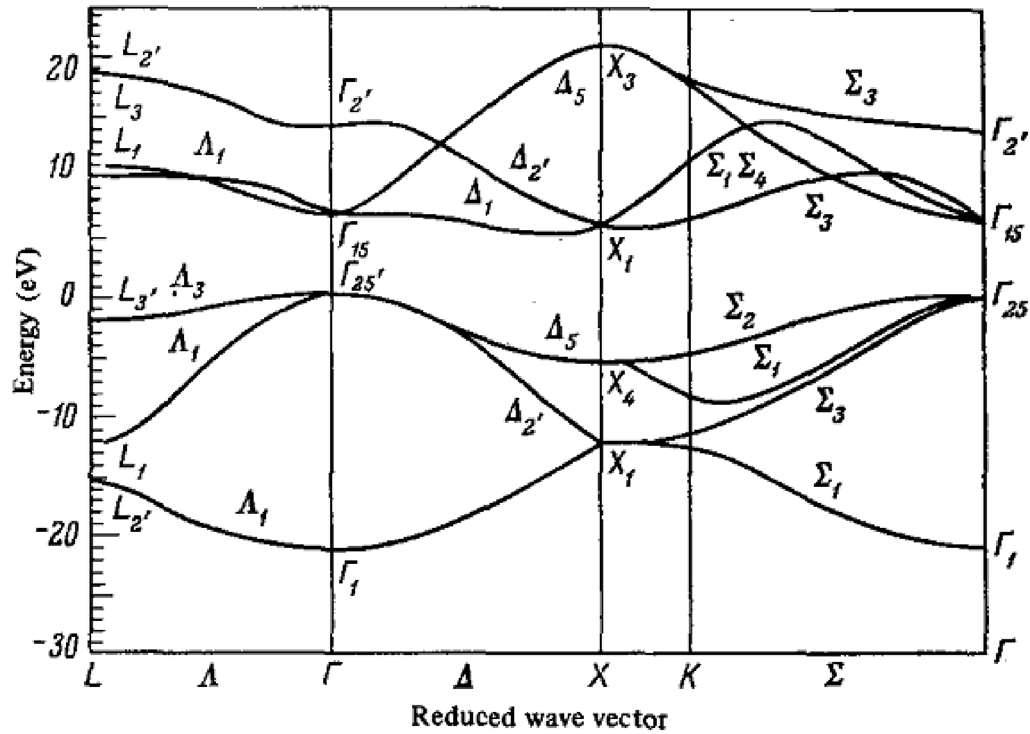

Figure 2-1: Structure of energy bands for diamond [14, 15]

The wide band gap (5.5ev) of diamond simultaneously makes it an excellent insulator and an unusably resistive semiconductor. With doping, the intrinsic properties of diamond can be manipulated into practical energetic states. Boron has been identified as the dopant responsible for p-type behavior in naturally occurring semiconducting diamond [10]. From geometric and energetic considerations, boron is likely the only element that can substitutionally dope diamond without large distortions to the lattice. Nitrogen, a commonly occurring impurity in diamond, is electrically inactive, although it acts as a recombination center [10]. A theoretical study by Kajihara et al [16] suggests the potential of P, Li, and Na as shallow n-type dopants. Phosphorus is theorized to occupy a substitutional site, while lithium and sodium are expected to reside in interstitial positions. Recent work on phosphorous doping has met with some success [17]. Additional treatment of electrical carriers in diamond is addressed in Section 2.4.5.

CVD deposited diamond films necessarily contain hydrogen, as it is an essential component of the plasma growth environment. Hydrogen is known to reduce the resistivity to the order of 10^6 Ω-cm. Annealing in a hydrogen-free environment allows hydrogen to diffuse out of the film, increasing resistivity by a few orders of magnitude [18, 19]. Exposure to hydrogen reversibly reduces the resistivity to as-deposited values. An improved understanding of hydrogen effects in diamond films would certainly contribute to tighter control over electrical properties.

2.1.4. Thermal

Diamond is unmatched as a thermal conductor. It is informative to compare the thermal conductivity of diamond to that of other materials with which it may be used or with which it may compete. Such a comparison is provided in Table 2-1. Polycrystalline diamond films of good quality generally exhibit thermal conductivities in the direction of growth of 55% of single crystals. In the plane of growth, 25% of single crystal values is more typical, but these figures are dependent on grain size [20].

Table 2-1: Thermal conductivity of various materials with which diamond may compete.

Material	**Conductivity (Watts/cm-C)**
Diamond	20
Boron Nitride	13
Water	6
Beryllium Oxide	5.9
Silicon Carbide	4.9
Silver	4.18
Copper	3.8
Ethylene glycol (engine coolant)	2.6
Aluminum	2.38
Iron	.82
Quartz	.14

Heat may be transferred in a solid principally by one of two mechanisms. The most common mechanism, drifting electrons, is most prevalent in metals and alloys. The second principal mechanism is that of thermal phonons (i.e., the directional wave motion of interacting lattice ions). This mechanism is most prevalent in dielectrics such as diamond. At low temperatures, thermal conduction is limited by phonon scattering from impurities and defects in a manner similar to metals. Small sample size may also affect thermal conductivity as phonon phase cancellation from sample boundaries becomes significant. Boundary scattering certainly affects most of the published data for the thermal conductivity of diamond at low temperatures. Actual values are thought to be considerably higher than those published. Diamond’s extraordinary thermal conductivity is entirely due to thermal phonons.

At higher temperatures, phonon-phonon scattering predominates; therefore the thermal conductivities of many dielectrics tend to converge at high temperatures. Phonons may also be scattered by isotopic variations. Carbon naturally contains about 1% of the C^{13} isotope. While the mass differential between Si^{28} and Si^{29} is only 3.6%, the mass differential between C^{12} and C^{13} is 8.3%. If diamond were synthesized from isotopically pure carbon, its thermal conductivity is expected to increase by 40% over natural diamond and a factor of five over that of recent CVD material [21, 22].

In work by Novikov et al. [23], the thermal conductivity of single diamond crystals and CVD diamond films with different C^{13} isotope content has been analyzed in the framework of Debye's model using Klemens–Callaway's expression [24] for the thermal conductivity. The increase in thermal conductivity for isotopically pure diamond can be explained by Callaway’s model by lowering the isotope-scattering effect (Figure 2-2). The effect of C^{13} isotopes on the diamond thermal conductivity was considered, with allowance made for the earlier assumption that the presence of isotopic impurity, apart from direct resistive effects, results in the activation of the normal phonon scattering processes. As a result, the relaxation time of normal processes is observed to depend on the isotopic concentration. In this case, a good agreement between theory and experiment is observed for the temperature region 10 – 1000 K.

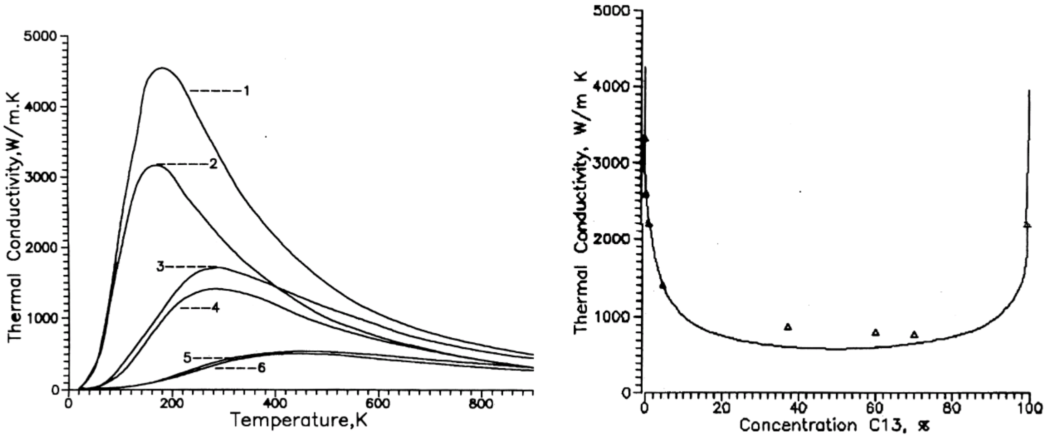

Figure 2-2: Thermal conductivity vs. C ^{13} *isotope content. Loss of thermal conductivity at low purities is attributed to isotope phonon scattering [23]*

Maximum thermal conductivity is essential for thermal management applications. It is also of secondary importance for wear coatings that generate heat during use. With unmatched thermal conductivity, diamond appears to be the ideal heat exchange material. It may be thought of as a solid state heat pipe, but capable of operating over a much wider range of temperatures than any liquid heat pipe. Data from several investigators [25, 26] have shown that minimizing non-diamond material leads to better thermal conductivity.

2.1.5. Optical

Diamond is transparent from the UV (225 nm) to the far infrared. Only minor absorption bands exist resulting from two-phonon absorption between 2.5 and 6.5 µm. This makes diamond an ideal material for multispectral optical applications. Diamond's optical properties are isotropic with an index of refraction of 2.4 in the visible region.

A celebrated early use of a diamond window was for the IR emission sensor of the Venus explorer. Diamond's particular combination of very low absorption coefficient and its very high thermal conductivity permits it to be used as a window for high power lasers [27]. Conventional materials (a) absorb too much of the laser energy, (b) may become nonlinear under the intense energy levels, and (c) cannot dissipate the heat from the center of the window to the outer periphery where a cooling apparatus may be attached. The use of diamond not only reduces absorption by several orders of magnitude, but the absorbed energy is quickly conducted to the window periphery where it may be dissipated safely. Optical mirrors are also similarly vulnerable to high energy laser beams. Diamond mirrors or diffraction gratings have been calculated to reduce the length of a free electron laser 100-fold by reducing the need to diverge the beam to lower power density.

2.2. History of diamond growth

2.2.1. Types of diamond

Diamond was originally classified by its optical properties into types I and II. Later the ‘a’ and ‘b’ suffixes were added. Type I has large amounts of nitrogen included. If the nitrogen is aggregated into platelets (as in most natural diamond) then it is type Ia. If it is dispersed (as in most lab-grown diamond) then it is type Ib with a visible yellow tint. The yellow tint is due to nitrogen defects absorbing in the blue end of the spectrum. Type II is virtually free of nitrogen. Type IIa is colorless and essentially free of impurities making it highly insulating while type IIb contains boron leading to a blue tint. A doping level of only a few parts per million is sufficient to produce the blue color.

2.2.2. Early diamond characterization

The word "diamond" has its origins in Greek "adamao". Adamao has the meaning of "I tame" or "I subdue." The word originally described strong and hard substances. Written records indicate that the Holy Roman Emperor Maximilian gave a diamond engagement ring to his fiancé, Mary of Burgundy, in 1477 [28], which may have been the very first occurrence of a diamond ring. India was the only major producer of diamonds until the discovery of diamonds in South Africa in 1866.

Smithson Tennant demonstrated in 1797 that diamond was a form of carbon by burning diamond with examination of the resulting CO2 gas. Since diamond has a higher density than other forms of carbon, it became immediately plausible that pressure (which reduces volume and therefore increases density) might convert other forms of carbon into diamond.

2.2.3. Diamond growth attempts

Over the years, scientists have developed principles for evaluating scientific accomplishment and attribution. The claim of a successful experiment cannot be fully accepted until it has been duplicated by other experimenters following the published descriptions of the technique. It is obviously the claimant’s fault if inadequate descriptions do not permit a successful duplication, and the claims then have to be discounted.

Given what is now known about the conditions necessary to produce diamond, many of the early (and unfounded) claims to have produced diamond can be discounted. In many cases, the technology in use was incapable of producing the pressures or temperatures required. A phase diagram of carbon illustrating the regimes in which diamond can be formed is shown in Figure 2-3 [29, 30]. When crossing the line delineating the conditions under which diamond can stably exist, it should not be inferred that graphite will spontaneously convert to diamond, as graphite is metastable above this line. The pressures required to form diamond can be difficult to comprehend. The pressure induced by balancing the Eiffel tower on a coin would be approximately enough to induce a phase transformation into diamond, but only if done at temperatures that would turn the tower to a glowing liquid.

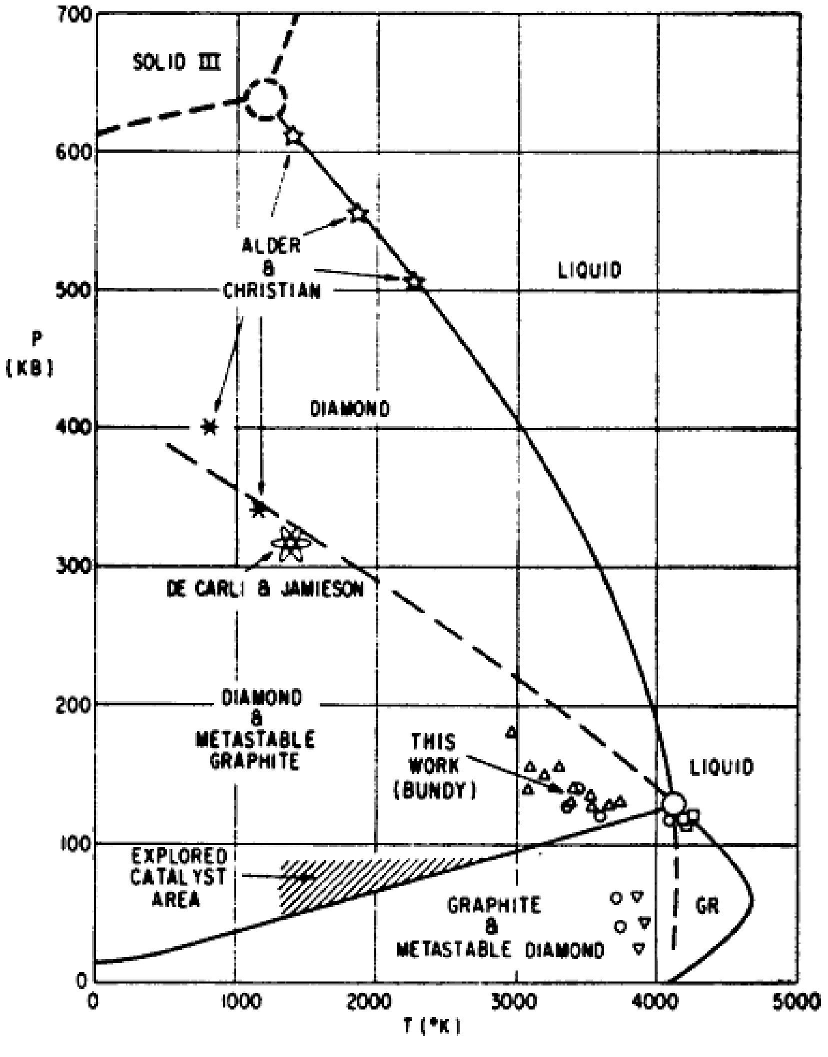

Figure 2-3: Proposed phase diagram of carbon as proposed by Bundy [29].

2.2.4. *Initial diamond growth successes*

2.2.4.1. High pressure high temperature (HPHT)

General Electric (G.E.) announced the growth of diamond in a lab in 1955 and published the procedure in reproducible detail in Nature in 1959 [31]. This method can be performed at pressures as low as 10^6 psi (6.9 GPa) and temperatures below 2000ºC. The line in Figure 2-4 marked Ni shows the melting curve of nickel, which dissolves graphite, for which it has a high solubility, while at the same time crystallizing out diamond, for which the solubility is much lower.

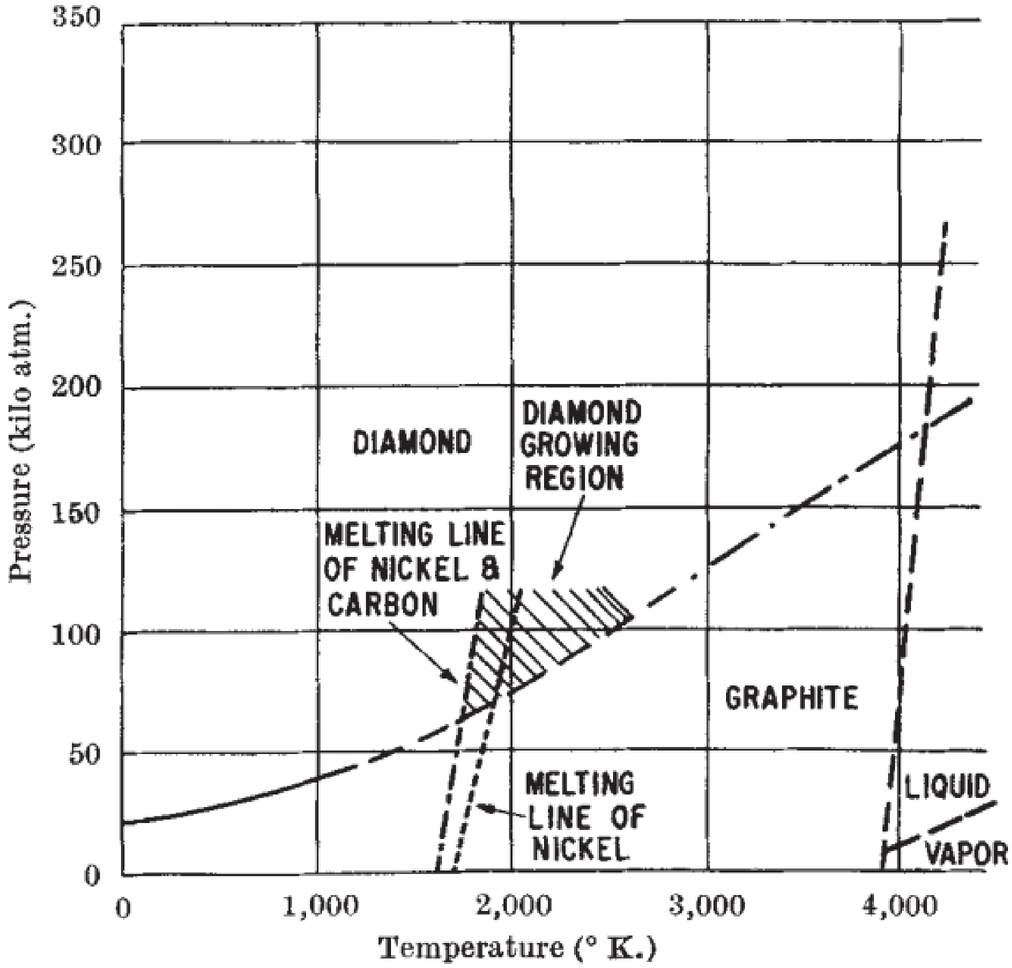

Figure 2-4: The diamond growing region within molten nickel [31].

A sample configuration for the growth of diamond through the use of metal solvents is shown in Figure 2-5 [20, 31]. In this apparatus, the chamber is compressed to at least one million psi. The graphite core is electrified to heat it resistively to a temperature of 1,800ºC. Under these conditions, nickel can dissolve graphite up to 4 wt%. Since the solubility of diamond in nickel is lower than that of graphite (3.6 wt%), diamond crystallizes out. Reportedly, movement of the carbon through the metal is quite rapid. In a few minutes, all the graphite will convert to diamond as the nickel moves from both ends towards the hotter center. The chamber is cooled and then depressurized. Once the metal is dissolved away with acid, the diamond crystals are released. One study [32] observed that the crystal orientation of the resultant diamonds could be influenced by adjusting the chamber temperature.

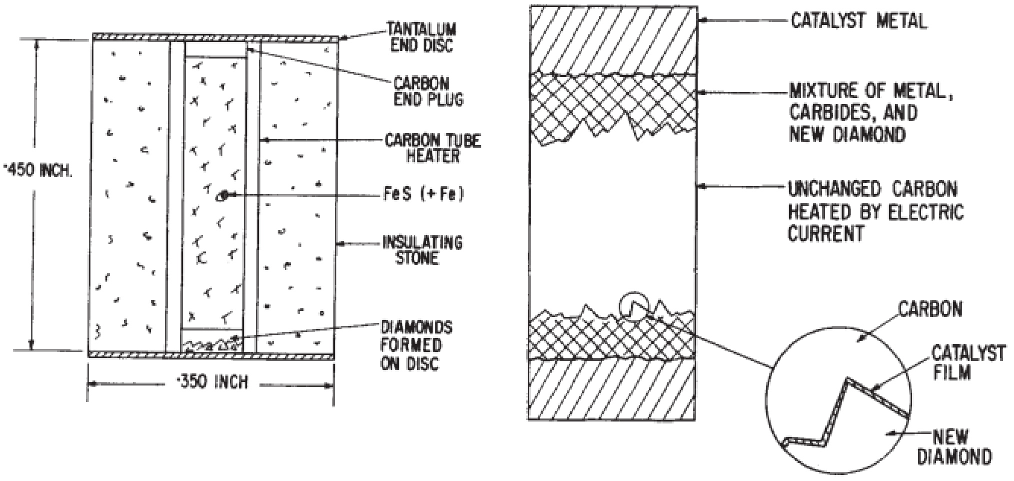

Figure 2-5: Diamond growing apparatus utilizing a metallic solvent as used and described by Bovenkerk et al [31].

At higher temperatures and pressures, diamond has been crystallized without the use of a metal solvent. Diamond has been produced at moderate temperatures and extreme pressures by shock wave techniques [33]. Oddly enough, nearly any form of carbon can be and has been turned into diamond. One report [34] lists over 20 substances that have been successfully turned into diamond including naphthalene (moth flakes), paraffin wax, sugar, and even peanuts.

Fifteen years after the initial G.E. announcement, the achievement of large, gem quality crystals were announced in 1970 with publications by Wentorf, Strong, and Chrenko following in 1971 [35, 36]. Procedures were similar to the processes described earlier, except that seed crystals were used. Diamond grit is preferred as a feed material over graphite because there is shrinkage in the graphite to diamond conversion. By this method, it takes about a week to produce a 5mm (1 carat) crystal. Attempts to accelerate this process result in additional flaws and spontaneous nucleation at the expense of the seed crystals. Figure 2-6 [36] shows a large crystal fabricated by this method from diamond grit (also lab grown). As graded by the GIA scale, these initial diamonds received a remarkable F for color and a respectable VS1 for clarity. Other diamonds were doped with nitrogen, aluminum, and boron for color and to impart semiconducting properties.

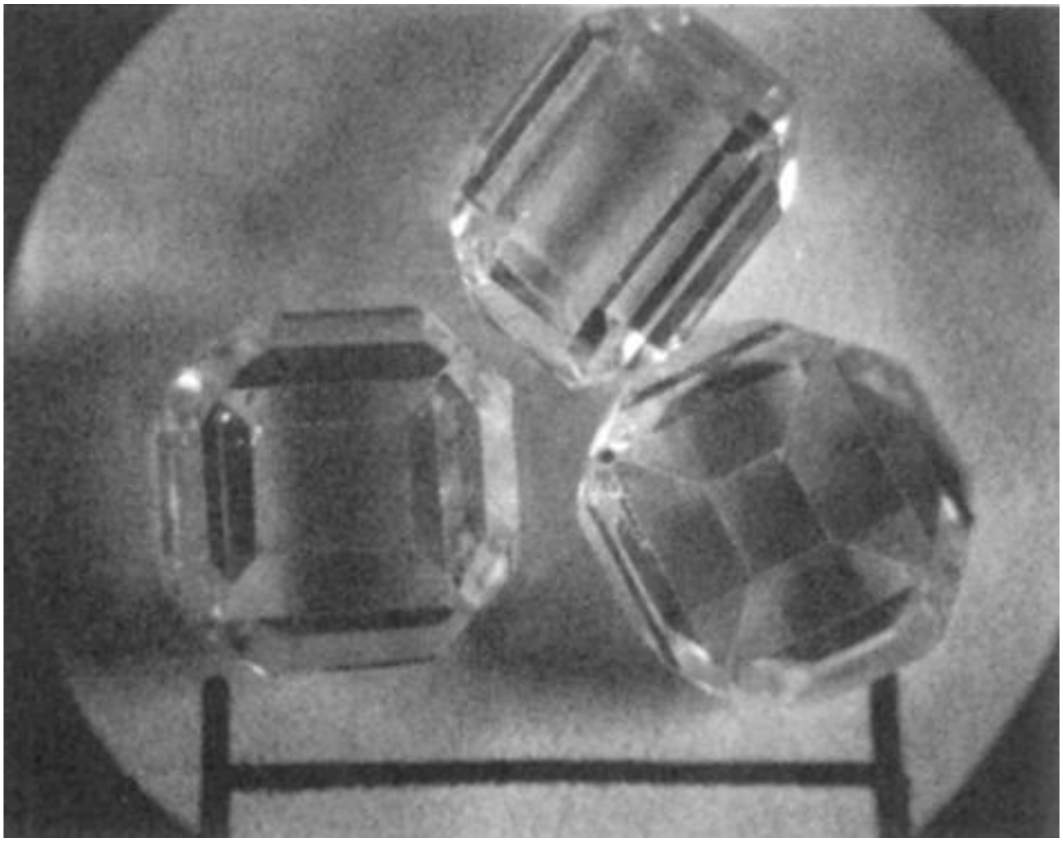

Figure 2-6: Colorless diamonds growth by Strong and Chrenko [36]. The line is 1 cm long.

Lab grown diamond grit is of the same hardness as natural diamond but is superior to natural diamond grit as it is longer lasting in most cutting and abrasive tool applications. The reason that man-made grit is superior lies in the ability to control the size and distribution of crystals by growth conditions without resorting to crushing or grinding the crystals into a powder. Natural diamonds must be powdered to yield grit, a process that involves severe shock and cracking. Many of the resulting particles will thus contain cracks which represent points of weakness and lead to failure or even loss.

2.2.4.2. Detonation diamond

In 1961, DeCarli and Jamieson [33] used an explosive charge to generate a shock wave in graphite with peak pressures of 4.5 million psi for a millionth of a second. The result was a small amount of diamond. If the instantaneous pressure is combined with temperatures of >1,000ºC, the molten carbon immediately forms diamond. Unfortunately, because the pressure applied by this method drops much more rapidly than the temperature, the vast majority of it reverts back to graphite. To combat this, clever arrangements of copper and/or water serve to increase pressure and absorb the heat, thus cooling off the diamond before it can completely revert to graphite.

Current production of detonation nanodiamond is localized in Eastern Europe. Vanderbilt's most recent purchases have originated in the Czech Republic where the detonation nanodiamond then is distributed and processed by a number of global retailers. Current challenges of functionalization and deagglomeration have prevented the price from dropping much below $1,200 USD/kg. Global production as of this writing is at approximately 8,000 kg / year. Retailers include NanoBlox and NanoAmor Inc.

2.2.4.3. Chemical vapor deposition (CVD) of diamond

In 1952, William Eversole at Union Carbide Corporation was the first to reproducibly grow diamond via low-pressure CVD [37]. The growth of diamond from the vapor phase begins with nucleation, the initial formation of a crystal. In order for nucleation to proceed, an incipient nucleus must form and be stable long enough for lattice growth to occur. The development of a critical nucleus, i.e., that size above which it is more probable that a nucleus will survive and grow than that it will decay, depends on the system free energy accompanying growth conditions [20]. Formation of a nucleus is followed by homoepitaxial deposition of additional carbon layers on the surface, thus increasing the crystal size. Optimization of the nucleation step appears to lead to a different set of conditions than optimization of homoepitaxial growth.

Since there is only a slight energy difference between normal and twinned diamond structures, diamond is predisposed towards twinning. Diamond growth is believed to proceed via frequent twinning on (111) planes. W. Zhu [38] observed that while diamond morphology depended on growth conditions, defect density and location also correlated with diamond surface morphology. Only nanoscale roughness was observed on (100) surfaces. These features were different than the micro-scale roughness and features observed on (111) surfaces. Along boundaries of (100) surfaces where (111) planes lie, planar defect features were extensively detected. This observed relationship between the external morphologies and internal defect concentrations is immensely important to designing an experiment to grow structurally perfect diamond films. Oxidation studies on diamond films confirmed the observation that (111) surfaces were more defective [39]. Diamond (111) surfaces were attacked preferentially around defect sites and were observed to be substantially more pock-marked following oxidation than (100) planes, indicating a higher defect density.

Haubner and Lux [40] investigated variables relating to microwave plasmas on the morphology of diamond. They observed gradients in the intensity of the plasmas and linked them with deposition parameters such as gas pressure, flow rate, methane concentration and substrate temperature. High temperatures (~1100ºC) and intensities favored (111) faces while low temperatures (900ºC) and intensities favored (100) faces.

W. Zhu [38] performed a systematic study on CVD-grown diamond morphology variables. With an increase of methane concentration, diamond films tended from (111) faces towards (100) faces. Further increases in methane concentration (beyond 5%) resulted in clustered films with substantial graphitic content. Under a variety of conditions, initial diamond nucleations tend to form roughly cubic shapes instead of extreme octahedral shapes indicating that the growth rates of (111) and (100) faces must be nearly the same, or else the disappearance of a single plane due to a higher growth rate of another plane could not occur.

A myriad of papers have been published with insights into diamond growth kinetics. Analysis of diamond CVD is complicated by a need to manage the competing co-depositions of thermodynamically metastable diamond and the stable graphite phase. Carbon atoms can combine in diverse ways, using sp, sp^2, and sp^3 hybridizations of its valence electrons. This characteristic of carbon lends to the diverse possibilities of chemical reactions and arrangements.

Chemical vapor deposition of polycrystalline diamond has reached a mature and commercial level making the purchase of a plate of CVD diamond a commercial endeavor available to anyone with a hundred dollars in their pocket.

2.3. *THEORETICAL CONSTRUCT, HISTORICAL EVOLUTION OF THEORY*

2.3.1. Three mechanisms of electron emission

The most common types of electron emission are thermionic emission (Section 2.3.1.1), thermionic-field (Schottky) emission, and field emission (Section 2.3.1.2). For thermionic emission, electrons emit into vacuum due to thermal excitation. As the temperature increases, the electrons gain kinetic energy. If the temperature is sufficiently high, some distribution of electrons have energy exceeding the vacuum level. These electrons are spontaneously emitted into vacuum with no applied electric potential. Thermionic emission from metal is normally observed at very high temperatures (>1500°C) dependent on the metal's work function.

At more moderate temperatures, electrons have total energy above the Fermi level (E_F) but below the vacuum level (E_{vac}). In order for these electrons to emit, a moderate electric field must be applied to reduce the width of the potential barrier. Thermally assisted field emission, in which emission is achieved by a combination of increasing thermal energy and reducing the electric barrier potential is called thermionic-field or Schottky emission. Depending on the work function, thermionic-field emission from metal can be observed at temperatures of 700-1500 °C.

At low temperatures (room temperature in this case), a strong electric field must be applied to reduce the width of the potential barrier thereby allowing electrons to quantum-mechanically tunnel into vacuum. This is called field emission because electric field is the main driver inducing electron emission.

2.3.1.1. Thermionic emission

Diamond has now become of interest for thermionic applications due to its unique material properties such as low to negative electron affinity, radiation tolerance, and chemical inertness. Work function values of less than 2eV for nitrogen incorporated diamond films have been reported [41-43] indicating that diamond may be a superior electrode material for a thermionic energy converter. In other work at Vanderbilt [44], the thermionic emission properties of nitrogen-incorporated diamond films are being examined over a broad temperature range for use as an electrode for thermionic energy conversion.

The thermionic emission current density of a heated cathode can be described by the Richardson Equation [45]:

$$J_C = A_C T_C^2 e^{-\Phi_C / kT_C} \qquad \textit{Eq 2-5}$$

J_C: Cathode thermionic emission current density (A/cm^2); A_C: Cathode Richardson Constant (A/cm^{2}T^2); T_C: Cathode temperature (K); Φ_C: Cathode work function (eV); and k: the Boltzmann constant.

It can be seen from Eq 2-5 that a material with a lower work function (Φ) can achieve higher current densities at lower temperatures than a material with a higher work function. Because the Richardson equation pertains to all materials, reverse electron emission current arising from the anode must be accounted for in a similar manner as:

$$J_A = A_A T_A^2 e^{-\Phi_A / kT_A} \qquad \textit{Eq 2-6}$$

where J_A: Anode thermionic emission current density (A/cm^2); A_A: Anode Richardson Constant (A/cm^{2}T^2); T_A: Anode temperature (K); Φ_A: Anode work function (eV); and k: the Boltzmann constant. Assuming that 100% of the electron emitted are collected, we can recognize a net total current as J_T=J_C-J_A.

$$J_T = A_C T_C^2 e^{-\Phi_C / kT_C} - A_A T_A^2 e^{-\Phi_A / kT_A} \qquad \textit{Eq 2-7}$$

2.3.1.2. Field emission

A field emission vacuum diode is a two-electrode electronic device which has a simple structure as shown in Figure 2-7. The first electrode is the cathode which is the source of electron emission. The second electrode is the anode where electrons are collected. The two electrodes are separated by a vacuum gap. To facilitate emission at low electric fields, the cathode is normally made of a material with a low barrier to field emission.

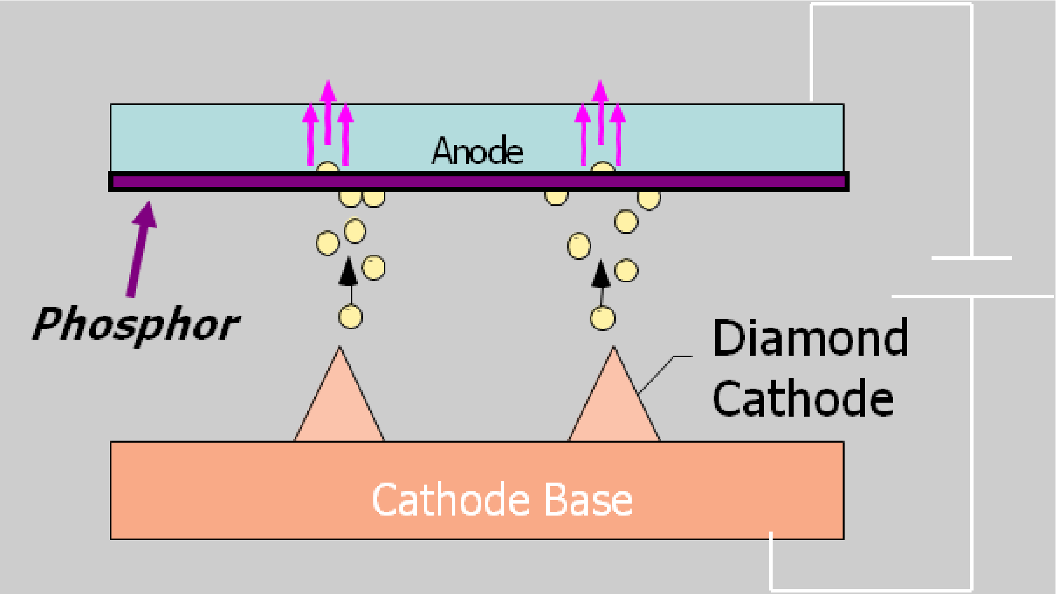

Figure 2-7: Vacuum diode schematic shown with phosphor anode.

Under forward bias, where a positive voltage is applied to the anode with respect to the cathode, electrons may be emitted from the cathode through a surface potential barrier into vacuum via quantum mechanical tunneling. The emitted electrons are accelerated through vacuum gap by the applied electric field and collected at the anode. Under reverse bias where a negative voltage is applied to the anode with respect to the cathode, electrons may emit from anode to the cathode by the same quantum tunneling processes, but this scenario is practically prevented by a dramatically lower geometric enhancement factor at the anode requiring very high fields for emission in this direction. The reverse breakdown field depends on the anode-cathode spacing, anode material properties, and the condition of anode surface.

The potential barrier to emission is called the work function (Φ). In order to eject electrons from a solid surface, energy must be applied to the solid so that electrons can overcome or tunnel through the potential barrier. Similarly, given the presence of electrons in the conduction band, the electron affinity (χ) embodies the energy barrier between the conduction band and vacuum. Further treatment of the energy band structure of diamond is found in Section 2.1.3. Discussion of surface treatments that can result in a negative electron affinity is found in Section 2.4.3.

2.3.2. *Fowler-Nordheim field emission theory*

Electron field emission from metal has been verified theoretically and experimentally to follow the Fowler-Nordheim [46] equation:

$$J= K1(E2/\Phi)exp(-K2\ \Phi3/2/E) \qquad \text{Eq 2-8}$$

where J is the emission current density (A/cm^2); K_1 and K_2 are constants: K_1=1.54x10^{-6} A·eV/V^2, K_2=6.83x10^7 V/(cm·(eV)$^{3/2}$); Φ is the work function (eV) of the emitting surface and ‘E’ is the macroscopic electric field (V/cm) across the parallel plates, which is given by E = V/D. ‘V’ is the applied voltage and ‘D’ is the anode-cathode spacing.

Eq 2-8 can be expressed in Fowler-Nordheim form to demonstrate the exponential relationship of the equation:

$$\mathrm{Ln}\left(\mathrm{I}/\mathrm{E}^2\right) = \mathrm{Ln}\left(\mathrm{AK}_1\beta^2/\phi\right) - \left[\left(\mathrm{K}_2\phi^{1.5}/\beta\right)\left(1/\mathrm{E}\right)\right] \qquad \text{Eq 2-9}$$

In Eq 2-9, the image effect has been ignored, since it is considered to have minor effects on emission current at all but the most extreme current densities. Space charge is negligible below current densities of the order of 10^7 amperes/cm^2 [47].

Apparent in the equation, the emission current strongly depends on the work function of the cathode. A low work function contributes to a higher emission current for a given applied electric field. In this second form, a plot of Ln (I/E^2) versus 1/E should be linear with slope equal to $-K_2\Phi^{1.5}/\beta$ and the y-intercept equals to Ln ($AK_1\beta^2/\Phi$). This plot is generally referred to a Fowler-Nordheim (F-N) plot. F-N plots of the experimental data collected in the course of this dissertation are generally in good agreement with the F-N equation.

2.3.3. *Improvements upon the F-N form*

The Fowler Nordheim (F-N) equation is derived for a planar cathode with an assumption that there is uniform electric field in the vacuum gap. These assumptions are not valid for sharp non-metallic structures. The precise calculation of potential distribution, electric field, and emission current for a sharp microstructure involves numerical calculation of the 3-dimensional Poisson equation and Schrodinger equation for electron emission.

There are three experimentally unknown device parameters involved in the slope and intercept of an F-N plot: the emitting area (A), the work function (Φ), and the field enhancement factor (β). These three parameters cannot empirically be determined, because only two equations can be obtained from the slope and intercept of the F-N plot. Additional methods must be used to determine one of these unknown parameters.

The emitting area (A) is easy to estimate but there is no experimental technique to directly measure the emitting area of diamond field emission cathodes. Furthermore, it is expected that the area is field-dependent and geometry specific. Spindt et al [48] provide a formalism for the calculation of emitting area based on measurable dimensions and known quantities such as applied field. Gotoh et al have attempted to measure emission area but with ambiguous results [49].

The work function (Φ) of diamond is difficult to determine because diamond is a wide-band-gap material. Work by Gomer et al [50] describes a linear dependence of work function on field. In addition, the work function of polycrystalline diamond depends on composition and surface structure. Measurements of work function of polycrystalline diamond films have been performed by many research groups worldwide [42, 44, 51-55].

The field enhancement factor (β) depends on the geometry of the cathode, and it may be estimated by physical measurement of the diamond tip geometry by SEM. Consider the sharp cone structure as illustrated in Figure 2-8. The sharp cone structure is generally referred as a “Spindt cathode” in reference to Dr. Charles Spindt’s work on the fabrication of conical metal field emitters [48]. The sharp cone structure results in non-uniform electric field at the emitter surface as illustrated in Figure 2-9.

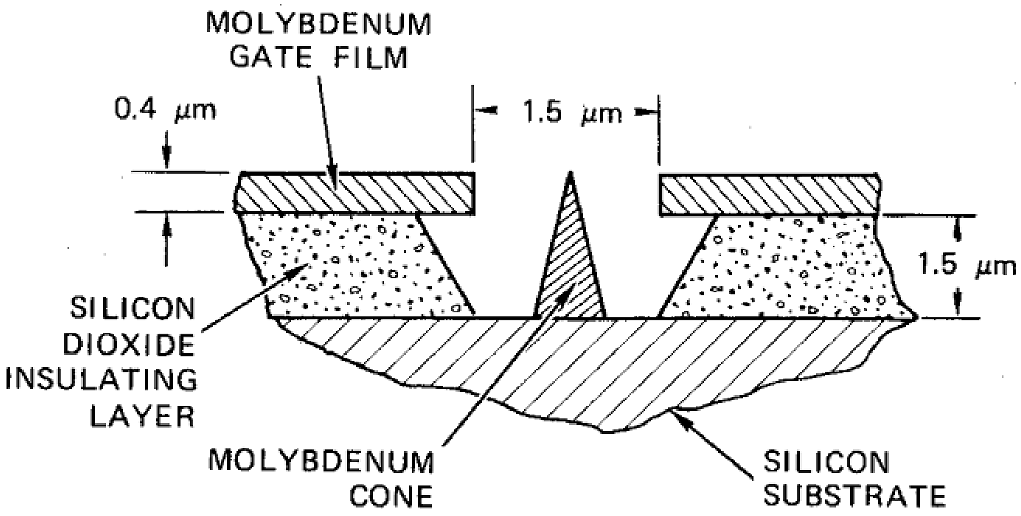

Figure 2-8: Spindt field emission cathode made of a sharp molybdenum cone. [48]

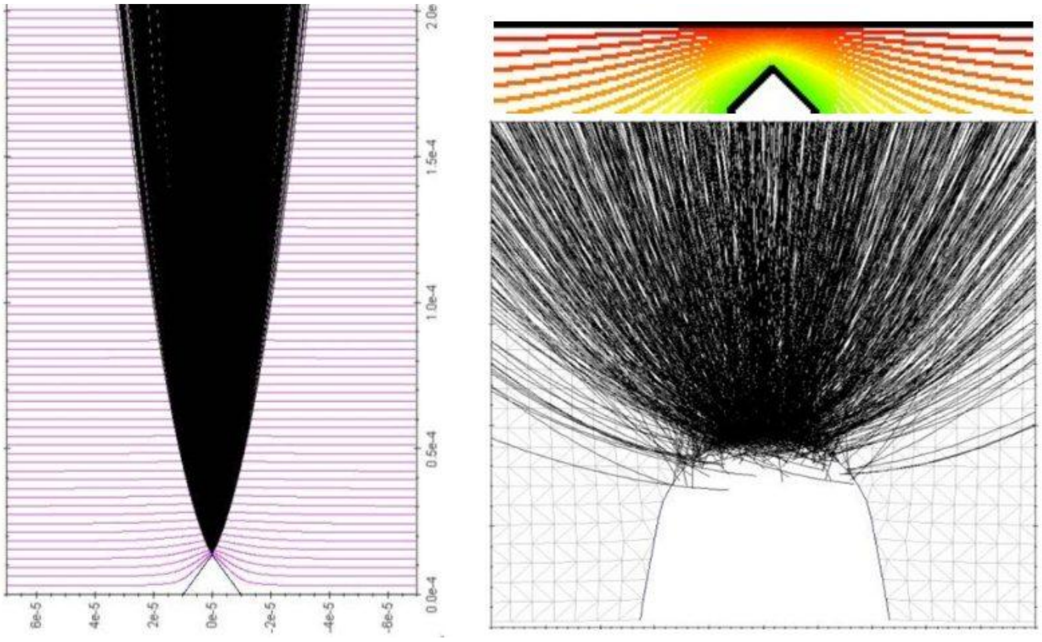

Figure 2-9: Result of modeling efforts showing field lines over a diamond tip showing the local enhancement of field at sharp features. Modeling performed by students in Dr. Brau's laboratory.

An approximation of emission current for a sharp microstructure can be obtained with a simple modification of Fowler-Nordheim equation for a planar metal cathode by replacing the parallel electric field with electric field at the apex of the sharp microstructure that is E=βV/d. 'β' is the factor by which electric field is increased due the sharp microstructure relative to the planar structure. Calculations of emission dependence on β performed by Dyke et al [47] indicate that an increase in β of only 20% would decrease the emission current by more than a factor of 10. In the case of these pyramidal tips, a tip radius of 5 nm differs by 20% from a tip radius of 6 nm. A high degree of control is therefore required for predictable field emission.

It is well known that the geometric field enhancement factor increases with sharpness of the tip and the field at the apex of the tip is inversely and non-linearly proportional to the tip radius. A common and simple approximation implies that the emission current for a sharp microstructure is equivalent to the emission current of a planar cathode of the same vacuum gap but the effective electric field is increased by the factor of β. This approximation agrees well with experimental results because the electric field of a sharp tip is strongest at the apex and decays rapidly for the region away from the apex. It can be assumed that the emission current arises entirely from electron tunneling within the vicinity of this highest electric field region.

2.4. FACTORS RELEVANT TO ELECTRON EMISSION FROM DIAMOND

2.4.1. Topology / geometric enhancement

Experimental results demonstrate that turn-on electric field can be significantly reduced by tip sharpening. The virtues of geometric field enhancement have been understood since Dr. Charles Spindt [48] developed sharp metal features for field emission applications.

The field enhancement factor of the sharpened diamond tip can be estimated using a two-step field emission enhancement model. In this model [56], the sharpened diamond tip is modeled as a large conical tip with tip height of h_1 and tip radius curvature of r_1 superimposed with a sharp tiny conical tip with tip height of h_2 and tip radius curvature of r_2 as illustrated in Figure 2-10. The electric field at the sharpened tip apex arises from the two-tip cascaded structure. In the first step, the electric field at the apex of large conical tip is enhanced by the factor of h_1/r_1 from the planar base. In the second step, the electric field at the apex of the sharp tiny conical tip is enhanced by the factor of h_2/r_2 from the apex of large conical tip. Thus, the total geometrical field enhancement factor of the sharpened tip is the product of field enhancement factor of two cascaded tip structure.

$$\beta_{sharpened} = (h_1/r_1)(h_2/r_2) \qquad \text{Eq 2-10}$$

Geometric field enhancement factors calculated by this method agree reasonably well with results derived from experimental F-N emission analysis [57].

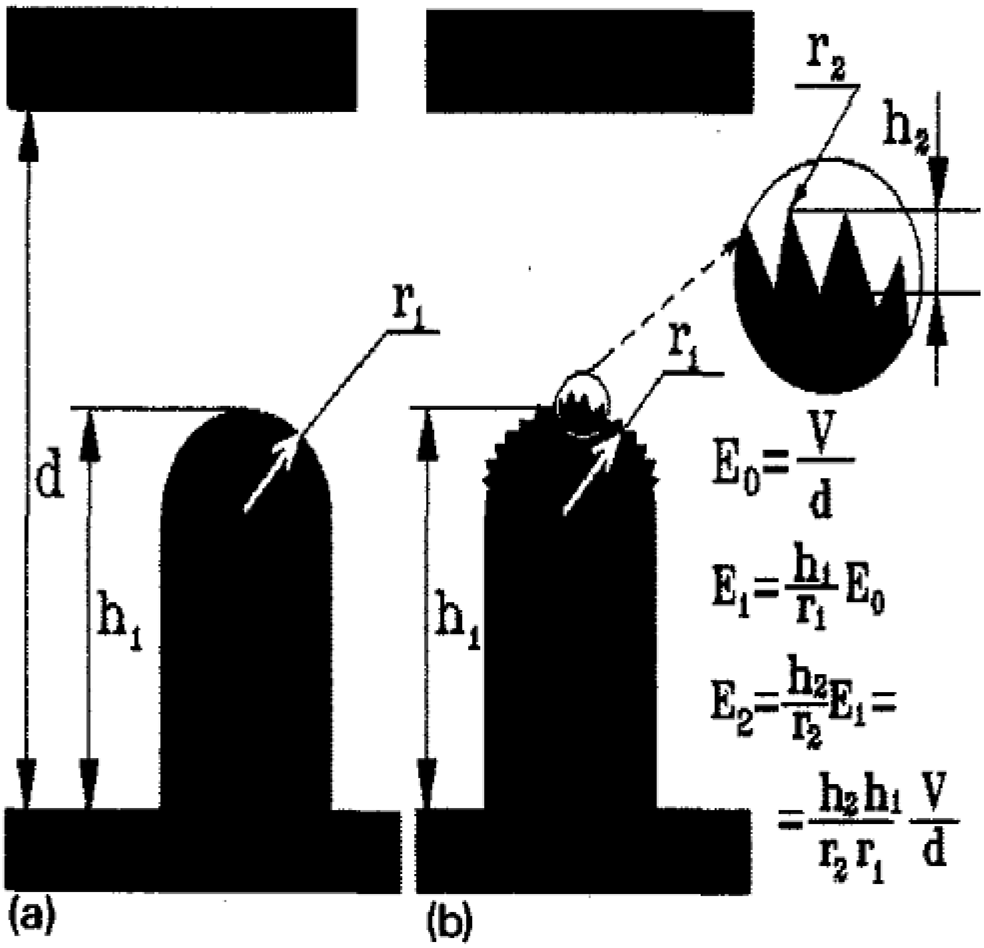

Figure 2-10: Field enhancement model as illustrated by Givargizov et al [56]

After the Fowler-Nordheim theoretical work in 1928, a notable advance in geometric enhancement came with the development in 1937 by Erwin W. Müeller of the field electron microscope (FEM). Müeller used a sharply pointed tungsten wire as a field emitter tip in a vacuum enclosure opposite a phosphor screen. As voltage is applied between the tip and screen, an image forms which reflects the current-density distribution across the emitter apex. Smaller emitting surfaces and longer drift distances between the cathode and anode increase the effective magnification, which is commonly ~10^6x.

The geometrically enhanced emitter concept can be extended to a silicon cathode. The silicon cathode is usually heavily doped (n+) to achieve a low work function for silicon ($\Phi \approx \chi =$ 4.12 eV) and good ohmic contact with the metal back plate. Silicon emitters have shown some improvement over metal cathodes [113]. Since the work function of silicon is the same order of magnitude as most metals, the improvement obtained from a silicon emitter is in increasing the geometric field enhancement factor due to the availability of advanced silicon technology. Mature integrated circuit manufacturing technology facilitates mass production of the emitters. However, silicon emitters have limited applications because the operating voltage of a silicon cathode is still high compared to that of a solid-state device. In addition, silicon emitters have a serious surface adsorption problem, which leads to instability and lifetime issues.

2.4.2. Temperature

Due to the large band gap, diamond field emitters are largely temperature independent. At high temperatures (>700°C), diamond field emitters have been found to emit by thermionic mechanisms consistent with the Richardson Equation [45, 58]. Detailed discussion of the Richardson equation and thermionic emission is addressed in Section 2.3.1.1.

2.4.3. Electron affinity/crystal face

Diamond has low electron affinity, which is a measure of the energy barrier that electrons must overcome to escape into vacuum from the conduction band. This combination of low surface barrier to electron emission in an otherwise robust material has attracted attention to diamond's promise as a high performance cold cathode material. Diamond is an indirect wide-band-gap material with E_g =5.45 eV.

Electrons in the conduction band are generally prevented from escaping into the vacuum by the electron affinity barrier (χ). However, the diamond (100), (110), and (111) surfaces are known to exhibit negative electron affinity when terminated with hydrogen [54, 59-62]. Hydrogen exists as an ionic species forming an affinity lowering surface dipole sufficient to result in a NEA surface. It is rare to find a material system for which the electron affinity is negative indicating that any electron that manages to be in the conduction band will be spontaneously emitted from the surface. Himpsel et al have observed negative electron affinity from unterminated, unreconstructed diamond (111) surfaces [59].

Diederich et al.[54] investigated band bending, electron affinity and work function of differently terminated, doped and oriented diamond surfaces by X-ray and ultraviolet photoelectron spectroscopy (XPS and UPS). The hydrogen-terminated diamond surfaces have negative electron affinity (NEA), whereas the hydrogen-free surfaces present positive electron affinity (PEA). The NEA peak is only observed for the boron-doped diamond (100)-(2×1):H surface, whereas it is not visible for the nitrogen-doped diamond (100)-(2×1):H surface due to strong upward band bending. Electron emission from energy levels below the conduction band minimum (CBM) up to the vacuum level E_{vac} allowed the electron affinity to be measured quantitatively for PEA as well as for NEA. The lightly boron-doped diamond (100)-(2×1):H surface presents a high-intensity NEA peak. Its cut-off is situated at a kinetic energy of 4.9 eV, whereas the upper limit of the vacuum level is situated at 3.9 eV, resulting in a NEA of at least −1.0 eV and a maximum work function of 3.9 eV. The highly-boron-doped diamond (100) surface behaves similarly, showing that the NEA peak is present due to the downward band bending independent of the boron concentration. The nitrogen-doped (100)-(2×1):H surface shows a low NEA of −0.2 eV but no NEA peak due to the strong upward band bending. E_{vac} is situated at 4.2 eV or below, resulting in a NEA of at least −0.9 eV and a maximum work function of 4.2 eV. The high-intensity NEA peak of boron-doped diamond seems to be due to the downward band bending together with the reduced work function because of hydrogen termination. Though unaffected by anneals up to 600°C, upon hydrogen desorption at higher annealing temperatures (1,100°C), the work function increases and NEA disappears. For the nitrogen-doped diamond (100) surface, the work function behaves similarly, but the observation of a NEA peak is absent because of the surface barrier formed by the high upward band bending.

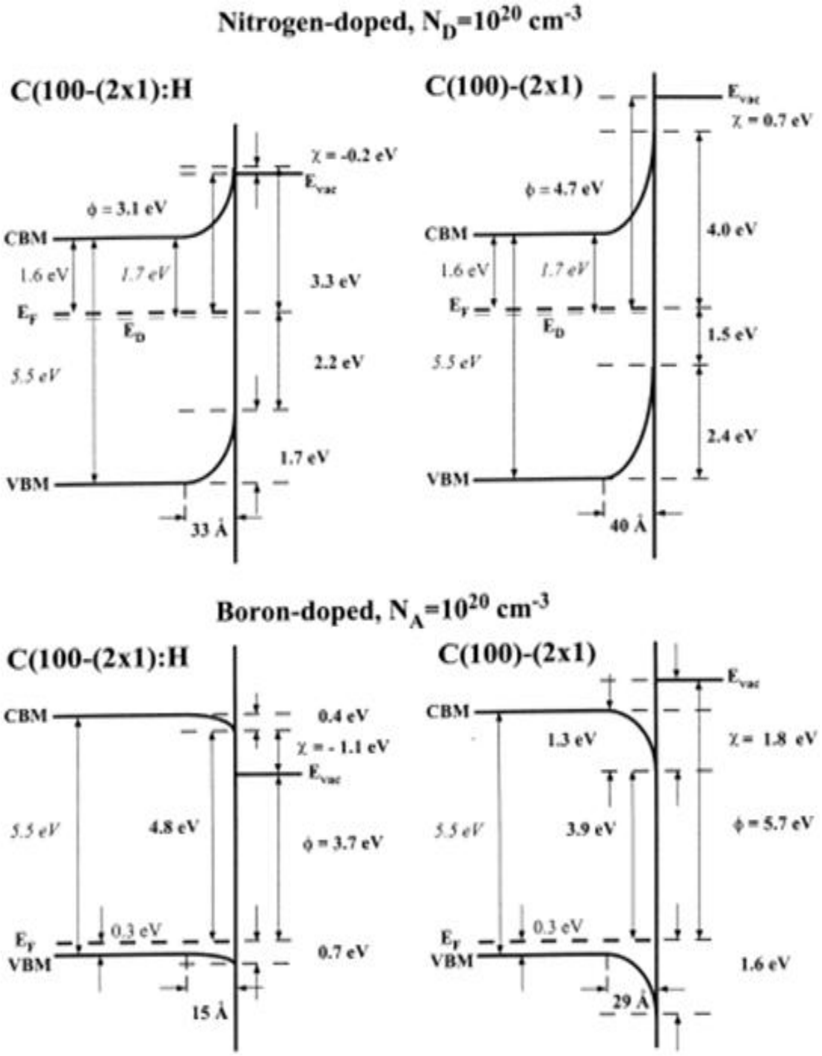

Figure 2-11: Measurements of electron affinity and band bending on diamond surfaces with boron and nitrogen doping. Hydrogen-terminated surfaces (two plots on left) show negative electron affinity. Boron doping leads to downward band bending while nitrogen causes upward band bending. Image from Diederich et al. [54]

For hydrogen-free diamond (100) surfaces, the electron affinity is small and positive as shown in Figure 2-11. Partially hydrogenated diamond surfaces display negative electron affinity (NEA), as illustrated in Figure 2-12. The diamond (100)-(2x1):H hydrogenated surface is believed to be a true NEA surface as illustrated in Figure 2-11. The small electron affinity of diamond is believed to be critical to the observed emission from diamond at very low fields.

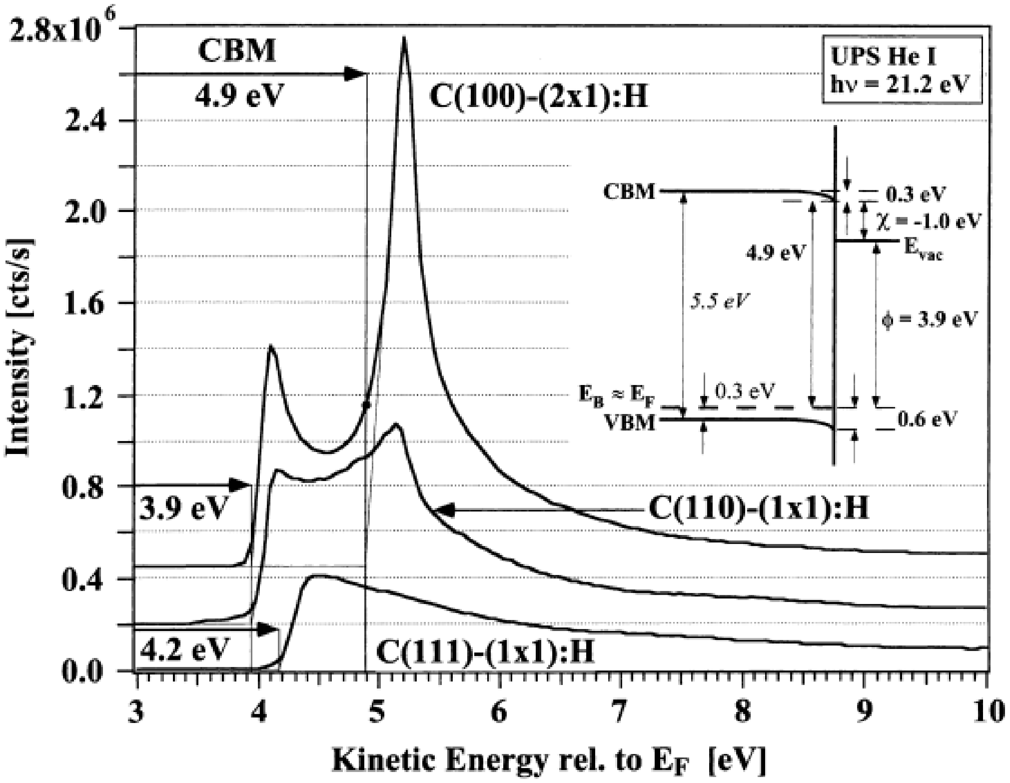

Figure 2-12: Ultraviolet photoelectron spectroscopy (UPS) results of three hydrogen terminated diamond surfaces, all displaying negative electron affinity [61].

A diamond surface coated with a thin layer of certain metals including Zirconium (Zr) [51], Cobalt (Co) [63], Ni [60], TiO [64], and Cs [65] have also been observed to exhibit NEA.

While the low electron affinity property of diamond surfaces may be important and can make diamond an efficient emitter, it is not adequate, by simply invoking this property, to explain why diamond is a good field emitter material. To sustain field emission, there must be a continuous supply of electrons and a sustainable transport mechanism for the electrons to reach the surface. Emission related to a small electron affinity requires population of states in the conduction band which is limited due to the wide band gap of diamond. A small electron affinity surface is practically useful in reducing the barrier for electron emission only when the energy levels of some occupied states or bands, possibly including surface states, are positioned sufficiently close to the conduction band minimum in diamond. Unless n-type doping is performed, electrons must be injected into the conduction band of diamond in order for emission to occur. High electric fields should be required for electrons to tunnel through a metal-diamond interface because the potential barrier at a metal-diamond interface would be as high as the work function of silicon or metals.

Ultraviolet photoemission spectroscopy studies of diamond surface termination with deuterium performed by Baumann and Nemanich [62] confirm the predicted higher binding energy of deuterium. Deuterium imparts the same negative electron affinity characteristics to the diamond surface as hydrogen but with a higher binding energy. Hydrogen is observed to impart a negative electron affinity to the (100) surface of diamond up to a temperature of 1,100°C. Deuterium imparts the same affinity lowering effect but is observed to be stable up to 1,250°C. Similarly, annealing hydrogen terminated diamond (110) surfaces to 800°C was sufficient to remove the negative electron affinity, but temperatures of 900°C were required to remove the negative electron affinity from the deuterium terminated surface. Difficulty in procuring a single crystal (111) faced diamond prevent study of this surface, but similar effects are expected.

Deuterium has been found to preferentially abstract and replace hydrogen on polycrystalline diamond surfaces by Koleske et al [66]. Desorbed atoms/molecules were analyzed by mass analysis of time of flight experiments. Hydrogen was found to be abstracted 3x faster than deuterium on diamond surfaces.

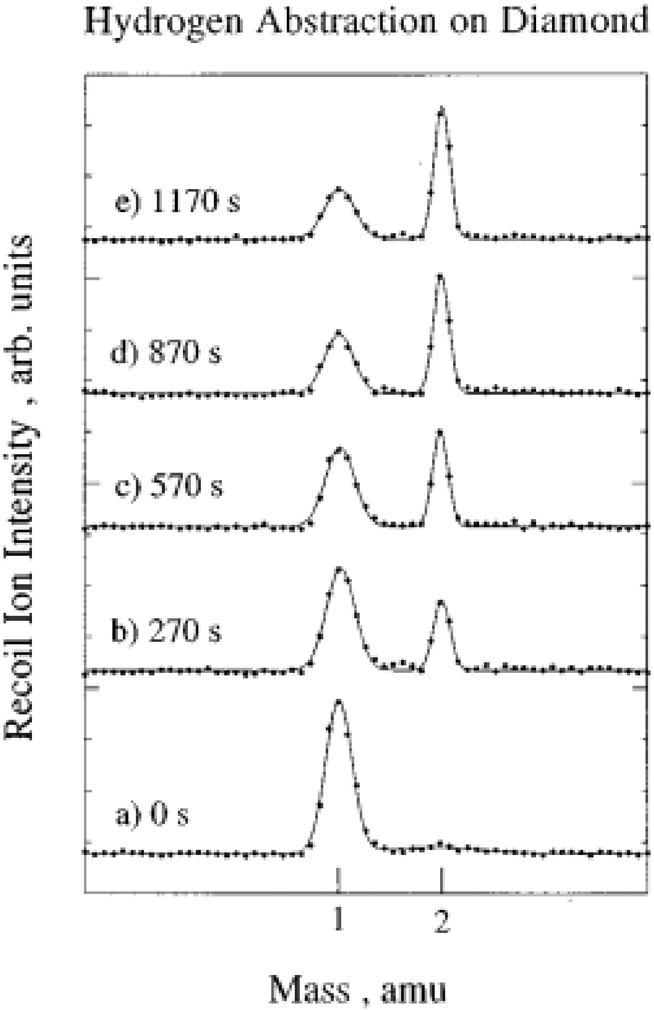

Figure 2-13: Over time, hydrogen is abstracted from diamond by a deuterium flow. [66]

2.4.4. Defect states

Defect states or bands are very probable origins of electrons for field emission enhancement. Defects in diamond such as vacancies and grain boundaries are created during growth by chemical vapor deposition. Vacancy defects in diamond thin films can be substantial [67, 68]. In addition, defects in the form of graphite and multiply twinned quintuplet wedges [69] have also been observed.

Calculations [70] indicate that defect states may exist in the bulk band gap. The effects of the negative electron affinity, the band bending, the image interaction, and surface states have been examined by Huang et al. They found that the conventional theory of electron field emission applied to crystalline diamond cannot explain the measured high-current emission at low fields. They postulate two sub-bands in the intrinsic band gap, which may be generated by defects or impurities. With reasonable band parameters, the calculated I-V characteristics agree with experimental data. If the defect concentration is significant, the electron states in these defects could form energy bands as illustrated in Figure 2-14. Huang unfortunately makes the indefensible assumption that emission from defect states will have an infinite supply of electrons like a valence band, when in fact carrier replenishment is a major barrier to field emission from defect states. More theoretical study is needed to determine how these defect states couple to each other to form a defect-induced conducting band.

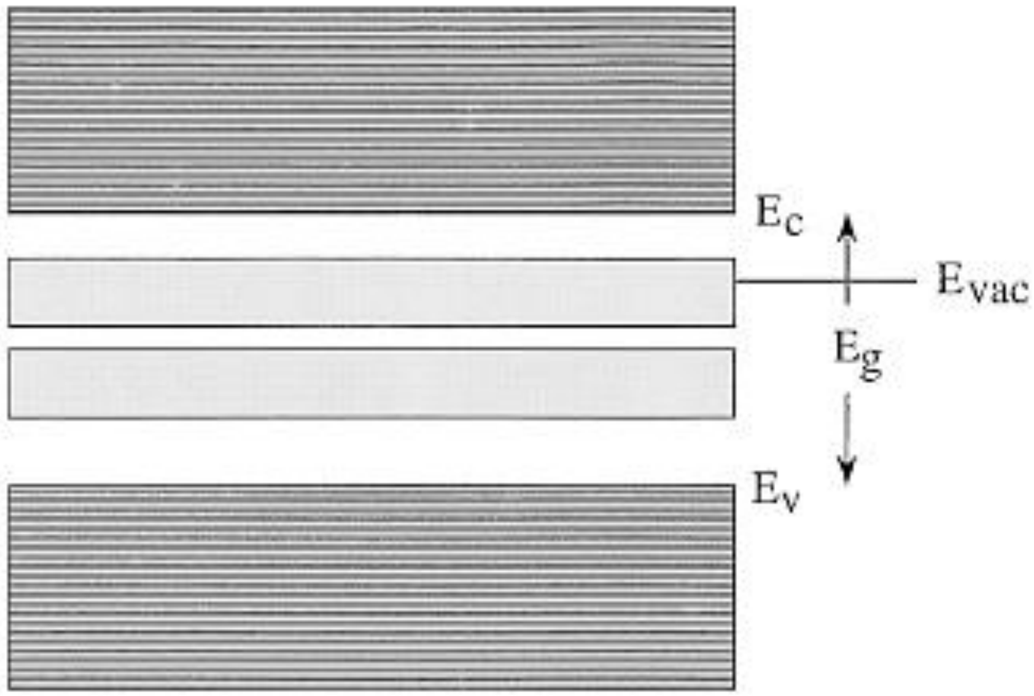

Figure 2-14: Illustration of intraband states as proposed by Huang et al [70].

XPS studies were performed in 2008 on diamond films by Yamaguchi et al. [71] in order to shed light on the origin of emitted electrons. In this work, the authors theorized that, since the emitted electrons were observed to be mono-energetic, they must originate in the same energy state. Since emission currents are large, the energy state from which the electrons are emitting must have a high density of states. They concluded that emission must be occurring directly from the valence band, as the only known energy level with a sufficiently high density of states.

Diamond samples with varying defect densities have been synthesized by CVD and their field emission characteristics have been analyzed [72, 73]. It was found that the potential barrier of undoped diamond films declines rapidly with increasing structural defect density. Similar correlations between the field emission and the structural defect density were also observed for p-type (boron) diamond films. It was also found that emission from p-type diamond films was more stable than undoped diamond films. These studies demonstrated that the creation of defects and likely defect-induced energy band(s) enhanced field emission. If these bands are wide enough or closely spaced, electron hopping within the band(s) or excitation from the valence band could provide the necessary conduction path for electrons to reach the emitter surface to sustain stable emission of electrons into vacuum. Electrons may tunnel directly from these bands or hop to surface states for emission. The position(s) of these defect-induced energy bands could not be determined because of uncertainty in the local field enhancement factor and emission area.

A detailed theoretical examination of electron transport mechanisms in diamond did not reveal any viable process to populate these tunneling states [74]. The density of states for a lattice with a single vacancy has been calculated by Cutler et al. and found that defect states exist only within a narrow energy range (~1-2 eV) above the valence band maximum. However, since this study was performed, additional defect states have been recently located 2.0 eV below the conduction band minimum of diamond by photoelectron yield spectroscopy [75]. Defect states such as these may become viable candidates for electron emission from diamond.

Defects created by ion implantation have also been studied for electron field emission [72, 76]. Emission threshold field was observed to decline rapidly as the implantation dose increases. In addition, implantation of silicon ions resulted in more dramatic electron emission enhancement than carbon implantation. This was attributed to the larger mass of silicon ions producing more defects and damage. The emission characteristics of implanted diamond films were found to be insensitive to atmospheric exposure, suggesting that the modified surface produced by the implantation process is stable and chemically inert. Defects introduced in the surface regions by ion implantation were observed to increase the conductivity and reduce the work function of the diamond. The effect of carbon, hydrogen, argon, and xenon ion irradiation on a pure graphite carbon fiber has also been studied [77]. The field emission threshold could be minimized with careful choice of dose, beyond which the emission threshold was degraded by further implantation.

In previous work at Vanderbilt, it has been concluded that the turn-on threshold of the undoped diamond tips tends to improve as sp^2 content increases. These results are in agreement with other work on diamond coated emitters and planar diamond films [78-80].

2.4.5. Carrier transport

Bobrov et al. have explored single crystal diamond electronic structure via scanning tunneling microscopy (STM) [81]. In high purity single crystal diamond, they observed one-dimensional fully delocalized states and very long diffusion lengths for conduction band electrons. The insulating nature of diamond makes it difficult to probe electronic states, and indeed the STM tip was crashed when trying to establish a tunneling current. By annealing in situ, they were able to remove adsorbed hydrogen and realize a 5MΩ resistance through 200 μm of diamond. Only at high voltages (5.9V+) was imaging possible, indicating that the STM is operating in the near-field emission regime.

2.4.5.1. N-type doping

Diamond has many superior materials properties, yet its application in electronic devices is severely limited due to the difficulty of producing n-type thin films of sufficiently high conductivity. Defects may be deliberately introduced into the diamond film by the incorporation of dopants. Previous efforts to synthesize diamond or diamond-like carbon thin films with high n-type conductivity have been largely unsuccessful. [82-85]

Although part of the prior work [85] demonstrated that n-type doping could produce shallow donor levels close to the conduction band of diamond, the room-temperature conductivities are still too low for the application of these materials in conventional electronic devices.

The donor state of nitrogen lies in the band gap of diamond 2.2eV below the conduction band. Since nitrogen is a deep donor impurity that is not ionized at room temperature, field emission enhancement is not expected to arise from the direct emission from the donor dopant but could instead arise from dopant related defect centers. Known nitrogen-related defects include vacancies trapped adjacent to the substitutional nitrogen atom (1.94 and 2.15 eV above the valence band maximum), at A centers (2.3 and 2.46 eV), and at B centers (2.49 eV). These defects were identified by photoluminescence (PL) and cathodoluminescence (CL) spectroscopy measurements. However, electrons in these defect states would seem to require too much energy to couple to the vacuum or conduction band.

Highly conducting n-doped nanocrystalline films were grown in work by Bhattacharyya et al [86]. Nitrogen-doped UNCD thin films were synthesized using CVD with a CH_4 /Ar/N_2 gas mixture. The morphology and transport properties of the films were observed to be greatly affected by the presence and amount of CN in the plasma, which varies as nitrogen gas is added. The TEM data indicate that the grain size and grain boundary width increase with the addition of N_2 in the plasma. Transport measurements indicate that these films have impressive n-type electrical conductivity as shown in the Arrhenius plot (Figure 2-15) for a series of films synthesized using different nitrogen concentrations in the plasma.

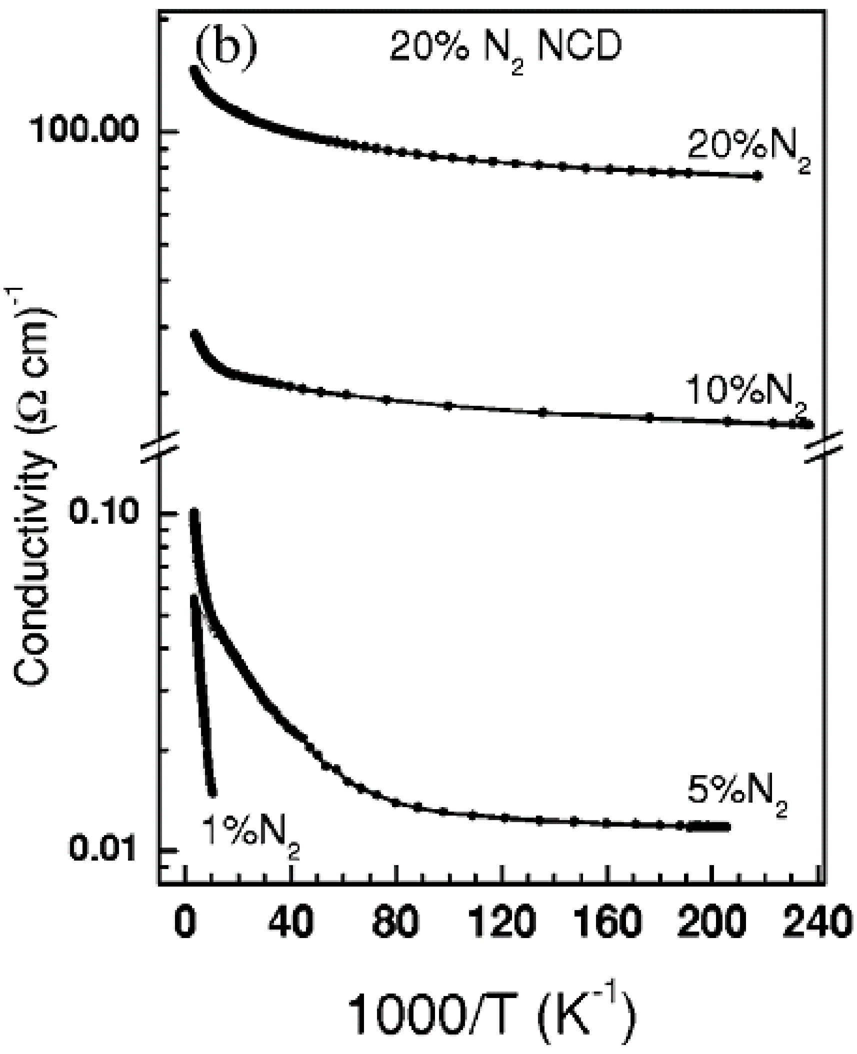

Figure 2-15: Arrhenius plot for a series of films produced by Bhattacharyya et al [86]

In recent years, work function values of less than 2eV for nitrogen incorporated diamond films have been reported. In work by Koeck et al [87], doped diamond films with a negative electron affinity (NEA) surface showed a reduced effective work function for electron emission of ~ 1.5 eV for nitrogen doped diamond films prepared by microwave plasma CVD. The film exhibited a resistance that decreased with temperature suggesting the role of the dopant. An analysis based on the Richardson–Dushman equation indicated an emission barrier of < 1.3 eV. In similar systems, work by Suzuki et al [88] derived a work function of 1.99eV in nitrogen incorporated diamond.

2.4.5.2. P-type doping

P-type doping lowers the Fermi-level of the bulk and traditionally increases the work function. However, in boron doped (p-type) diamond films, the turn-on electric field decreases with p-type doping. This is due to surface band bending and is explained by Diederich et al in Figure 2-11 which demonstrates the effect of boron-doping on the electron affinity and work function of diamond surfaces.

Boron is the most prevalent and well understood dopant in diamond. The boron acceptor state lies in the diamond band gap 0.4eV above the valence band. In The “Physics and Chemistry of Color” by K. Nassau, it was pointed out that nitrogen, aluminum, beryllium, boron, and lithium are the only known materials to readily enter the diamond lattice [89].

2.5. TECHNIQUES FOR CHARACTERIZATION OF CVD DIAMOND FILMS

To distinguish between the many structurally and compositionally different types of carbon films which could be deposited from the vapor phase is not an easy task, especially when trying to determine that a particular phase is absent. Numerous techniques are used to characterize diamond films. A brief overview of these techniques is given in Table 2-2. In some cases, different techniques are listed even though they may yield approximately the same information.

Table 2-2: Techniques for characterization of diamond (modified from [20])

Technique		Physical process	Type of information
Vibrational spectroscopy	Raman	Inelastic light scattering with lattice vibration which changes polarizability	Carbon bonding (sp^2/sp^3), structural perfection, stress state, crystal size [90]
	Infrared	Inelastic light interaction with lattice vibration which changes the existing dipole moment	Chemical bonding, absorption coefficient, refractive index, impurity
Electron spectroscopy	X-ray photoelectron (XPS)	Excitation and emission of electrons by x-rays	Surface species, bonding, electronic state
	Auger electron (AES)	Creation of an inner hole by incident electron subsequently filled by outer electron with the release of Auger electron	Surface composition carbon bonding type (sp^2, sp^3)
	Electron energy loss (EELS)	Electron energy loss by core level ionization, interband transitions or Plasmon excitation	Carbon bonding type (sp^2, sp^3), surface electronic structure
	Energy-dispersive X-ray spectroscopy (EDS)	X-ray created by incident electrons exciting an inner electron subsequently filled by an outer electron with the release of a characteristic x-ray photon	Quantitative elemental composition
Electron microscopy	Transmission electron (TEM)	High energy e-beam passing through a thin sample forming an image. Contrast determined by crystallographic orientation or atomic mass	Structural defects, crystallinity

	Scanning electron (SEM)	Scanning and focusing an e-beam over a surface and sensing the secondary	Surface morphology qualitative electrical conductivity
	Scanning tunneling (STM)	Voltage bias between surface and sharp tip causes electrons to tunnel to the tip thus relating current to position [81]	Surface structure with sub-nm resolution, charge density
Diffraction methods	X-ray (XRD)	x-ray elastic scattering with atoms (Bragg)	Structure identification, lattice constant measurement, crystal orientation
	Selected area electron (SAED)	High energy electrons scattering elastically with atoms	Structure identification, lattice constant measurement, crystal orientation
	Low energy electron (LEED)	Electrons backscatter elastically on the surface only (Bragg)	Surface structure, reconstruction
	Reflection high energy electron (RHEED)	Electrons backscattered elastically on the surface	Surface structure
Others	Secondary ion mass spectroscopy (SIMS)	Ionized surface atoms ejected by impact of high energy ions, then subjected to mass analysis	Elemental identification and distribution, chemical concentration depth profile
	Rutherford backscattering spectroscopy (RBS)	Collision of He+ ions with target atoms leading to energy transfer	Quantitative atomic composition, depth profile
	Spectroscopic ellipsometry	Multilayer optical techniques to deduce photon energy independent structural parameters	Layer thickness, densities, refractive index

The methods utilized in this study of diamond structures include SEM, EDS, XRD, FIB, SAED, and TEM.

2.5.1. Scanning Electron Microscopy (SEM)

Scanning electron microscopy is a technique to examine surfaces with sub-micron features. It operates by scanning a focused electron beam over the surface and detecting the secondary backscattered electrons emitted from the surface. The beam can be focused to achieve an ultimate resolution as small as 2 nm. The brightness of the image depends in part upon the local surface geometry due to the asymmetric location of the detector. Fundamentally, the brightness of the image is a function of the number of backscattered electrons. This yield is related to the electrical conductivity of the sample, thus making the SEM a useful tool to examine regions of varying electrical conductivity.

SEM has many advantages over optical microscopes in its high magnifications (~40x – 150,000x) and its extraordinary depth of field (500 times greater than optical microscopy). When compared to TEM, the SEM does not rely on transmitted electrons to form an image, and so bulk samples can be used, often without any sample preparation necessary. Highly insulating samples unable to diffuse electric charge can be coated with a thin film of a conductive metal such as gold.

2.5.2. Energy Dispersive X-ray Spectroscopy (EDS)

Many SEMs are equipped with EDS detectors. EDS is an analytical technique for the analysis of elemental composition and distribution of a sample which relies on analyzing characteristic X-rays emitter by the sample in response to bombardment with energetic electrons. Due to each element's unique atomic structure, the x-ray emissions can be identified uniquely from one another. The energetic incident electron excites an electron from an inner shell, ejecting it. An electron from an outer, higher energy shell, then drops in energy to fill the vacancy, releasing the difference in energy as an X-ray photon.

EDS is limited by a number of factors. EDS detectors generally cannot detect the first three elements of the periodic table: H, He, and Li due to detector design limitations. Light elements in general pose difficulties due to the low energy of their emitted X-rays which are either easily absorbed or lost to instrument noise. When an electron transition stimulates the emission of an X-ray photon, that photon is emitted in a random direction, but is detected only if it originates near the surface (so as to not be internally thermalized) and propagates towards the detector, thus detection efficiencies are low. New solid state detectors have reportedly eliminated the light element limitations by removing the protective layer over the surface of the detector which previously would absorb the low energy X-rays. In addition, these newer detectors are being used in arrays circling the sample with the goal of increasing detection efficiency by an order of magnitude.

Although each combination of X-ray energies may be unique to each element, specific energy peaks are sometimes shared by a number of different elements which can be differentiated only by observing collective sets of peak energies. It is this combination of peaks required to conclusively identify a material that makes the analysis non-trivial, particularly in samples with diversity in elemental composition, as a number of different elements may share one particular transition energy.

Often, instead of the outer electron filling the inner hole and emitting a photon, it can instead transfer that energy to a third electron leading to its ejection. This third electron is called an Auger electron, and analysis of these emitted electrons is known as Auger electron spectroscopy. If the excitation source causing the emission of an Auger electron is an X-ray photon, the technique is known as X-ray photoelectron spectroscopy (XPS).

2.5.3. X-ray Diffraction (XRD)

Diffraction techniques can provide direct information on the periodicity of a crystal structure. By studying the intensities of diffracted beams, information on the actual locations of atoms within the unit cell can be obtained. Unlike surface sensitive diffraction techniques such as LEED or RHEED, XRD is used to study bulk structures.

An XRD typically consists of an x-ray source, a goniometer, and detector/counter.

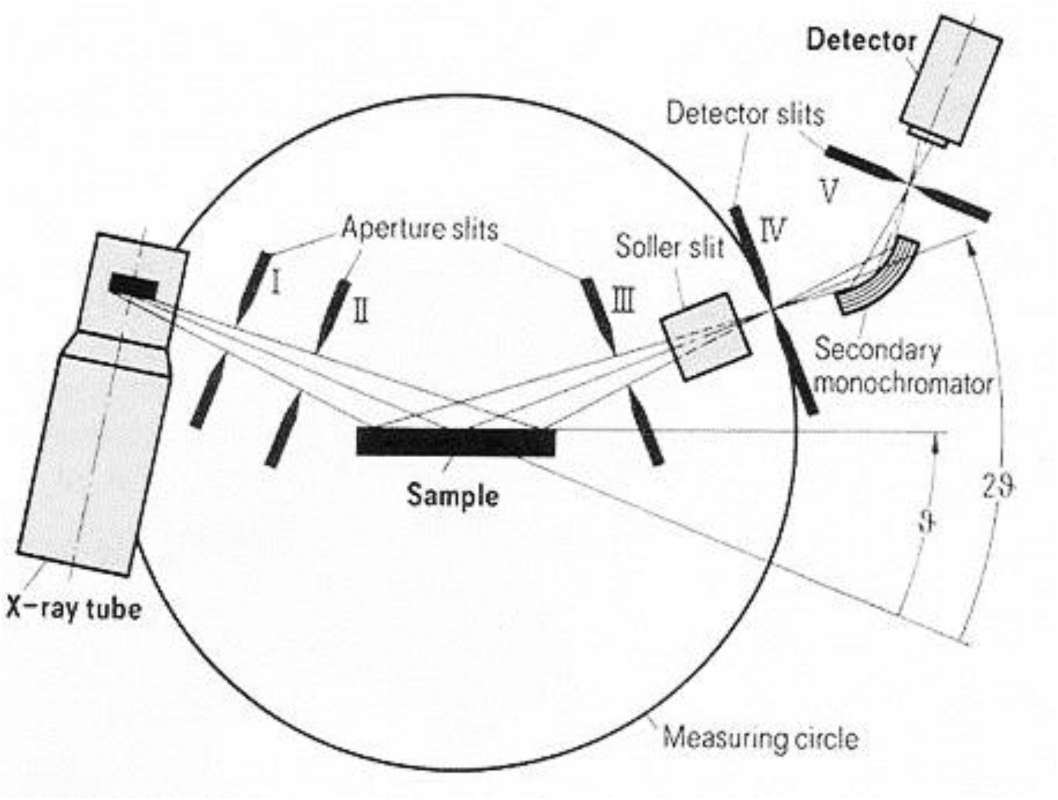

Figure 2-16: Schematic of an X-ray diffraction (XRD) system

Results are given in the form of a chart of peak intensity vs. 2Θ. This angle can then be converted into the inter-planar spacing using Bragg's law. XRD relies on Bragg's diffraction law [91]:

$$2d \sin\Theta = n\lambda \qquad \textit{Eq 2-11}$$

where 'n' is an integer representing a number of lattice planes, λ is the wavelength of the incident beam, 'd' is the distance between two lattice planes, and θ is the angle between the incident beam and the lattice. High accuracy in determining crystal orientation is generally possible, and sample preparation is easy. XRD is widely used for identification of crystal phases and crystal orientation.

The growth texture of CVD diamond films has been investigated by several researchers by x-ray texture analysis [92-94]. Observation of the subsurface crystal orientation has provided the basis for models of competitive crystal growth. The authors applied van der Drift's "evolutionary selection" model [95] to computer simulations to explain texture development in diamond films. The model assumes random nucleation orientations followed by competitive growth. The nuclei with the fastest growing crystallographic direction perpendicular to the substrate overgrows less favorably oriented ones leading to a texture with the fastest growing face normal to the substrate. With increasing film thickness, the fastest growing face increasingly dominates the surface. XRD observations of strong signals corresponding to the (220) plane guided the model to discover that <110> was the direction of fastest growth. This is only true, however, under the specific growth conditions that this group was working with. Clausing et al. [96] applied a similar growth model to different growth conditions and demonstrated directly that the growth texture can be controlled by manipulation of deposition conditions influencing the direction of most rapid crystal growth.

XRD has been used in situ to study the time evolution of diamond nucleation and growth on molybdenum substrates. Meilunas et al [97] monitored the Mo, Mo_2C and diamond diffraction wavelengths in situ during CVD growth. After one minute under diamond growth conditions, the sample was imaged by SEM and they found that nanocrystallites of molybdenum carbide had formed. As time progressed, the Mo signal dropped as Mo_2C signal increased. At 20 minutes, the Mo_2C signal stopped increasing, and a diamond (111) plane was detected. The final thickness of the Mo_2C layer was estimated to be 1.5µm.

2.5.4. Focused Ion Beam (FIB)

A focused ion beam instrument operates much the same way as an SEM, but rather than a beam of electrons, it relies on a finely focused beam of ions. The typical FIB consists of a source of liquid gallium (Ga) which is heated to a vapor and ionized to be accelerated through a series of electrostatic lenses. Figure 2-17 is a schematic of a FIB.

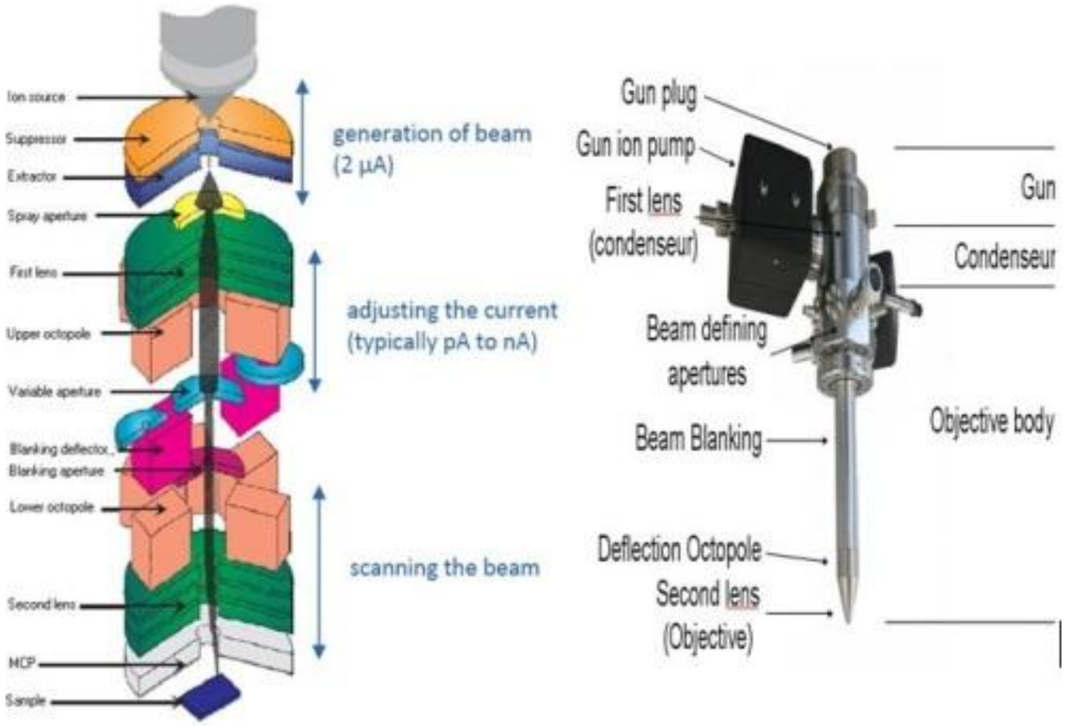

Figure 2-17: Schematic of a typical LMIS (liquid metal ion source) focused ion beam (FIB) column [98]

Following this effort's early work investigating FIB cutting in diamond, this effort has since required the additional capabilities of a dual-beam FIB. Dual-beam refers to an instrument with an electron acceleration column (SEM-like) attached to the focused ion beam column. In this way, the sample can be imaged by the less-destructive electron beam and reserve the ion beam for cutting only. Furthermore, many dual-beam instruments possess the ability to deposit platinum, tungsten, or carbon by electron-beam induced decomposition (EBID) of carrier gases. This capability turned out to be essential to surface preservation.

Interesting work is being done by McClelland et al. [99] to develop a deterministic focused ion beam source. Initial work has been done on chromium (Cr) due to their lab's experience with it and the availability of lasers with the appropriate wavelengths to cool Cr in a magneto-optical trap based ion source (MOTIS). The MOTIS can, with 98% certainty, produce a single ion and direct it to within 20 nm of a desired location.

2.5.5. Scanning Transmission Electron Microscopy (STEM/TEM)

A TEM employs an accelerated electron beam with a very short characteristic wavelength to image at extremely high resolutions. A series of electromagnetic lenses deflect and focus the electron beam. In addition to imaging the electrons that penetrate through the sample, a TEM is capable of analyzing backscattered electrons diffracting from the surface and of creating images from selected areas of diffraction, known as dark field imaging. Examination of electron diffraction patterns yields a reciprocal lattice of the imaged crystal.

Relative to other characterization techniques, TEM bears several important limitations. The basic requirement for a TEM sample is that it is thin enough (typically < 100 nm, preferably < 40 nm) to allow penetration of the incident electron beam to form an image. This nearly always requires difficult and time consuming sample preparation. The sample is vulnerable to radiation damage caused by the high energy incident electrons. TEM also requires a high level of user interaction. Whereas XRD or EDS analysis can be highly automated, no such automation exists for TEM. For many problems, there is no alternative but to turn to techniques such as TEM that may be destructive but nonetheless have the spatial resolution to directly access the microstructure.

The JEOL 2200FS at the Aberration Corrected Electron Microscope (ACEM) facility at Oak Ridge National Labs is a probe corrected STEM microscope. This instrument has an ultimate resolution of 0.07 nm, somewhat below the size of an average atom. Images have also been acquired on a Philips CM200 and a FEI Nova Tecnai G2. All of these are 200kV instruments.

The aberration correction on the JEOL system makes it the preferred TEM for this work, and thus most of the images here come from this instrument. The JEOL also has the capability of producing high-angle annular dark-field (HAADF) images. The HAADF detector forms a thick ring around the incident beam to collect only very high angle, incoherently scattered electrons, as opposed to Bragg scattered electrons. HAADF produces images with a very high Z-contrast, or sensitivity to atomic mass, as the intensity of the signal is proportional to Z^2.

Dark field imaging by TEM depends on imaging the patterns of Bragg diffracted electrons. Bragg's law is discussed in Section 2.5.3. Figure 2-18 and Figure 3-49 show diffraction patterns taken from a field emission tips. In a 200kV TEM, the incident wavelength used in the Bragg equation is 0.025Å in Eq 2-12.

$$1/d = 2/\lambda \ \sin\ \theta \qquad \textit{Eq 2-12}$$

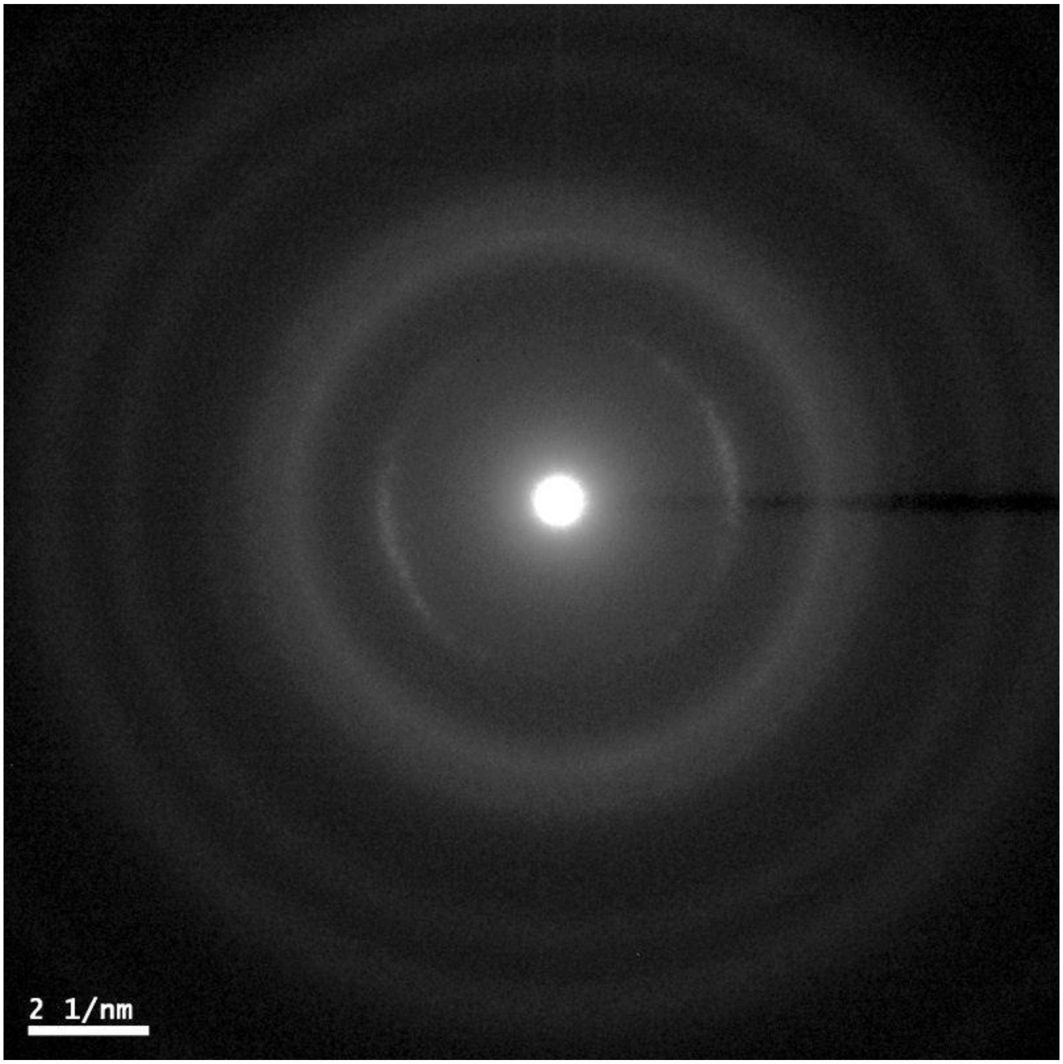

Figure 2-18: Diffraction pattern corresponding to the TEM image in Figure 3-33. The inner-most band corresponds to graphite spacings and the uneven "banded" structure is indicative of non-randomly oriented graphite.

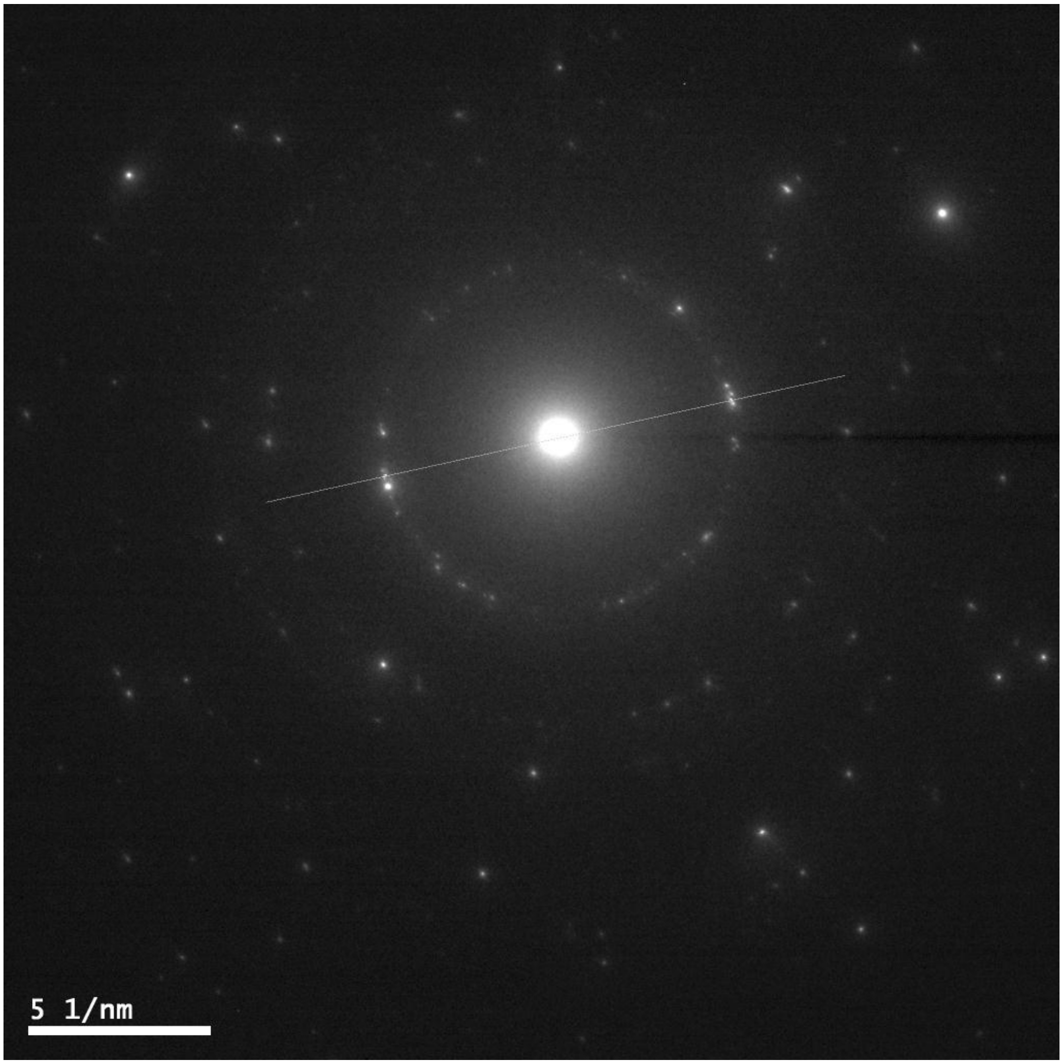

Figure 2-19: Diffraction from a microdiamond region of the field emitter tip. Here, note the near disappearance of rings, and instead bright spots from stochastically oriented grains. These spots are spaced at the same distances as rings seen in nanodiamond regions, but there are fewer crystals to contribute to ring blurring.

In the diffraction patterns, the innermost diamond ring corresponds to the 111 plane, with the next rings coming from the 220, and perhaps 311 planes. Not all planes are reflected in diffraction patterns because "diffraction occurs when the ray paths via successive planes in the system differ from each other by an exact number of wavelengths." [100] Ring patterns are generally consistent with crystals sizes less than 100nm as seen in Figure 2-18. Additional values for diamond and graphite plane spacing are in Table 2-3.

Table 2-3: D-spacing of diamond and graphite with their associated planes.

Diamond D-spacing (Å)	**Associated Plane**
2.061	111
1.261	220
1.0754	311
0.8916	400
0.8182	311
Graphite D-spacing (Å)	**Associated Plane**
3.55	001
2.13	100
1.82	102

CHAPTER 3

RESEARCH & RESULTS

3.1. EQUIPMENT

3.1.1. Field emission experiments

Field emission from diamond has been demonstrated in gated, ungated, and multi-gated cathodes at remarkably low fields [57, 101-109]. Diamond tips have even demonstrated current densities that approach the quantum degeneracy limit [110]. In the pursuit of ever brighter, longer lasting, and more uniformly emitting cathodes, the field emission experiments described here were intended to provide qualitative feedback to the array fabricators while routinely pushing the cathode's electron emission limits. For the first time at Vanderbilt, we have imaged field emission from diamond arrays with phosphor screens allowing study of the dynamic nature of emission and providing emission data for specific, individual tips.

Field emission experiments are performed in a large Perkin-Elmer stainless steel UHV chamber pumped by a Perkin Elmer TMB-X ion pump. The chamber is capable of achieving vacuum pressure better than the x-ray limit the of ion gauge used to measure it (~10^{-11} torr). During typical use, pressure was held between 10^{-8} – 10^{-9} torr. Besides the ion pump, the chamber also has an ExTorr XT100 residual gas analyzer (RGA).

Field emission experiments were achieved with a custom designed and built sample holder. A schematic is shown in Figure 3-1. Both plates are made of aluminum, chosen for electrical conductivity, vacuum compatibility, and reasonable cost. Between the two electrically conducting plates lies a "sandwich" arrangement of the diamond cathode array, a "picture frame" type electrically insulating spacer, and a conductive anode. The preferred spacer was a 270μm thick alumina (Al_2O_3) square with an empty center, thus "picture-frame".

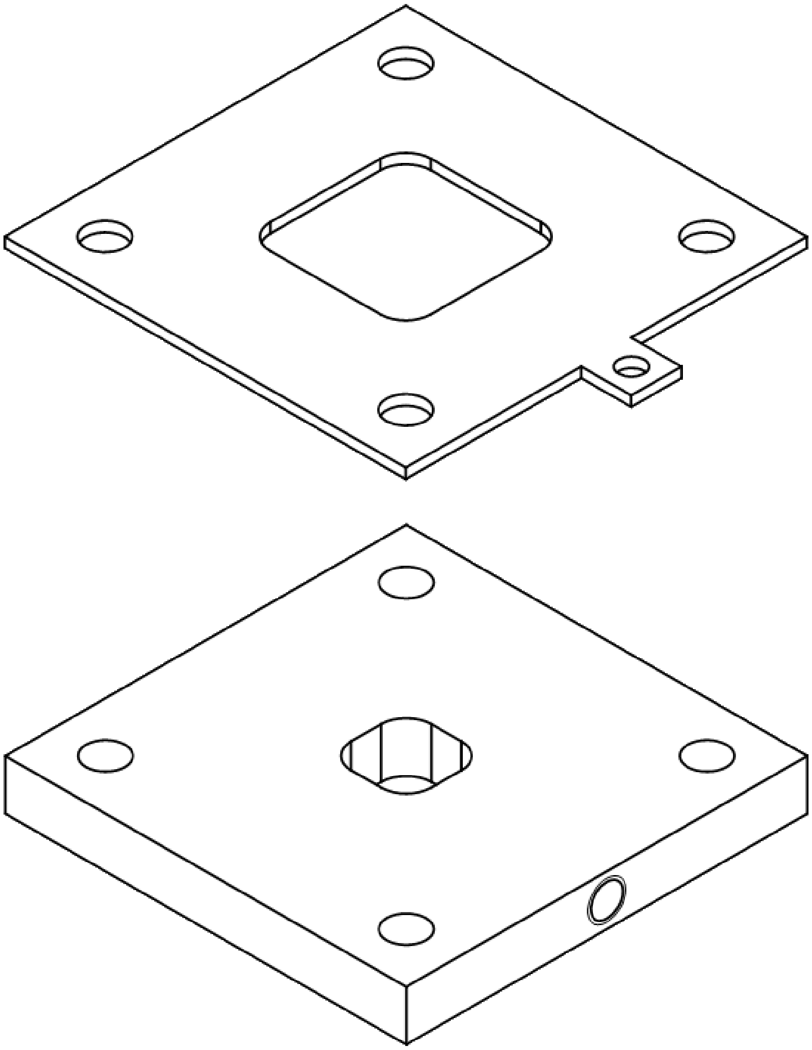

Figure 3-1: Schematic of sample holder used in field emission experiments. This is a fixed distance, close anode configuration.

The top plate permits the operator to view the back side of the anode. When a transparent phosphor anode is used, electron emission can be directly observed by stimulation of visible light photons in the phosphor. Assembled sample holder in use is shown in Figure 3-2. The points of light in the center of the white (alumina) square are emission sites lighting up the phosphor anode.

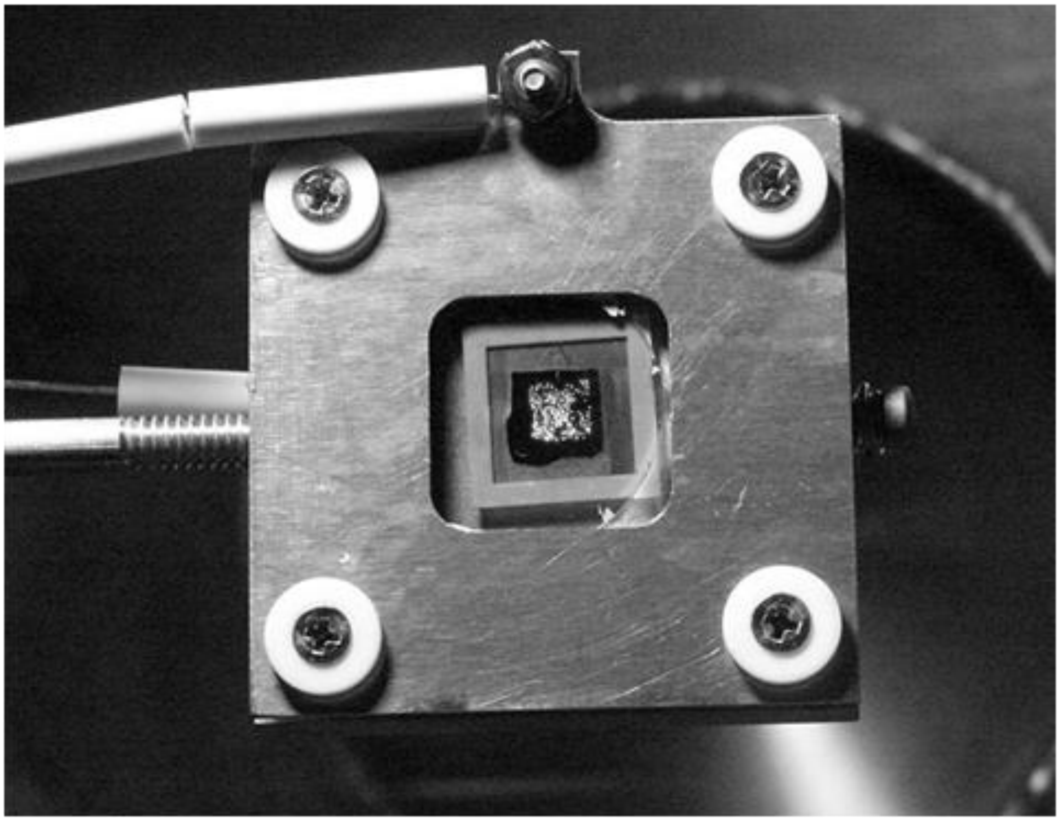

Figure 3-2: Field emission test apparatus in operation. Top aluminum plate is screwed in corners to lower plate, sandwiching cathode and anode between them. Anode electrical connection is visible top center. White inner frame is the alumina spacer. Dark region in the center of the image is the diamond film. Bright points of light in the center of the image are field emission sites

Voltage is applied by a Spellman RHR120W high voltage power supply with analog controls. It has a total output limit of 10 kV and 3mA.

Field emission currents have been measured by monitoring the voltage across a resistor with stated resistance values of 100 kΩ to 10 MΩ between the diamond cathode array and ground. Voltage across this resistor is monitored with a Fluke 289 True-RMS logging multimeter sampling at a rate of 1 Hz. The meter is unable to report results at a higher sampling rate, but for each sample it collects samples at a higher frequency and reports an average, maximum, and minimum value over the 1 second period. In extended emission tests, lower sampling rates were used, as low as one per 30 seconds.

3.1.2. Anode materials

High current field emission experiments have traditionally used a metal or silicon anode that does not allow direct observation of emission. In this way, only aggregated emission currents can be measured with no indication as to either the source of emission, or whether emission was distributed uniformly throughout the array. These experiments needed a durable, strongly conducting, and transparent anode. Thankfully, high sensitivity is not a requirement of a high current density experiment. Experiments with various phosphors (YAG:Ce, Y_2O_3:Eu, and $Gd_{1.5}Al_5O_{12}$:Ce) on (Indium Tin Oxide) ITO coated quartz plates showed reasonable durability, but the phosphors themselves were quickly disturbed or ablated. If e-beam deposition had been available for the deposition of these thin films, we may have achieved better adhesion, but lacking this ability; spin coating, drop casting, and precipitation from a liquid solvent were used.

A variety of choices of phosphor anode were used in this study. Zinc doped zinc oxide (ZnO:Zn) proved to be a very sensitive, bright, and fairly durable anode phosphor. Phosphor anodes were procured from Beam Imaging Solutions as microcrystalline powder e-beam deposited 10-15 µm thick on an ITO-coated 25mm diameter glass disc with the outer ring plated with aluminum. When procured in this way, phosphor anodes were $410 each, and thus reserved for low-field, short-term experiments. In an early high-field emission test, the anode suddenly failed in a catastrophic way, back-depositing large quantities of phosphor on the cathode (Figure 3-3).

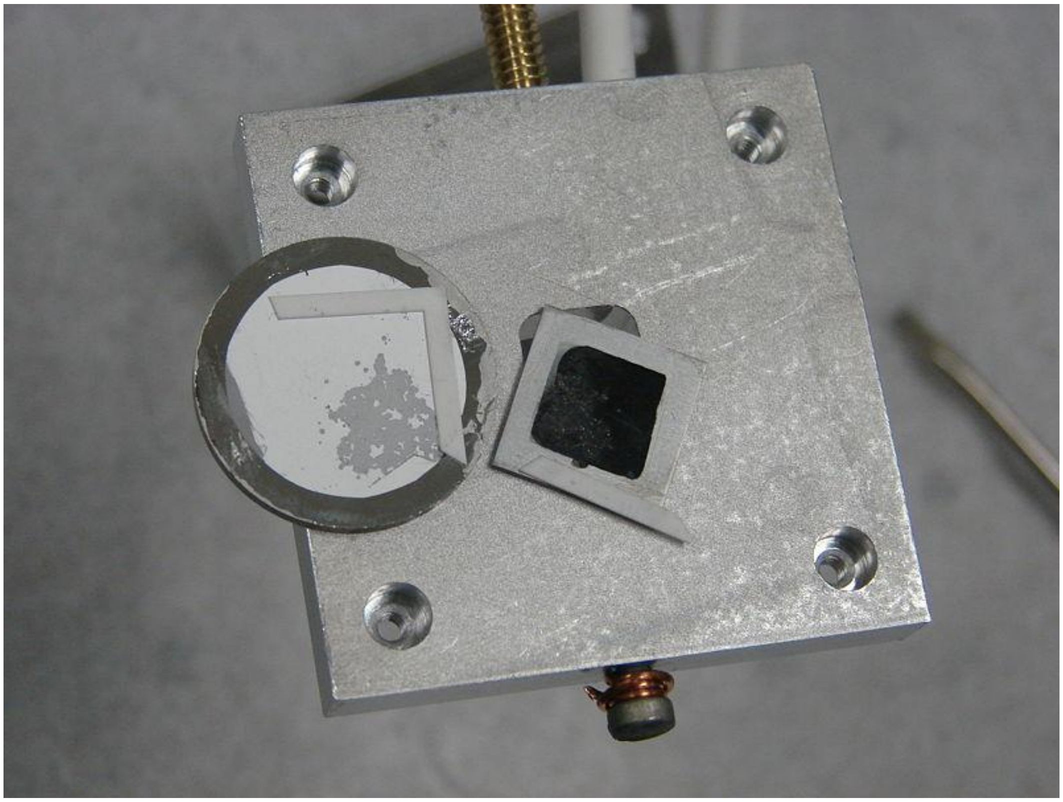

Figure 3-3: Photo of catastrophic phosphor failure leading to back-deposition of phosphor onto diamond cathode.

Interestingly, the anode plates continued to fluoresce even after the phosphors were blackened and gone. A little research and the use of an ITO coated plate without phosphor as anode revealed that glass and quartz exhibit a weak natural fluorescence under electron bombardment. While not suitable for long term experiments due to ablation of the thin, electrically conductive ITO layer, high current densities were measured with ITO coated quartz anodes.

Attempts at long-term, high current density experiments were not successful due to a lack of suitable anode materials. Two options have been considered but not yet put into practice due primarily to cost. Use of a solid YAG:Ce crystal as anode should provide the required light generation and optical transmission which retaining electrical conductivity and brightness even if the surface is mildly ablated. YAG:Ce has a history of use in electron scintillators and a reputation for brightness and durability. To sidestep entirely the anode degradation and associated cathode back-bombardment, we are considering a radio-frequency (RF) cavity in which fields are applied via RF rather than voltage on an anode. Suitable cavities have been identified in the hands of collaborators at Argonne National Labs, the Naval Postgraduate School, Los Alamos National Labs, and Raytheon Ktech. The first test of a diamond array in a RF cavity at Ktech did not produce measurable emission current, but notably did not self-destruct or cause damage to the cavity.

3.2. VANDERBILT DIAMOND FIELD EMITTERS

3.2.1. Fabrication process

The fabrication scheme for arrays of pyramidal diamond tips is shown in Figure 3-4. Conventional photolithographic patterning was used to define a mask array of squares on a (100) silicon wafer. The dimension of the square to become the base of the pyramids has been experimentally varied from 2 – 20 µm.

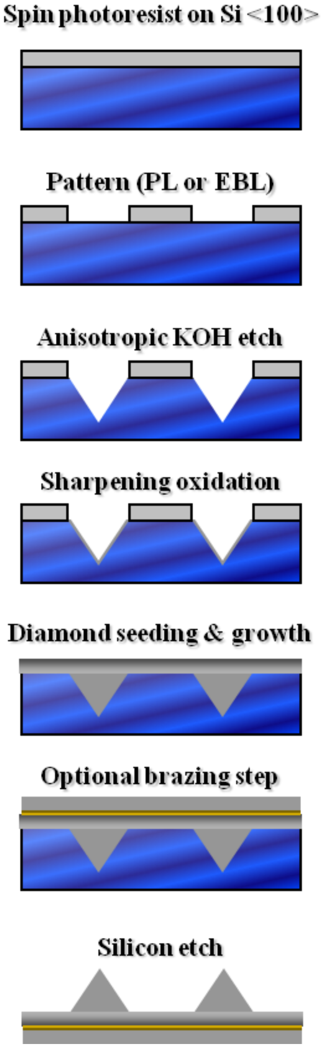

Figure 3-4: Fabrication process steps for ungated diamond field emitter arrays

To form an inverted pyramidal structure, the silicon wafer was anisotropically etched using potassium hydroxide (KOH). KOH etch rate on the silicon <111> plane is 1/400th that of the (100) plane and thus a pyramidal cavity comprised of four <111> planes is formed. Because the aspect ratio of the tip is determined by the angle between (111) planes in diamond, the apex angle of the pyramid is inflexible and is fixed at 70.6°. The final result of the etching process is shown in Figure 3-5.

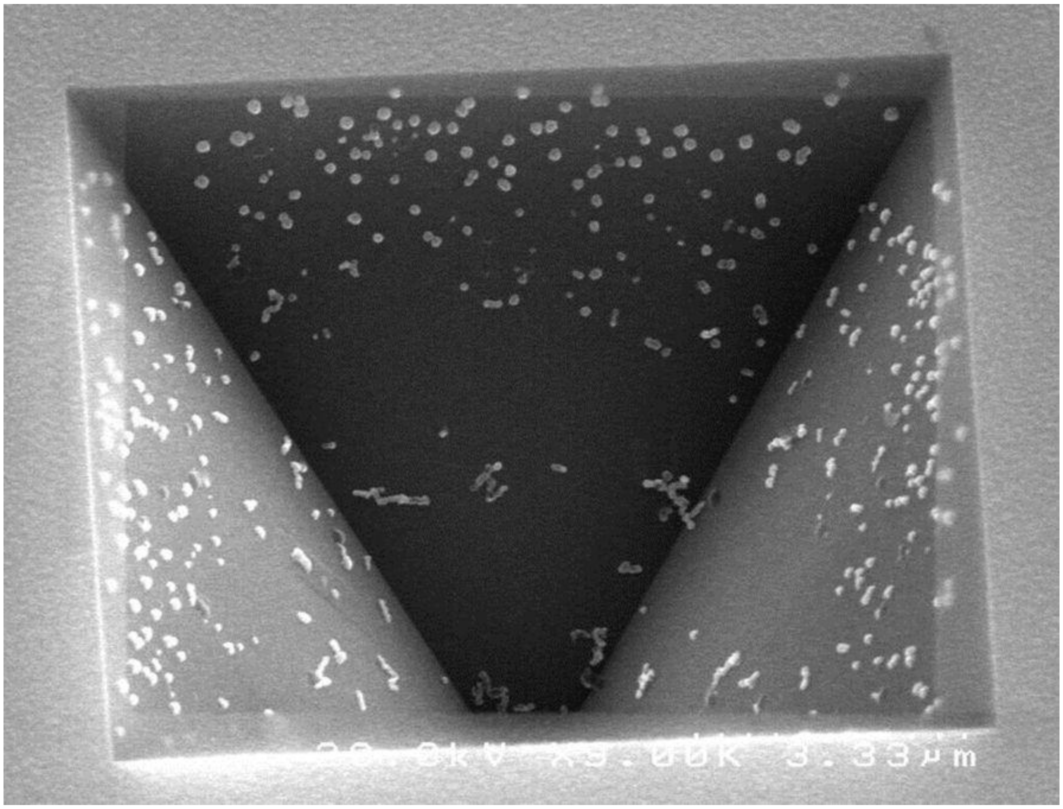

Figure 3-5: KOH etched pit in silicon wafer in preparation for diamond growth. Bright features in the pyramidal mold are believed to be SiO_2 *residue. Image provided by the Davidson lab.*

SiO_2 was then grown in the cavity via a wet thermal oxidation to achieve mold sharpening. Because the oxide grows preferentially on planes rather than edges, this has the effect of swelling the planes of the pit, enhancing sharp features as shown in Figure 3-6.

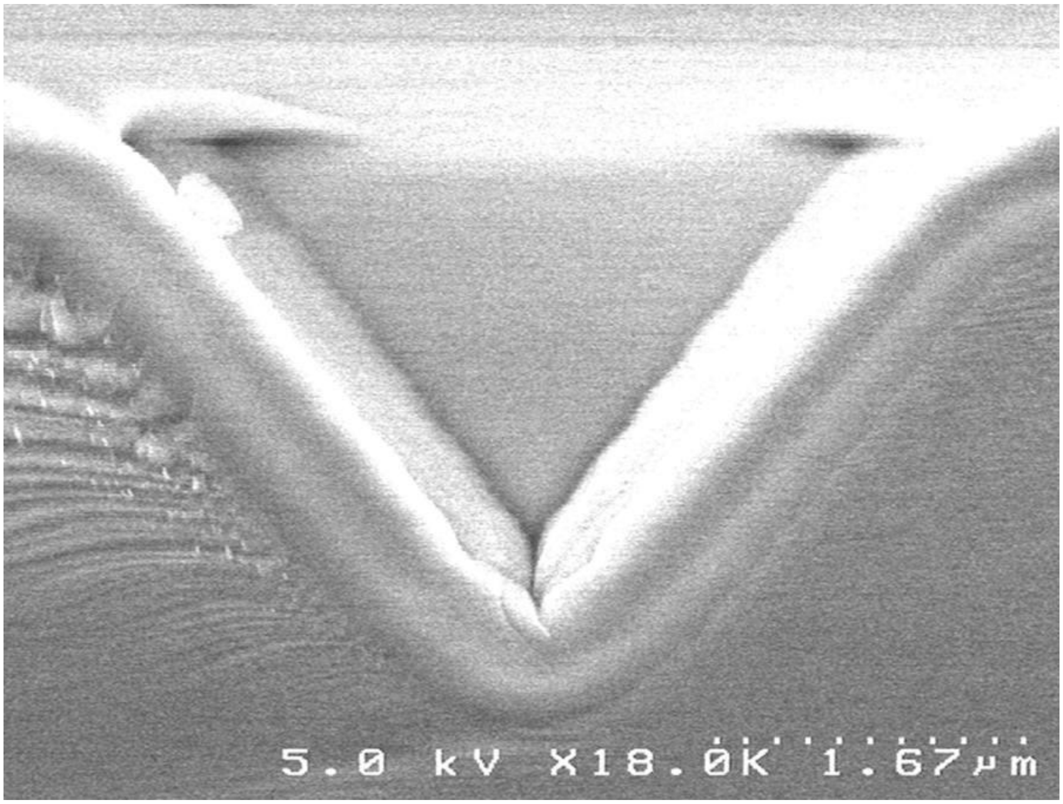

Figure 3-6: Etch pit in silicon following sharpening oxidation. Image provided by the Davidson lab.

Investigation into a "double oxidation" procedure have shown that by oxidizing the etch pit, removing the oxide, and growing another oxide, it is possible to retain a sharp tip while blunting sharp edges at the intersection of the sides of the pyramid thus removing potential spurious emission sites. Recent experiments have explored the feasibility of a shorter KOH etch, which leaves the etch pit incomplete with a square base instead of a sharp point. Since the oxidation process is faster on a plane than an edge, this structure swells at the base under oxide growth resulting in 4 tips per pyramid instead of 1 as shown in Figure 3-7.

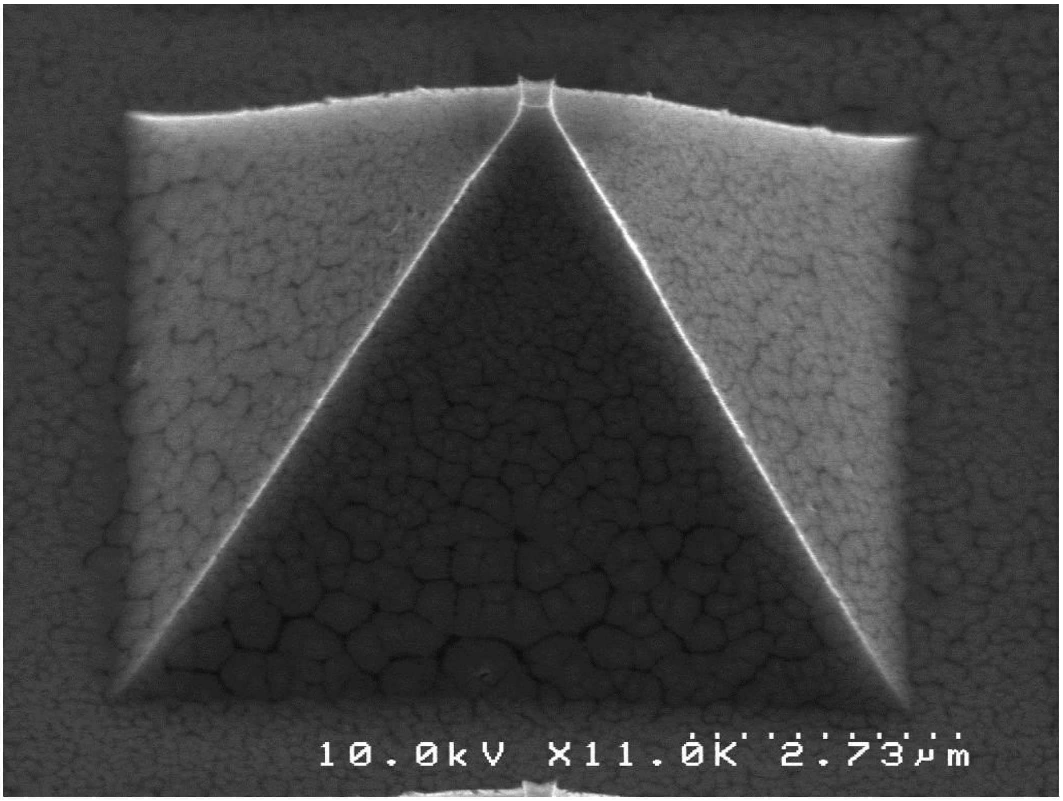

Figure 3-7: SEM image of a pyramidal tip with 4 tips courtesy of Jonathan Jarvis.

The nucleation step is performed by applying nanodiamond slurry to the SiO_2 surface. This provides both defect sites favorable to diamond growth and small diamond grains on which further growth is favored. The nucleation method is a critical step of diamond growth that has only recently moved from the realm of an art to a science. Most arrays at Vanderbilt have been prepared by mechanically abrading the surface with nanodiamond slurry followed by ultrasonication in a nanodiamond particle solution.

Next, diamond was deposited on the inverted silicon mold by Microwave-Plasma-Enhanced Chemical Vapor Deposition (MPE-CVD). In order to grow diamond, which is thermodynamically less stable than graphite, CVD methods have been developed that require a volatile hydrocarbon, an energy source, and an abundant source of atomic hydrogen. The growth medium hydrocarbon is CH_x, typically a methane (CH_4)-containing plasma. Atomic hydrogen drives the reactions that prepare the CH adsorption site by removing a hydrogen atom from the hydrogen-terminated diamond surface and abstracts the hydrogen atoms from the adsorbed CH_4, thereby permitting the carbon atom to move into the position corresponding to an extension of the diamond lattice.

Additionally, atomic hydrogen preferentially etches the graphitic phase. By using a plasma containing 98-99% H, it is possible to grow diamond films that are largely free of non-diamond secondary phases. However, atomic hydrogen also etches the diamond phase, resulting in the formation of voids and a columnar morphology. The growth rate is increased and grain size can be reduced to <100 nm by increasing the CH_4/H_2 ratio in the plasma, but non-diamond carbon phases are introduced. Nitrogen is commonly introduced to the hydrogen plasma to disrupt the growth of large single crystals thus increasing the renucleation rate and correspondingly improving the ability of the film to coat conformally while reducing film roughness. Nitrogen is incorporated in substantial quantities and is thermodynamically primarily in tetrahedrally coordinated sites at grain boundaries [111].

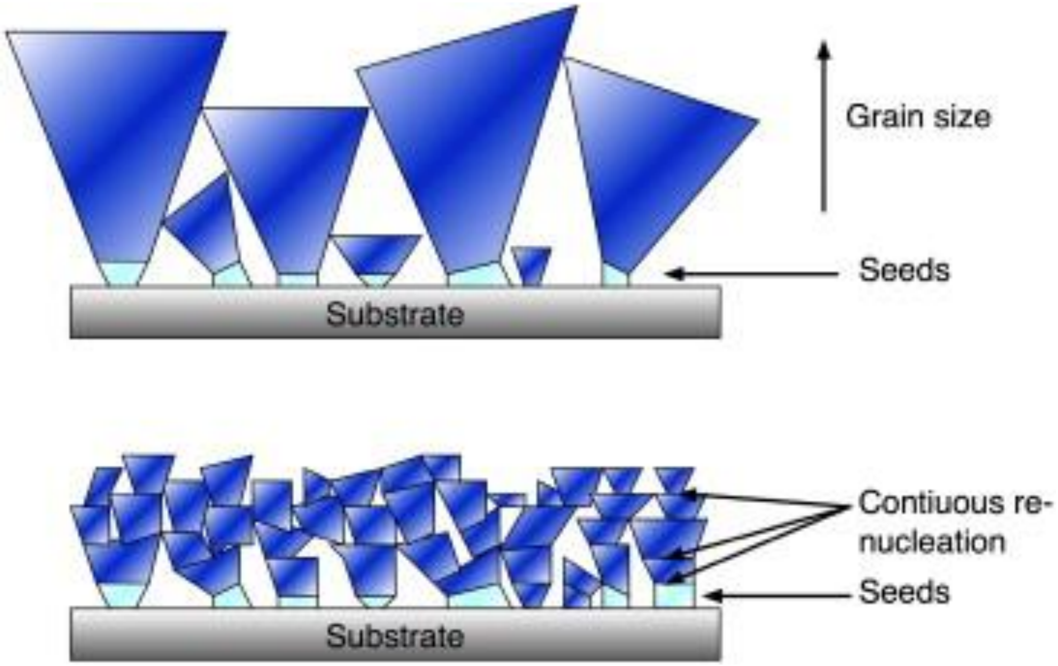

Figure 3-8: Comparison of diamond growth as affected by nitrogen in the growth process which causes continuous interruption of the grain growth and thus a high renucleation rate. Graphic borrowed from a presentation by Dr. Oliver Williams.

Following diamond growth, the diamond film is brazed to a polished metal plate (typically tungsten or molybdenum) for ease of handling, structural reinforcement, and electrical contact. The preferred braze material is an alloy of titanium, copper, and silicon (aka TiCuSil or CuAgTi). The braze components are shown in Figure 3-9.

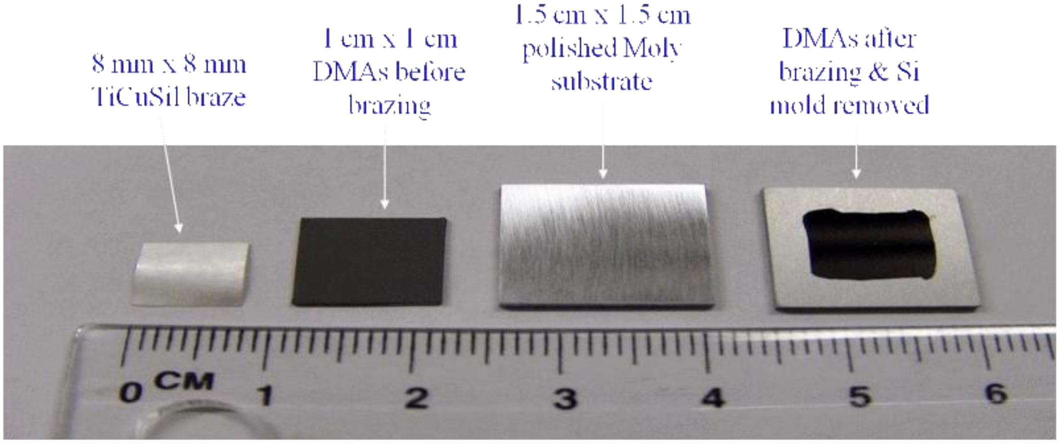

Figure 3-9: Braze components for arrays produced at Vanderbilt University.

The silicon and oxide is then completely etched away by a buffered oxide etchant (HF:HNO_3). The etchant leaves behind an exposed array of polycrystalline diamond pyramidal tips. Nanodiamond pyramidal arrays with tip densities up to 6.25 million tips/cm^2 have been fabricated. The arrays preferred in this study have a tip to tip spacing of 100µm intended to minimize neighbor shielding effects and enabling analysis of individual emission tips. Tip densities are routinely a hundred-fold larger to achieve extremely high current densities, but for this study, high emission currents and beam overlap complicated analysis of individual emitter contributions.

3.2.2. Diamond field emission vs. silicon

Diamond arrays outperform equivalent silicon tip arrays with 100x current densities at 1/10th the field [112]. Dr. Marco Alves, et al have published recent field emission data on silicon field emitter tips. The work is notable due to the substantial similarity in the fabrication processes to the emitters created at Vanderbilt. Pyramidal silicon tips of similar dimensions were demonstrated that exceeded previous records for field emission current per tip. Diamond field emitters, by comparison to the work by Alves et al, have achieved an order of magnitude more emission current per tip at 1/100th the field. This dramatic advantage due to diamond is apparent in comparison of current-voltage curves of the two emitters in Figure 3-10.

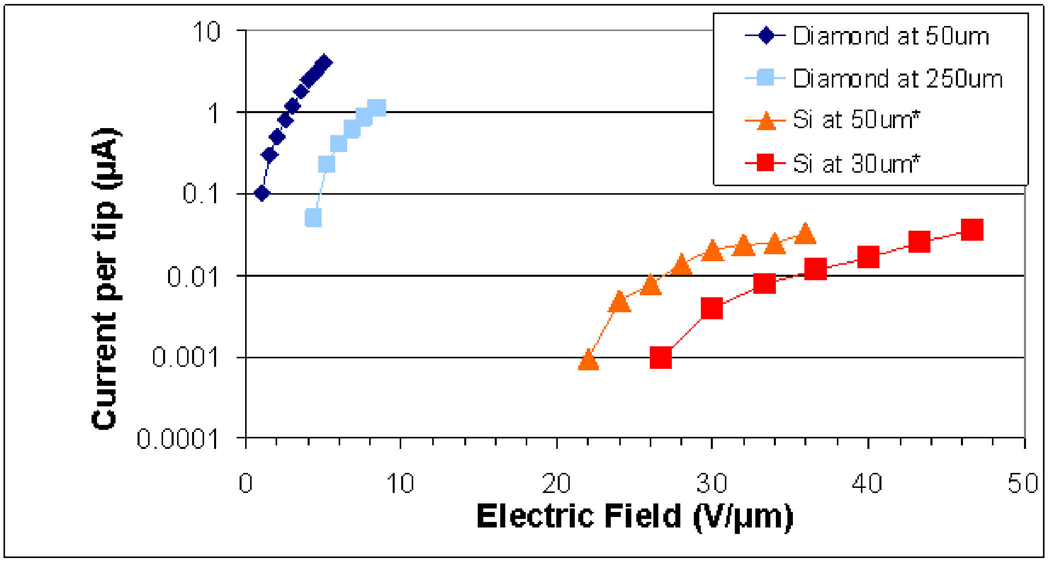

Figure 3-10: Diamond field emission current per tip as compared to silicon emitters of similar dimensions by Alves et al. [112]

3.2.3. Diamond field emission vs. metal

Diamond field emitters also compare favorably to the current state of the art in high current density metal field emitters. In recent work by Qi et al. [113], we observe that lanthanum hexaboride (LaB_6) field emitters can approach within an order of magnitude of the current density of diamond field emitters. It is worth noting however, that these current densities require 1,800x the applied field of those used for diamond arrays. Even with the sharp cone structure, the operating voltage of a metal cathode is comparatively very high, since the field enhancement factor is limited to 100-500 by the practical limits of current technology in making sharp metal tips.

It is also relevant to note that in the event of a tip ‘failure’, the diamond emitter benignly becomes dark on the anode screen with nearby tips and the overall array operation continuing unaffected. Even in our most dramatic of failures in which the tip is completely obliterated, other field emission tips only 7µm away continue functioning. An example of is shown in Figure 3-11 and Figure 3-12. By comparison, metallic cathodes typically fail in a disruptive plasma burst, contaminating or destroying the area and the emitter device.

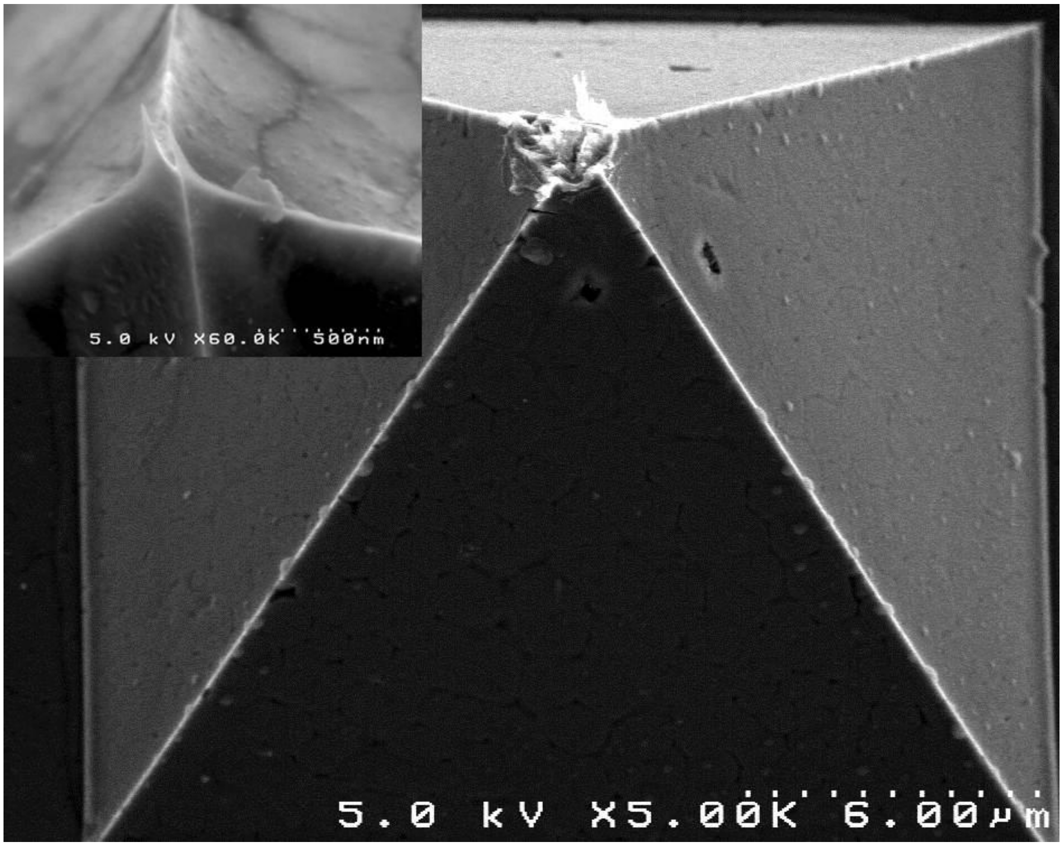

Figure 3-11: SEM of tip failure. Inset is same tip prior to testing.

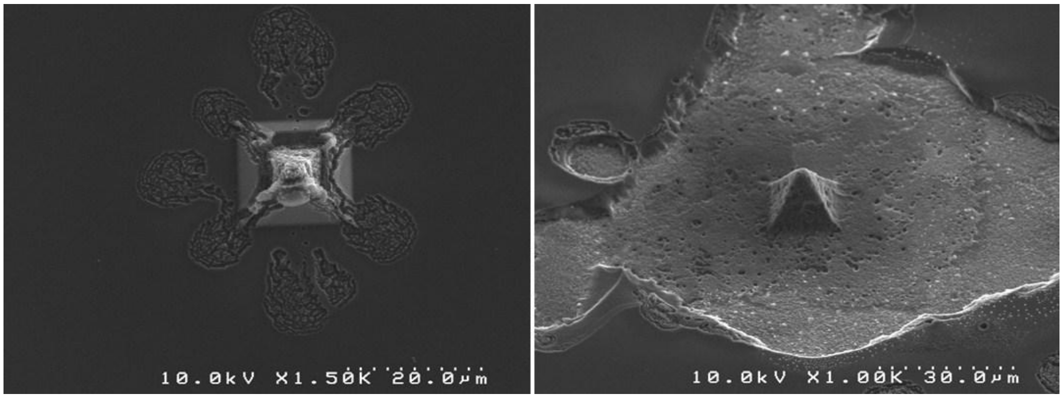

Figure 3-12: SEM images of tips destroyed in dramatic failure events during emission at very high fields.

3.2.4. Polycrystalline diamond emission vs. single crystal

Dr. Taketoshi Yamada et al. [114-116] have fabricated arrays of conical diamond field emitter tips to explore optimization of tip density as well as measure field emission from single crystal emitters. The Yamada group succeeded in fabricating nano-scale tips on single crystal diamond plates by plasma etching. Three configurations of tips were fabricated from a diamond plate of type IIb (boron doped) single crystal diamond (100) with a resistivity of 1 kΩ-cm. Aluminum dots were patterned to form a mask for diamond etching. Both dot size and dot spacing were varied in this study, from 1-2µm diameter spaced at 1.7-5µm. Tip radii were observed to be ~20nm with a tip height of 1,500nm. Field emission per tip and turn-on field were found to be similar to the polycrystalline CVD diamond tips made at Vanderbilt University. Only the highest density "whisker" configuration experienced nearest neighbor shielding which restricted emission to 1/10th that of the more widely spaced emitters. Experimental proof was offered for the theory [117] that the tip spacing should be kept to at least twice the tip height.

Toshimichi Ito et al [118] have also explored alternate configurations for fabricated single crystal diamond field emitters.

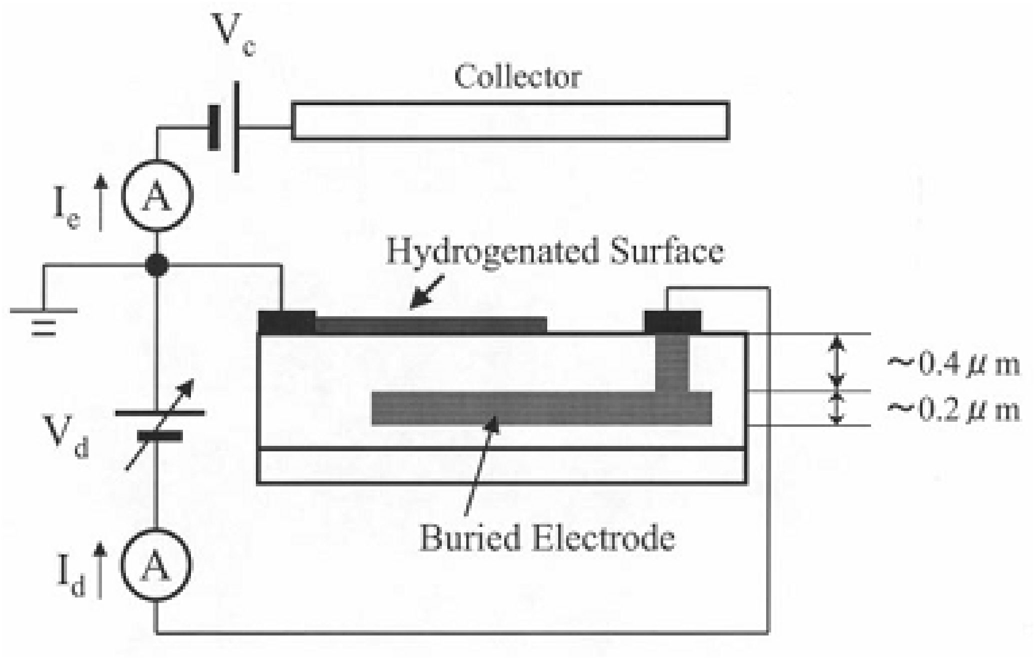

Figure 3-13: Nitrogen incorporated diamond field emitter cathode buried beneath 400nm of intrinsic diamond

3.3. ARRAYS HANDLED

Nanodiamond pyramidal arrays of 1 to 3,000,000 tips with tip densities of 2,500 to 6,250,000 tips per square centimeter have been fabricated at Vanderbilt University. The base of the pyramidal cathode tips ranged from 2 – 20µm. Smaller tips enable a higher tip density while larger tips are empirically observed to withstand higher per-tip currents. Spacing between tips ranged from 4 - 200µm.

It is generally accepted that there are optimizable limits to the tip sizes and densities. Arrays with tip spacing less than twice the tip height appear to suffer from nearest neighbor field shielding [116]. In this case, the field concentration gained by producing a sharp tip (high β) is diminished due to insufficient space between tips to allow the macroscopic applied field to reach the planar surface between tips. In similar fashion, larger tips provide a potentially greater field enhancement, but limit the number of emission tips per unit of cathode area.

The arrays used in this work were typically much smaller than the maximum array size because ultimate amperage and current density were not the priority. Instead, an ability to observe each tip individually and assess its physical and electrical properties was facilitated by low tip densities and small arrays. Square arrays of 5x5 or 10x10 tips strike a good compromise of having enough tips to measure while still being feasible to make a detailed study of each individual tip. When tip-to-tip spacing was 100µm or more, observation of individual tip activity was possible. Tip spacing in these selected arrays are commonly 100µm or 200µm.

3.4. FIELD EMISSION OBSERVATIONS

3.4.1. Predictions made by geometric evaluation

Gross emitter structure is clearly important to field emission. In one early array study of 25 tips, predictions of field emission behavior were made based on SEM images prior to emission testing. Emission predictions are shown in Figure 3-14(a). Five of the tips were single tips, 16 were double tips (example in Figure 3-15), and the remaining 4 were blunt or deformed. Single tip and double tipped emitters have been observed to emit comparably at low fields. Tips 17, 19, and 24 were dull did not emit nor were expected to emit.

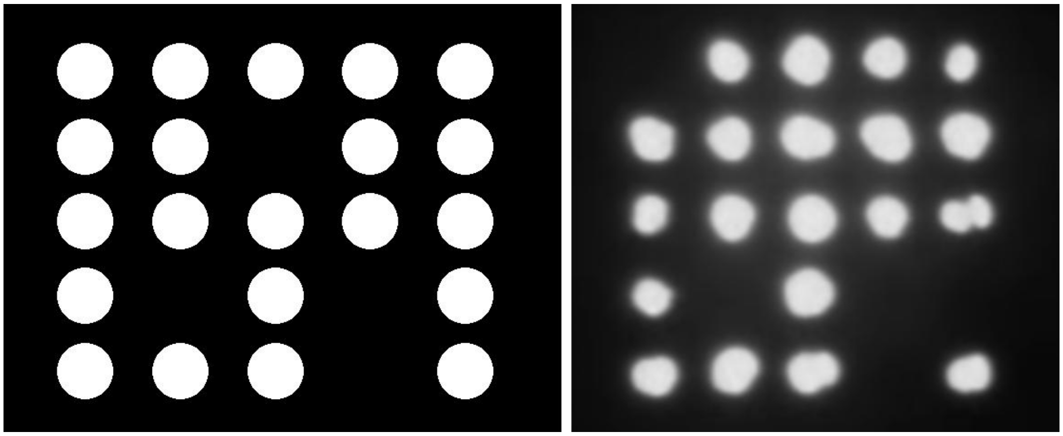

Figure 3-14: (a) Emission prediction based on SEM examination; (b) photograph of actual emission pattern. Prediction was correct in 22 out of 25 cases.

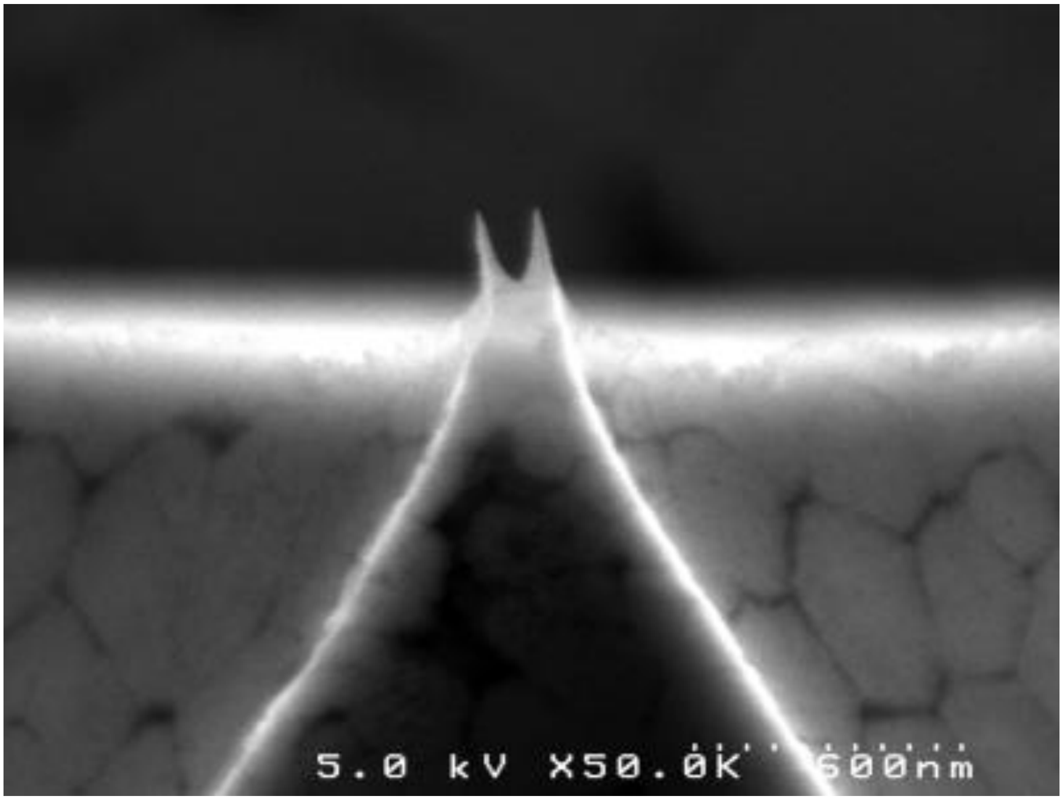

Figure 3-15: Diamond field emission tip with the non-ideal double tip configuration. Incidence of double tips has been ameliorated by purchase of a tighter tolerance photolithography mask.

Predictions made by evaluation of this emitter array by SEM proved accurate in 80% of tips. A photograph of the phosphor screen during emission is shown in Figure 3-14 (b). Geometric evaluation led to a correct prediction for 22 of the 25 tips. It has become fairly commonplace that the occasional tip will not emit as well as expected, as is seen with tips 1 and 20.

Much rarer are tips that do not have ideal shapes and still prove to be capable emitters. Only tip 8 (Figure 3-16) emitted when it was not predicted, but closer evaluation reveals that although it does not have the desired shape, it does in fact have a sharp feature which apparently proved sufficient for emission. Tips structured like this are not expected to be very durable.

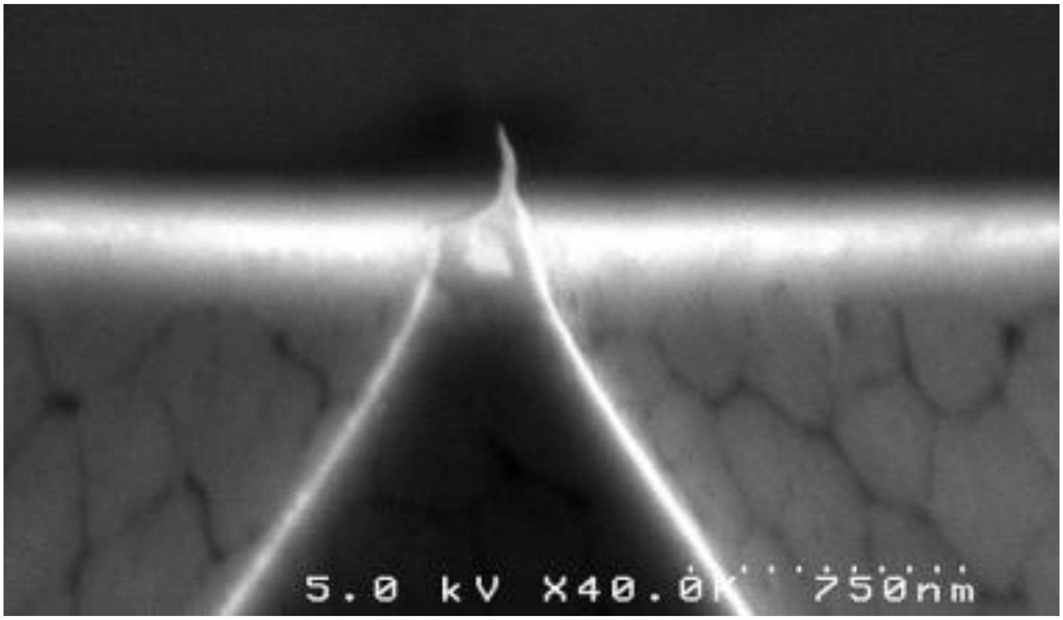

Figure 3-16: SEM of diamond field emitter tip which was not expected to emit. Sharp feature proved adequate for field emission, though tips of this configuration are not expected to be durable.

3.4.2. Array recovery with atmosphere exposure

It has been observed on many occasions that the field emission current degrades over time. This emission decay rate is observed to be field-dependent and has been observed to decay exponentially with a half-life on the order of hours as in Figure 3-17 and Figure 3-18. Scanning electron microscopy (SEM) images taken of the arrays before and after an extended period of emission have resulted in mixed conclusions.

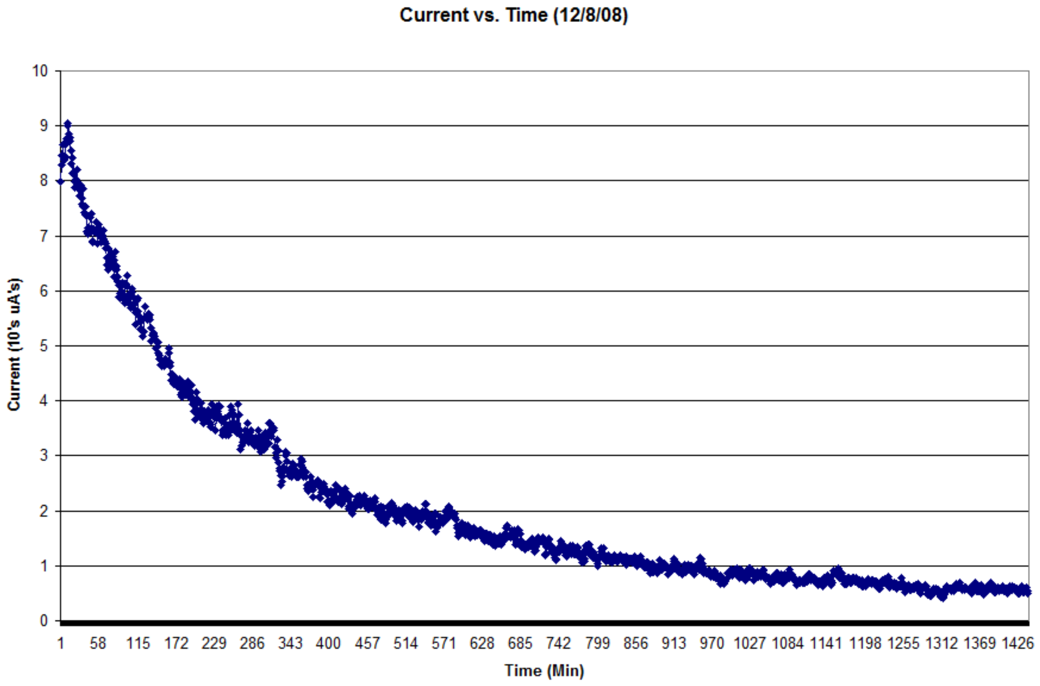

Figure 3-17: Field emission current decay over 24 hours of a 1,764 tip array plotted on a linear Y-axis

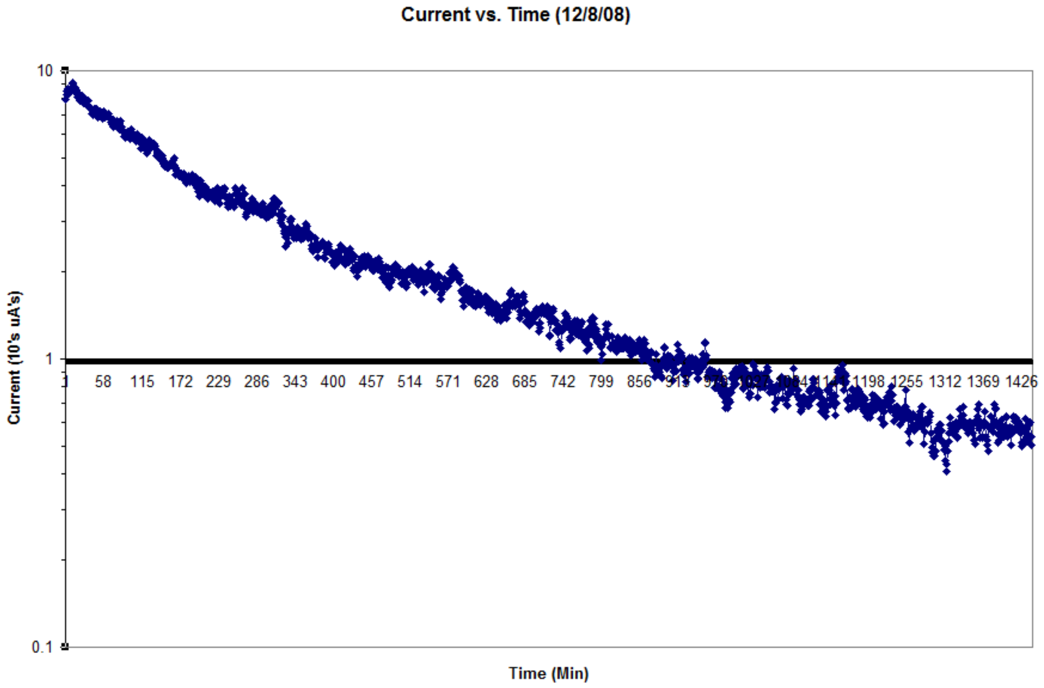

Figure 3-18: Field emission current decay over 24 hours of a 1,764 tip array plotted on a logarithmic Y-axis

Lacking sufficient data to this effect, the theory and opinion of those involved is that emission decay effect is the result of at least two simultaneous effects. In the instances where tests were performed at high current densities, the tips have been observed to progressively lose their sharp tips over time [119]. At lower emission densities, emitter shape as observed by SEM does not appear to change, but the emission current degrades over time nonetheless. This low-current loss of emission current has been tentatively associated with the loss of emission enhancing adsorbates.

Under certain conditions, the array is observed to recover from this decay. Theoretical approaches to this recovery seem to be conflicting [120, 121]. In the case of a particular 1,764 tip array that was handled in late 2008, Figure 3-19 shows an SEM of the array taken prior to any emission testing. Close inspection revealed that the majority of the tips were not well formed. Inspection of every tip was not performed due to the immense size of the array and the impracticality of cataloging each tip's state.

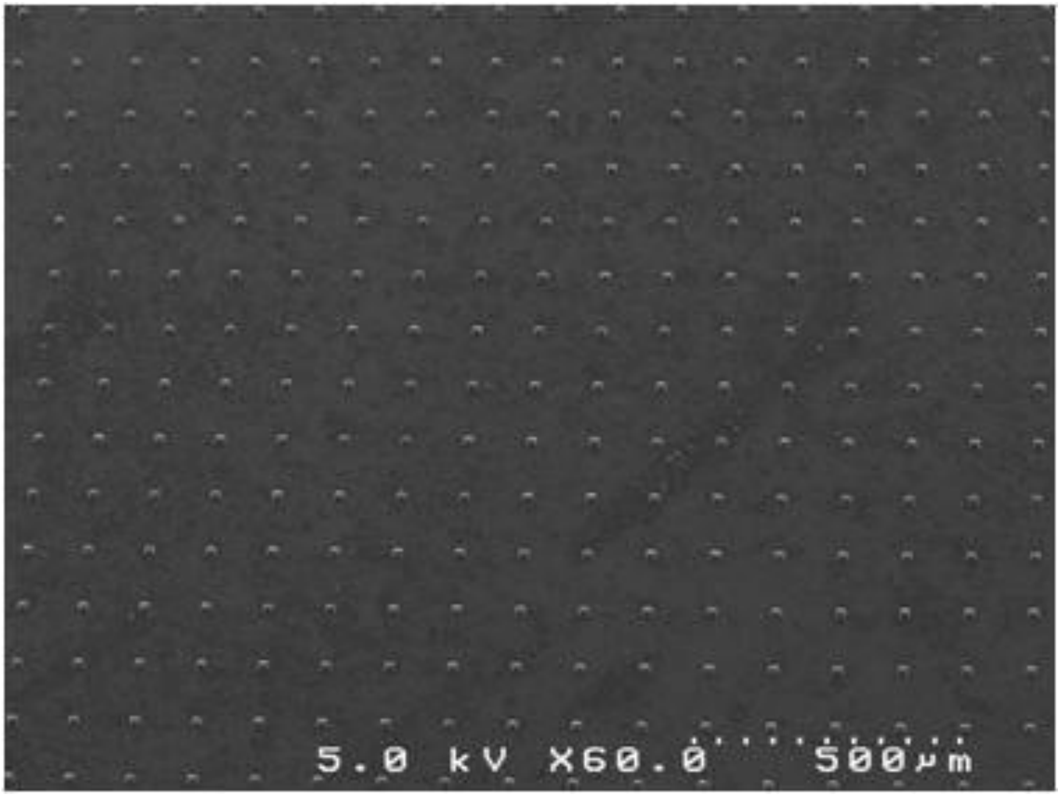

Figure 3-19: Low magnification SEM of a (42x42) 1,764 tip array.

Emission was observed to begin at 2 V/µm (15 nA at 550V with a anode spacing of 250 µm). At 1,330V (5.3 V/µm) Figure 3-20 shows the array glowing brightly if not particularly evenly. At an applied field of 7.2 V/µm, the array reached 1 mA of current. Later tests at fields up to 8.4V/µm yielded emission currents up to 2.6mA (shown in Figure 3-21).

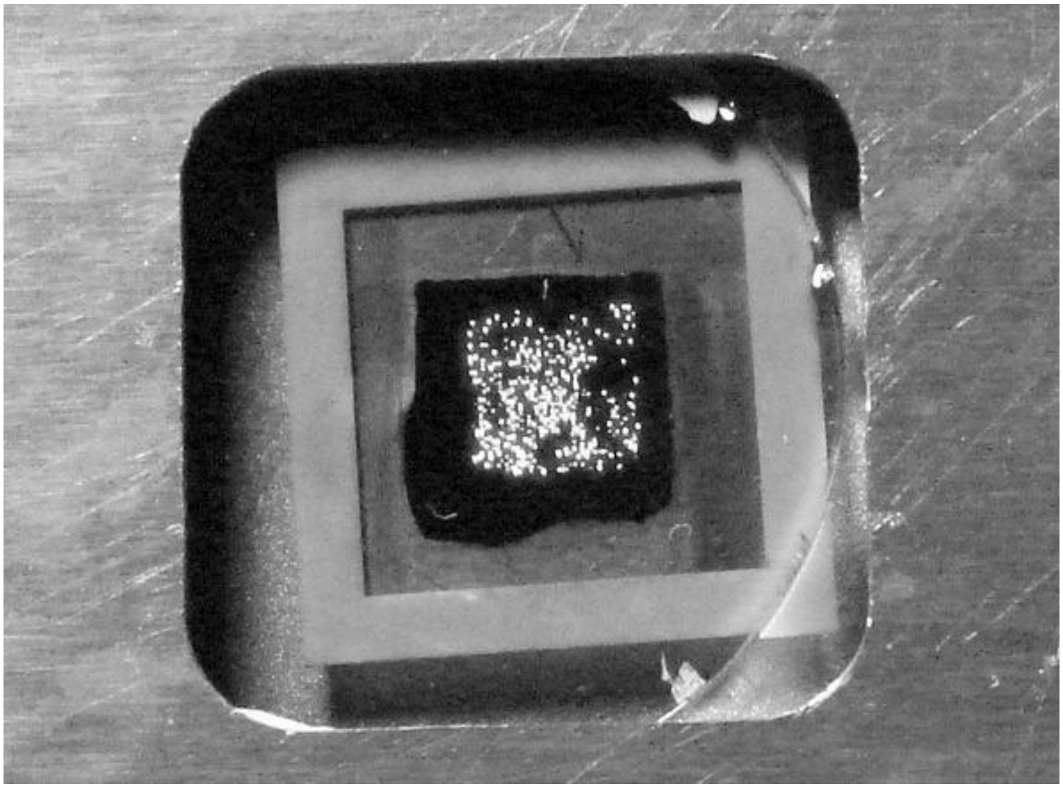

Figure 3-20: Photograph of 1,764 tip array lighting up phosphor.

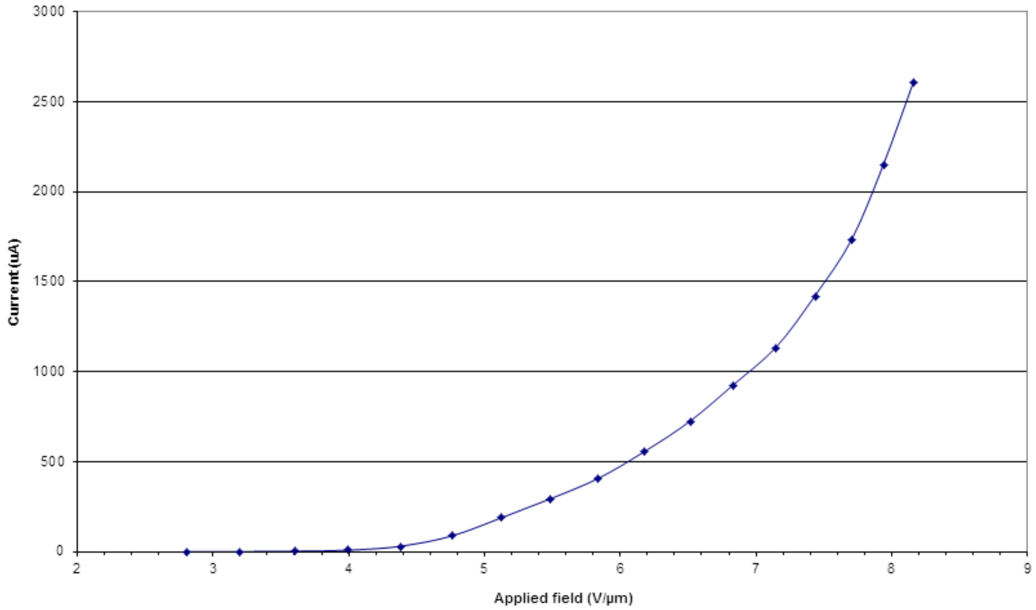

Figure 3-21: Plot of current vs. field for a 1,764 tip array shown in Figure 3-20. Peak emission current is ~2.6mA.

The 1,764 tip emitter array was tested for 24 hours with an initial emission current of ~11 µA. Notable emission decay occurred as seen in Figure 3-22. Once it was established that this array was going to be interesting, a limited catalog of tips was performed in the SEM. This required removing the array from the chamber, thus exposing it to atmosphere. Three days passed before it was returned to the chamber and high vacuum.

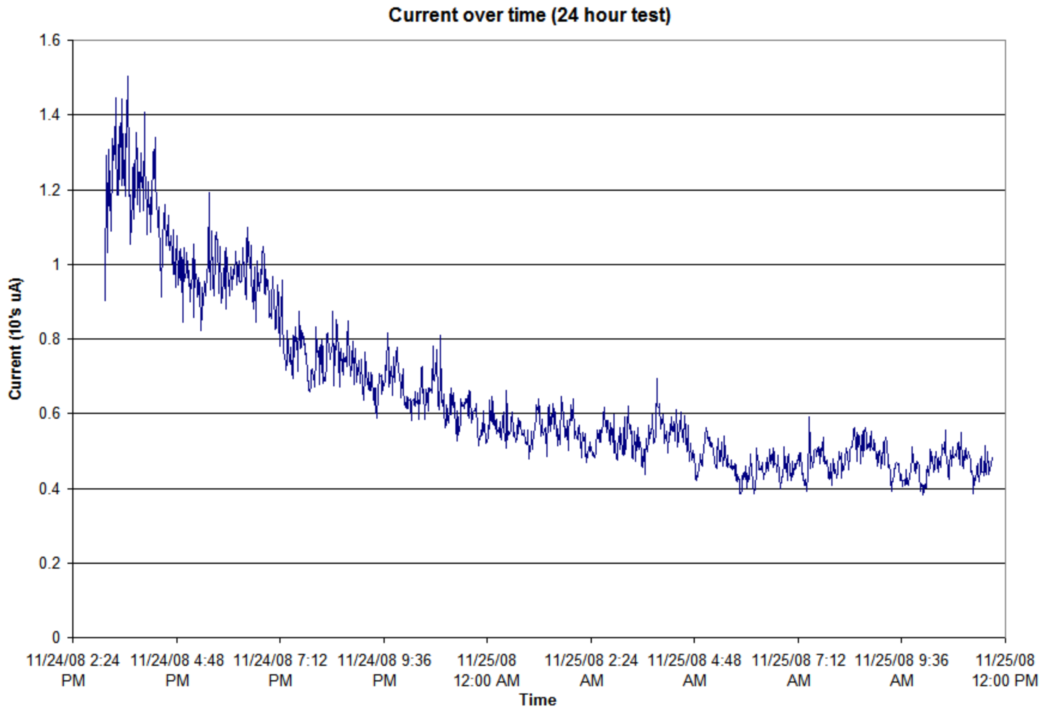

Figure 3-22: Current vs. time for the first 24 hour test of the 1,764 tip array. Emission current is observed to decay from 11uA to 5uA.

The current-voltage relationship was measured prior to beginning another 24-hour test. Remarkably, the I-V values correlated well to the first I-V measurement on this array prior to any extended testing (Figure 3-23). The emission properties of the array were apparently completely restored by the trip to atmosphere and the SEM. I-V curves taken before the 24 hour emission run and after atmosphere exposure are indistinguishable from each other. This strongly implies that the emission current decay is not due to irreversible tip structure changes. Because these emission tests are performed with a transparent phosphor anode, we can be assured that the observed current is from the array and is not being confused with leakage or spurious emission sites. In addition, reverse bias tests are routinely performed to be certain that leakage currents are not contributing to measured emission.

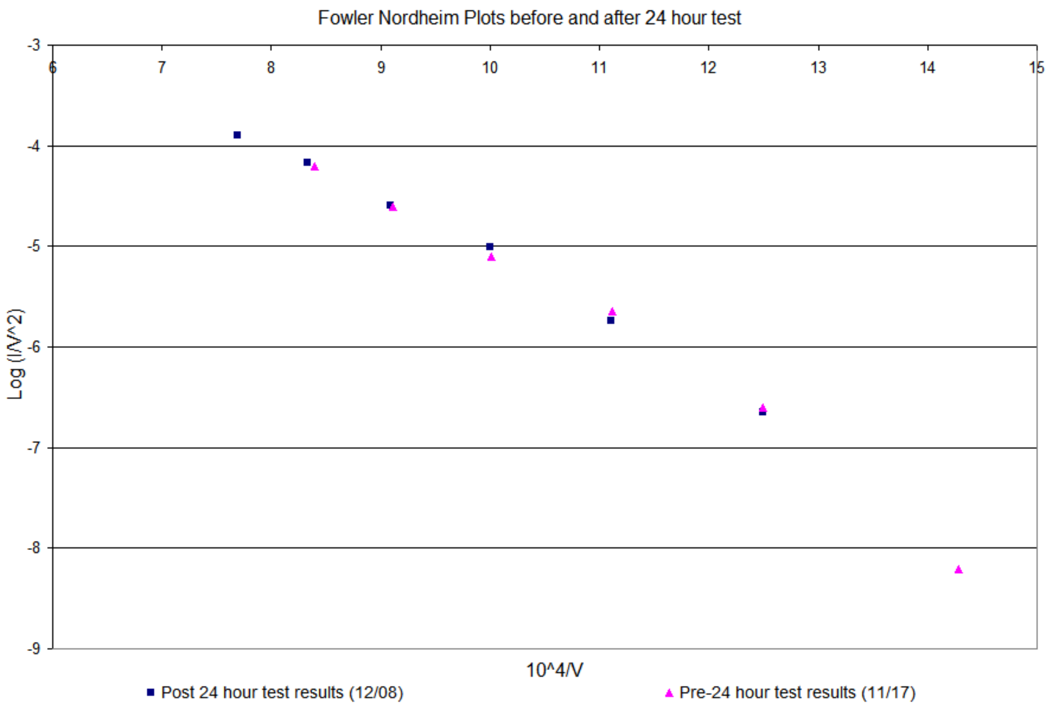

Figure 3-23: Emission results from an array that was examined before and after a 24 hour emission test (Figure 3-22) that saw substantial current loss over time. The results shown here indicate that the array characteristics before and after testing are indistinguishable.

A second 24-hour test was performed on this array with a tungsten anode rather than the phosphor used in previous tests. Plotted on logarithmic axes (Figure 3-18), the linear appearance of the data makes it apparent that emission is decaying exponentially with no signs of a plateau.

Following this second 24-hour test, SEM images of the tips appear to show that many of the tips have been damaged during the test (Figure 3-24). Many tips appear to have suffered from back-bombardment. Newly deposited particles are revealed by EDS to be carbon and copper (Figure 3-25). Oddly, none of the cathode, anode, spacer, or holder apparatus contains copper. Copper is present in the braze material (TiCuAg) binding the diamond film to the molybdenum substrate, but this material has not been observed to be exposed in the field emission area. Further emission testing of this array with a doped silicon anode demonstrated inferior emission currents (<100th) as compared to earlier tests and testing of this array was discontinued.

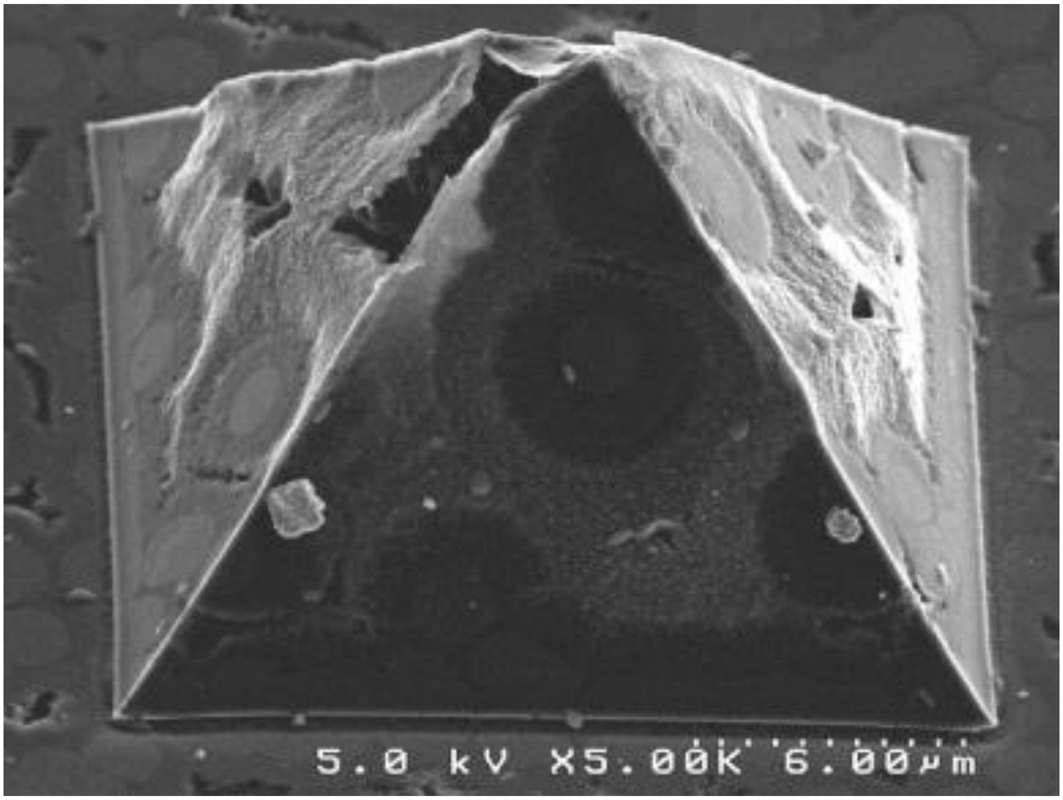

Figure 3-24: SEM image of tip damaged by apparent back bombardment.

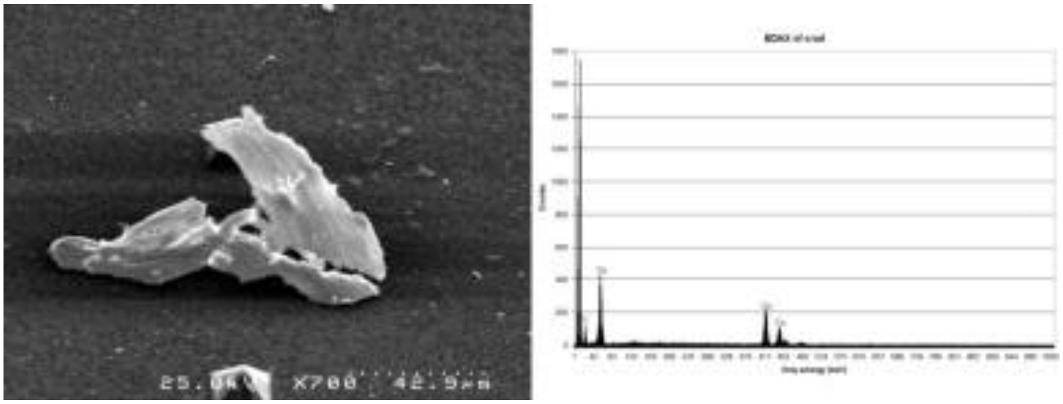

Figure 3-25: SEM image of "crud" found in the array following emission testing. EDS examination of this particle indicates it is copper.

Similar "array recovery" has been seen to a lesser degree in later experiments when an array is left in the chamber at no field for a number of days.

3.4.3. Extended emission tests

Extended emission experiments have been performed up to a maximum of 300 hours. In repeated experiments, arrays show exponential decay in the emission current over time. The decay rate has been observed to vary dramatically based on emission current per tip. In some isolated cases, the array is first observed to increase its emission current over the first few minutes of emission before beginning an exponential decay (Seen in Figure 3-17). This effect is also observed in a 15x15 tip array that was tested for 24 hours (Figure 3-26).

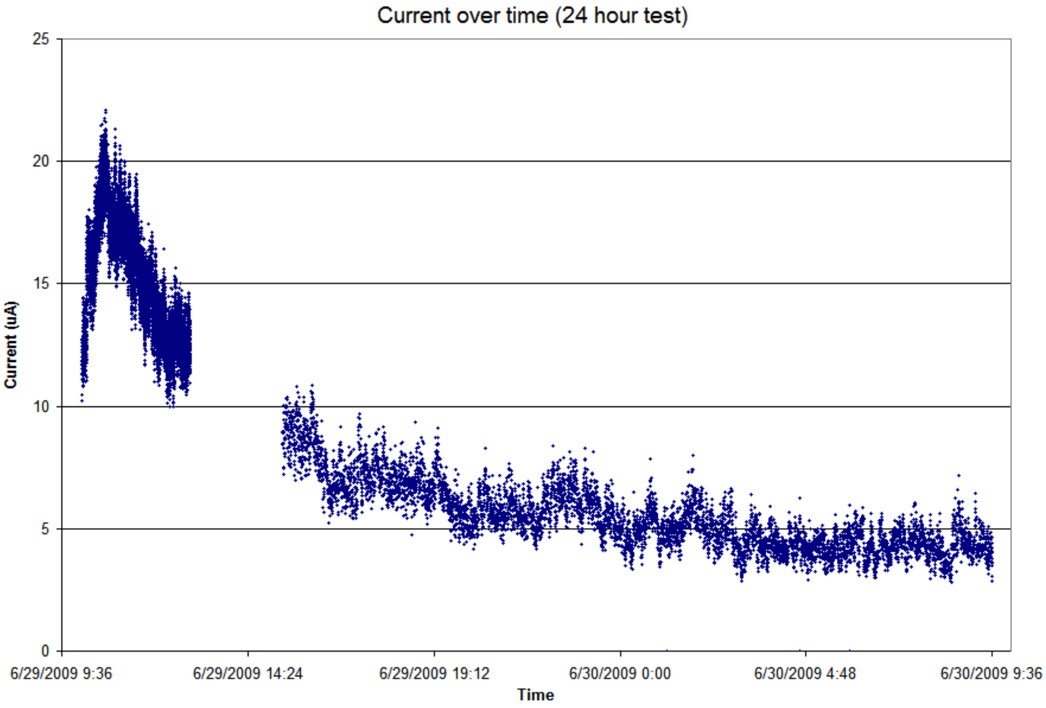

Figure 3-26: Field emission current decay over 24 hours of a 15x15 diamond field emitter array. Gap in data is due to loss of meter data.

When the 15x15 array was run continuously for another 7 days, another anomalous feature appears after 1 day of emission. Figure 3-27 and Figure 3-28 shows this 7 day emission test on linear and logarithmic axes. Figure 3-27 shows the anomaly clearly, while Figure 3-28 demonstrates more clearly that the emission current was not reaching some plateau at a low emission level, but continued its exponential decay for the entirety of the test. Increased noise at low emission levels is to be expected given the low currents measured and the relative magnification of noise due to the logarithmic axis.

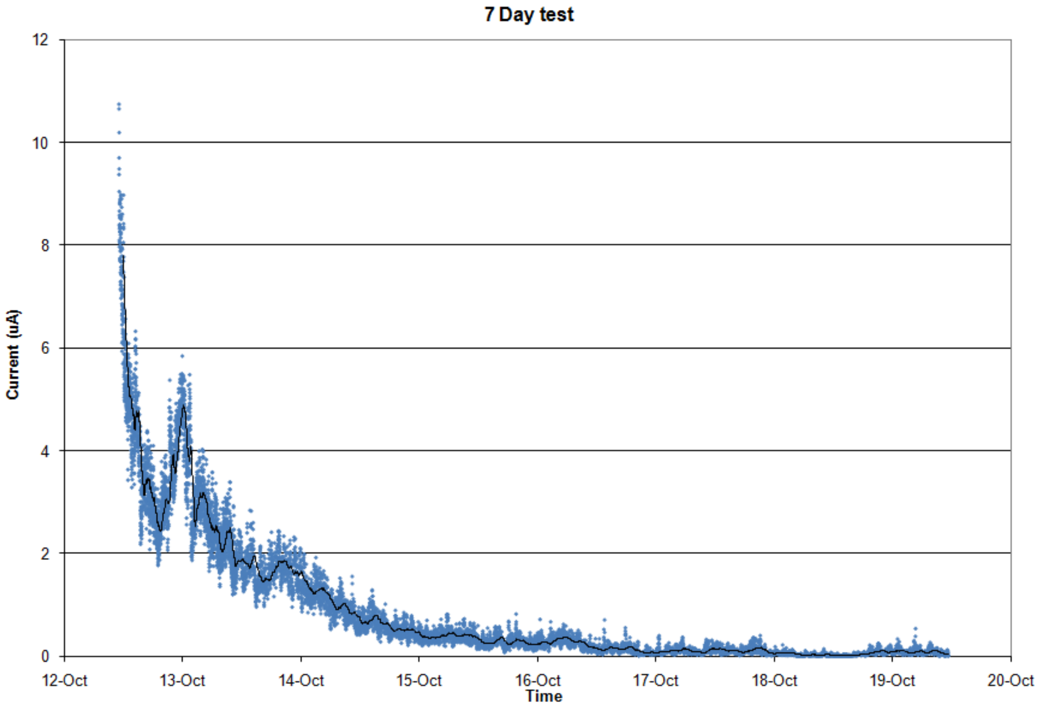

Figure 3-27: Emission decay over a 7-day field emission test plotted on a linear y-axis

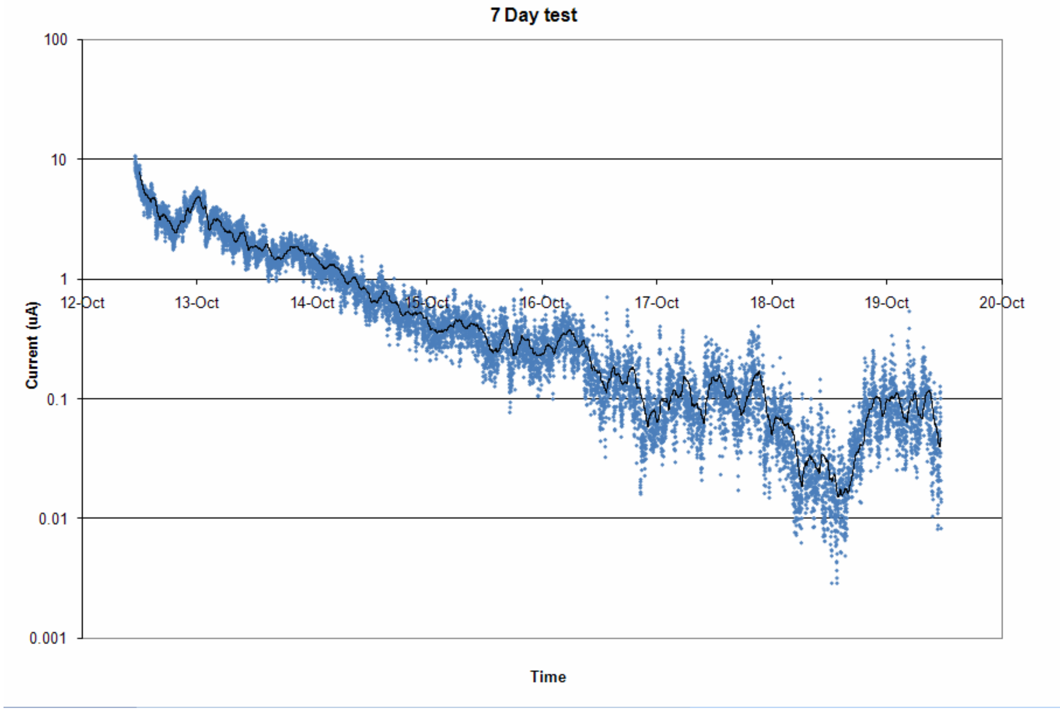

Figure 3-28: Field emission current over a 7 day run plotted on a logarithmic y-axis

SEM images taken before and after three 24 hour tests and a 7 day emission test shown in Figure 3-27 do not indicate any sort of macroscopic change in shape (Figure 3-29). The array appears unaffected by the long emission test despite the obvious drop in emission current.

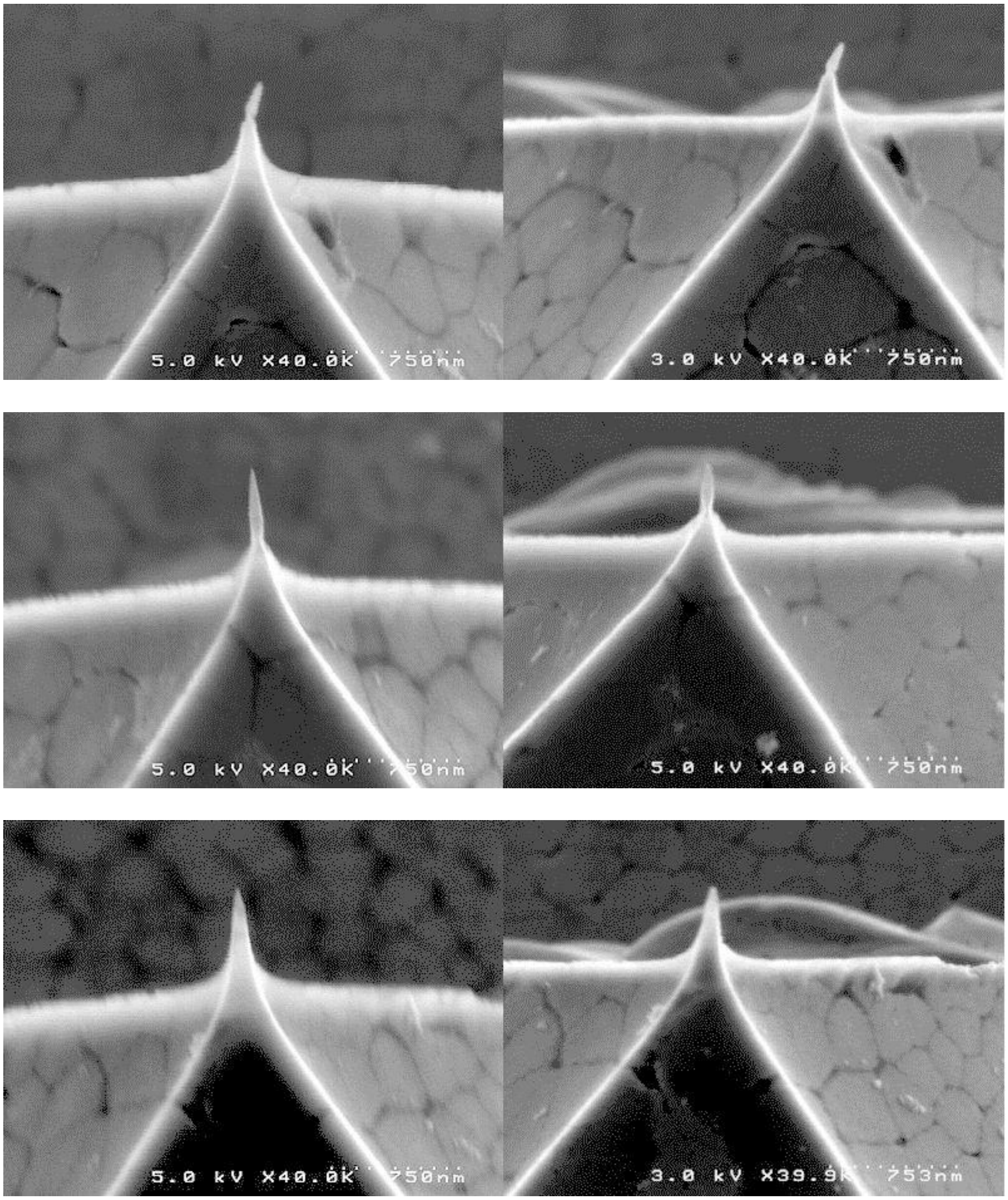

Figure 3-29: Representative tips before (left) and after (right) 10 full days of emission testing. No macroscopic differences are readily apparent. Differences in contrast are attributed to variations in imaging conditions in the SEM on different dates.

3.4.4. *Change in slope with increasing field*

A common feature in field emission measurements is a change in slope of the Fowler-Nordheim (F-N) plot at a moderate field (Figure 3-30). Electron emission onset from diamond arrays is observed from a few individual tips at fields as low as 2 V/µm. Below 5V/µm, the measured emission data does not follow the expected F-N behavior.

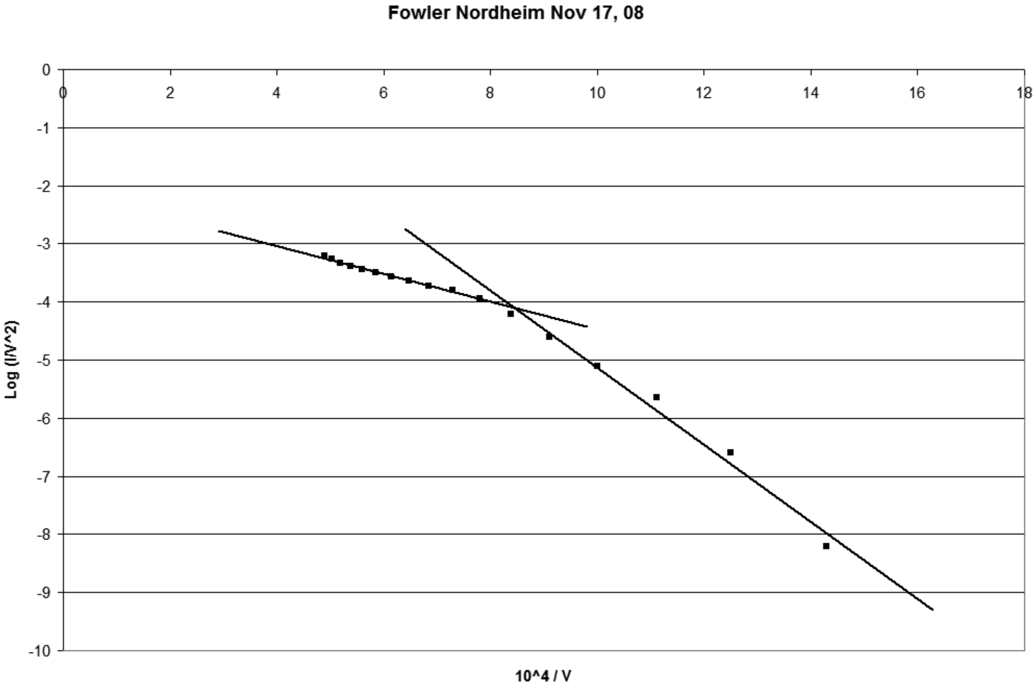

Figure 3-30: Field emission data plotted on F-N axes (explanation in Section 2.3.2). A change in slope is observed at ~5V/um although F-N plots are generally expected be to linear.

While not conclusive, there is a reasonable explanation for this slope change. Variation in field-dependent emission thresholds is considered to arise from variation in the geometric field enhancement factor of individual tips. At low fields the array emission increases faster than at higher fields. Most likely, we are observing field emission from only a portion of the array at low fields from those tips with the highest geometric enhancement factors. As the applied voltage is increased, an increasing number of tips begin to participate, such that we observe the aggregated effects of increasing emission currents from initial emitting tips with emission from new tips. A voltage is eventually reached at which all active tips are participating in emission. Above 5V/µm, we observe only the F-N consistent emission from these tips without the aggregated effect of an increasing number of emission sites. Electron emission increases in a stable exponential fashion, consistent with the Fowler-Nordheim electron tunneling description[46, 122].

It is also considered that as the applied field increases, emission may be seen from an increasingly large area of the tip, as regions with slightly less geometric enhancement reach the required turn-on field. At the point where the increasing applied field does not meaningfully increase the emission area, the aggregated emission behavior becomes more predictable as is expected for well-behaved F-N type emission.

3.4.5. Array outgassing

Residual gas analysis during array turn-on yields interesting results. Emission commencing results increases partial gas pressures of hydrogen and nitrogen which return to background levels over 3-5 minutes of operation. Also monitored were water and oxygen peaks which were observed to be unaffected by diamond field emission. Increasing the applied field and operation at high currents does not have a detectable effect on partial gas pressures. Residual gas analysis is shown in Figure 3-31. Measurements are taken with an ExTorr XT100 residual gas analyzer with quadrupole mass analyzer and 1 – 100 AMU mass range.

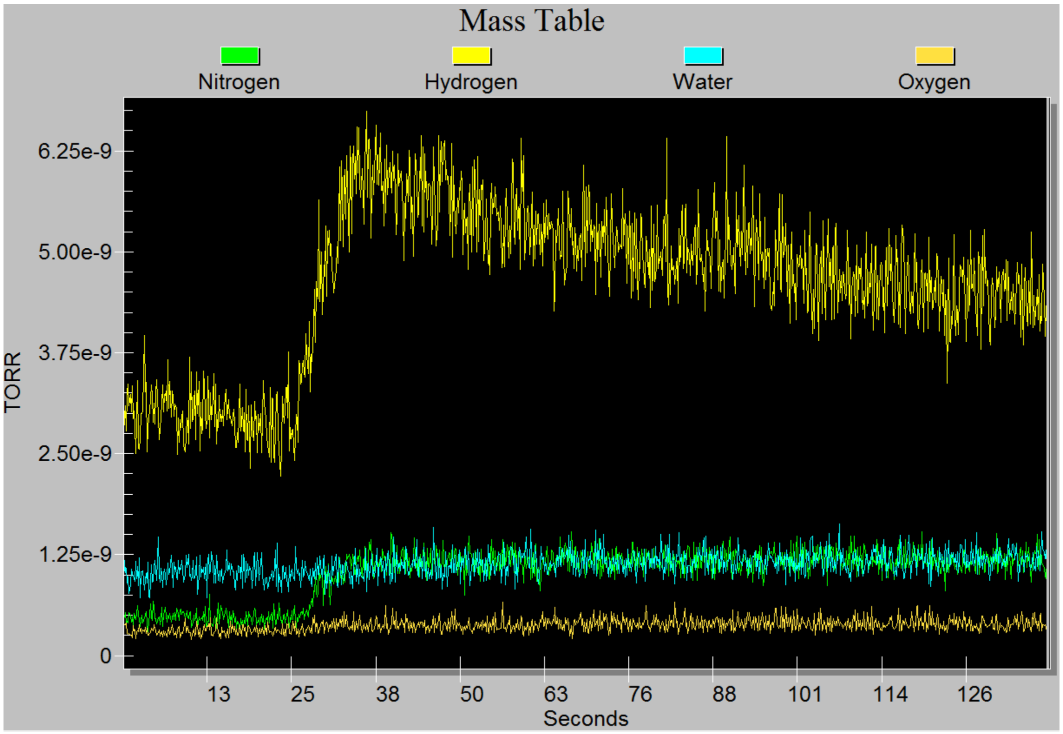

Figure 3-31: Residual gas analysis of field emission chamber during field turn on at 25s. Outgassing of hydrogen and nitrogen observed. No notable outgassing of water or oxygen. Hydrogen levels decay to pre-emission level in 3-5 minutes.

Outgassing of hydrogen was only expected at high temperatures (>700°C), yet its emission is noted at turn-on. High emission currents, which are expected to result in local joule heating and energetic back-bombardment had no measureable effect on hydrogen partial pressures. Nitrogen is similarly not expected to outgas, as nitrogen within the array is thought to be immobilized and nitrogen is not known to adsorb in appreciable quantities on the anode surface. Outgassing of water was expected, as water adsorbs readily onto a wide range of surfaces and is generally easy to desorb.

3.5. FIB METHOD FOR TEM SAMPLE PREPARATION

TEM analysis of unique nanoscale surface features is challenging given the processes typically required to prepare a TEM sample. Gallium bombardment of nanoscale diamond features quickly leads to their destruction and irreversible graphitization of diamond. Initial efforts to extract tips for TEM examination were foiled by Ga sputtering of the surface layers leading to material removal, as in Figure 3-32, and graphitization, as in Figure 3-33. Attempts at removal by non-FIB methods such as laser cutting and mechanical scribing were similarly unsuccessful.

Figure 3-32 and Figure 3-33 were recorded on a 200kV FEI Tecnai G2. Figure 3-32 shows an example where the sharp emitter tip was removed during final FIB thinning. However, Figure 3-33 reveals that with careful sample preparation, it is possible to capture the emitter tip in the cross-sectional sample.

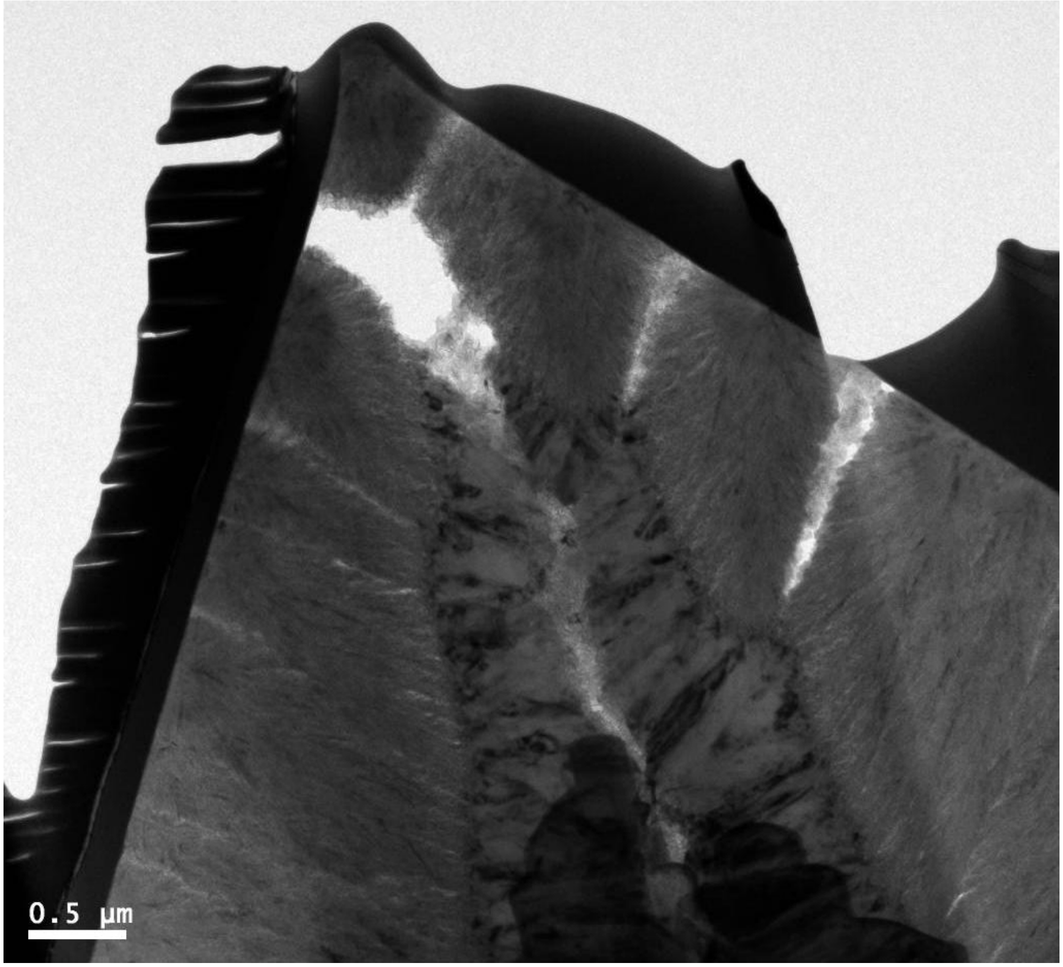

Figure 3-32: Low magnification TEM image of a diamond field emitter tip. The apex of the tip was milled away during FIB thinning, but the underlying structure was preserved well.

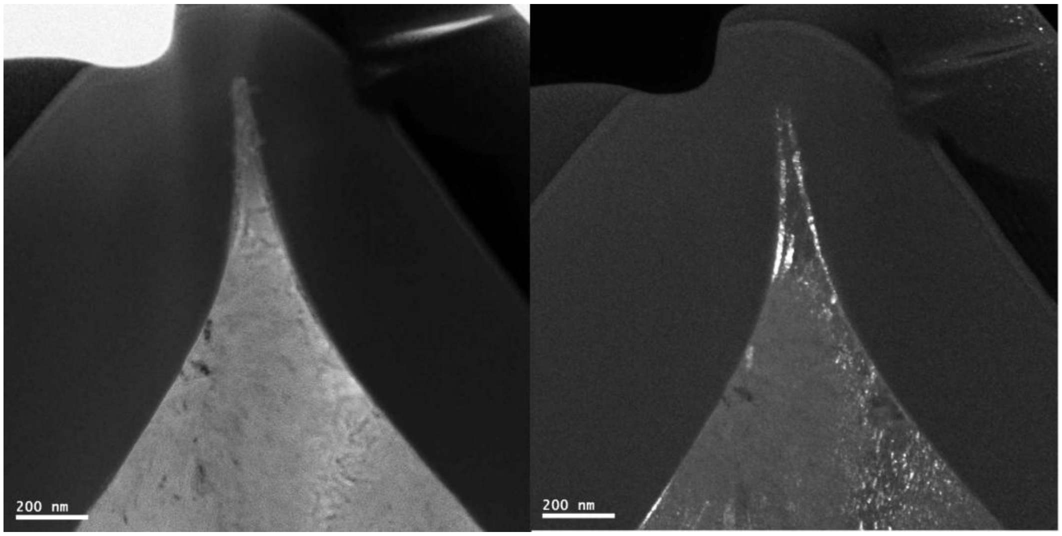

Figure 3-33: TEM image of the first cross-sectioned field emitter tip. Emitter apex is preserved. Right image is the same tip as viewed in the TEM's dark field mode. The bright regions correspond to graphitic surface termination. The nature of the surface is discussed in Sections 3.6.1 and 4.4.3.

Study of these surfaces and structures required the exploration of other methods of TEM lamella preparation to preserve small features and prevent surface graphitization. It is of primary importance to preserve the integrity of the surface.

Cross-sectional TEM samples were prepared on a Hitachi NB5000 dual-beam FIB (electron beam and Ga+ ion beam) at Oak Ridge National Labs, operated by Dorothy Coffey. Dorothy prepared most of the samples used here, and all of the later ones in which quality high resolution images were acquired. Work has also been performed on largely identical FEI Nova Nanolab 200 instruments at the University of Melbourne, The Georgia Institute of Technology, and Oak Ridge National Labs. Figure 3-34 through Figure 3-39 show the sequence of milling steps that result in a TEM lamella as performed on the Hitachi NB5000.

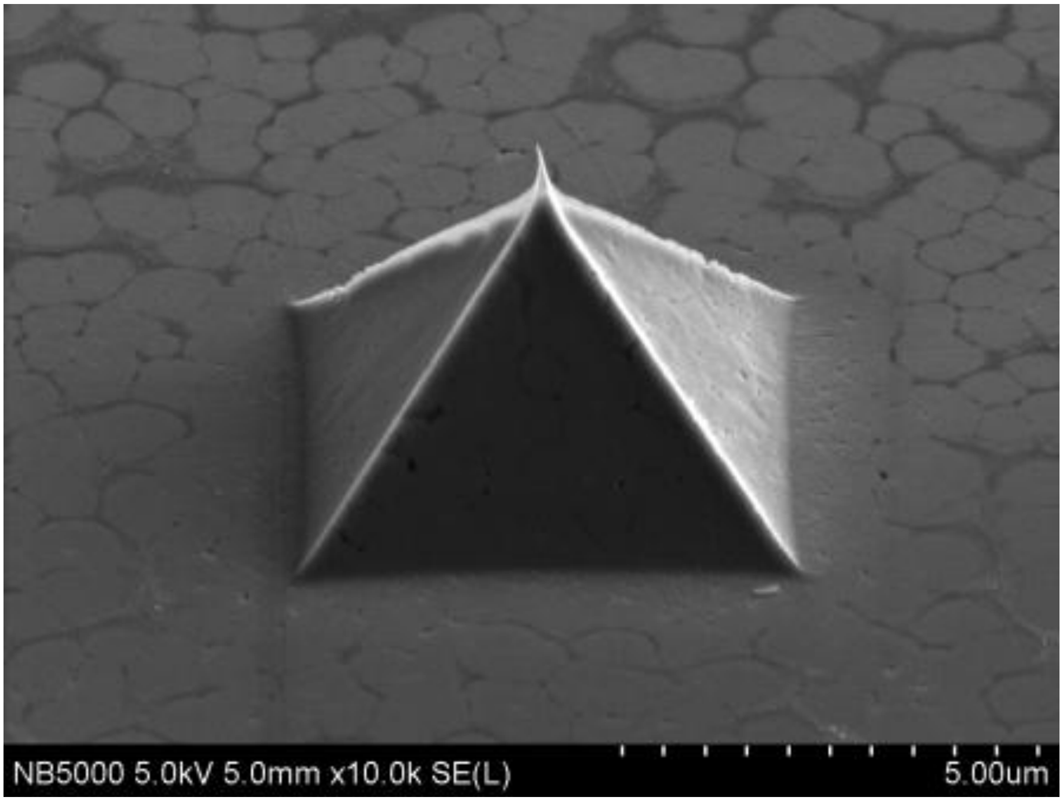

Figure 3-34: Tip 27 from the 100 tip correlation study array prior to FIB extraction for TEM sample preparation.

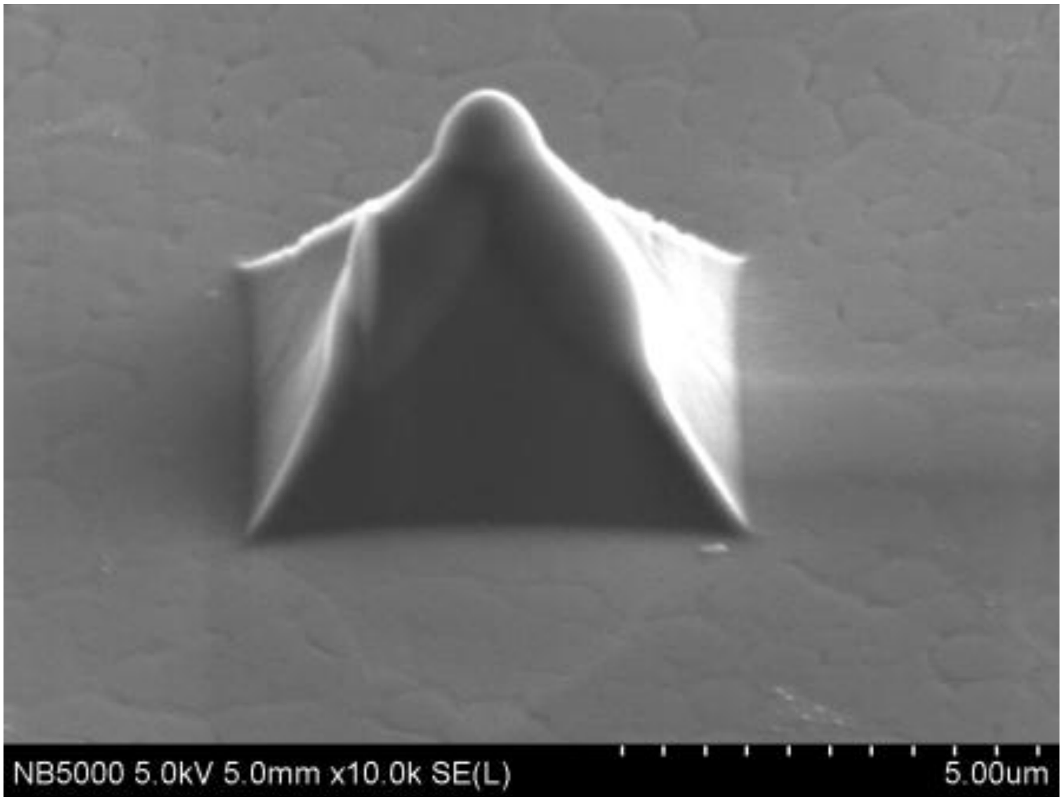

Figure 3-35: Tip 27 from the 100 tip correlation study array following EBID carbon. Deposition of this protective layer insulates the tip from the damaging effects of Ga-beam exposure in later processing steps.

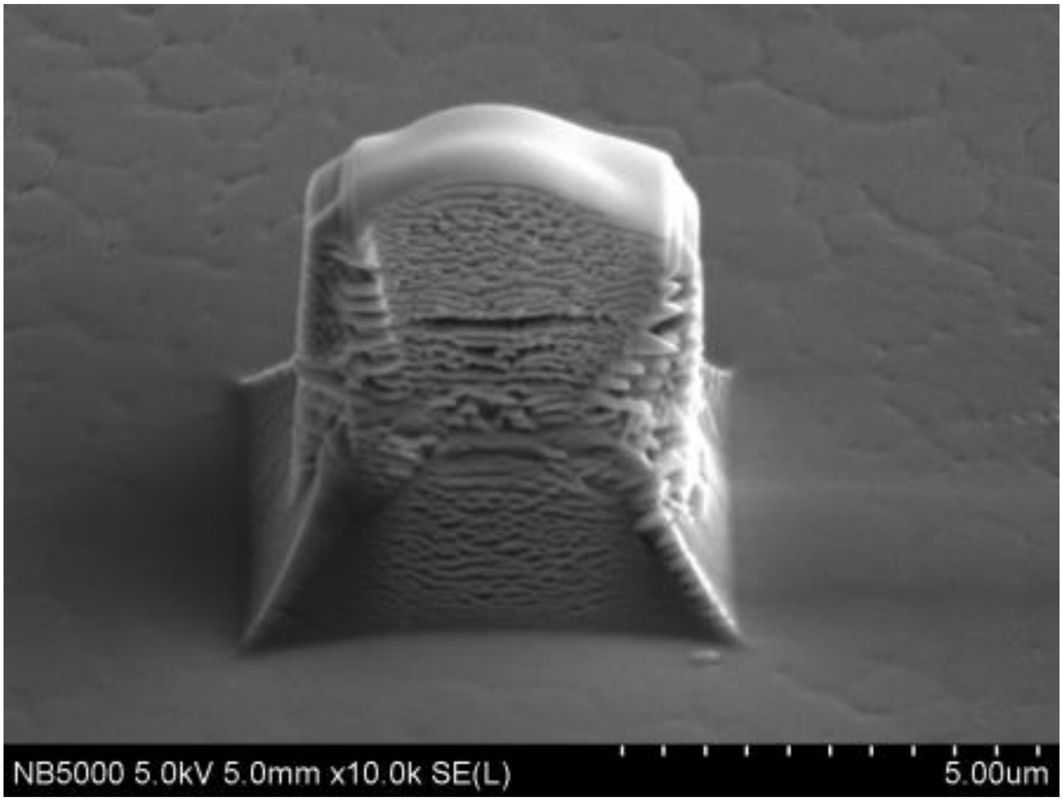

Figure 3-36: Tip 27 from the 100 tip correlation study array following IBID tungsten. The tungsten is deposited by ion beam decomposition of the tungsten halide gas which provides a protective surface layer for later thinning steps.

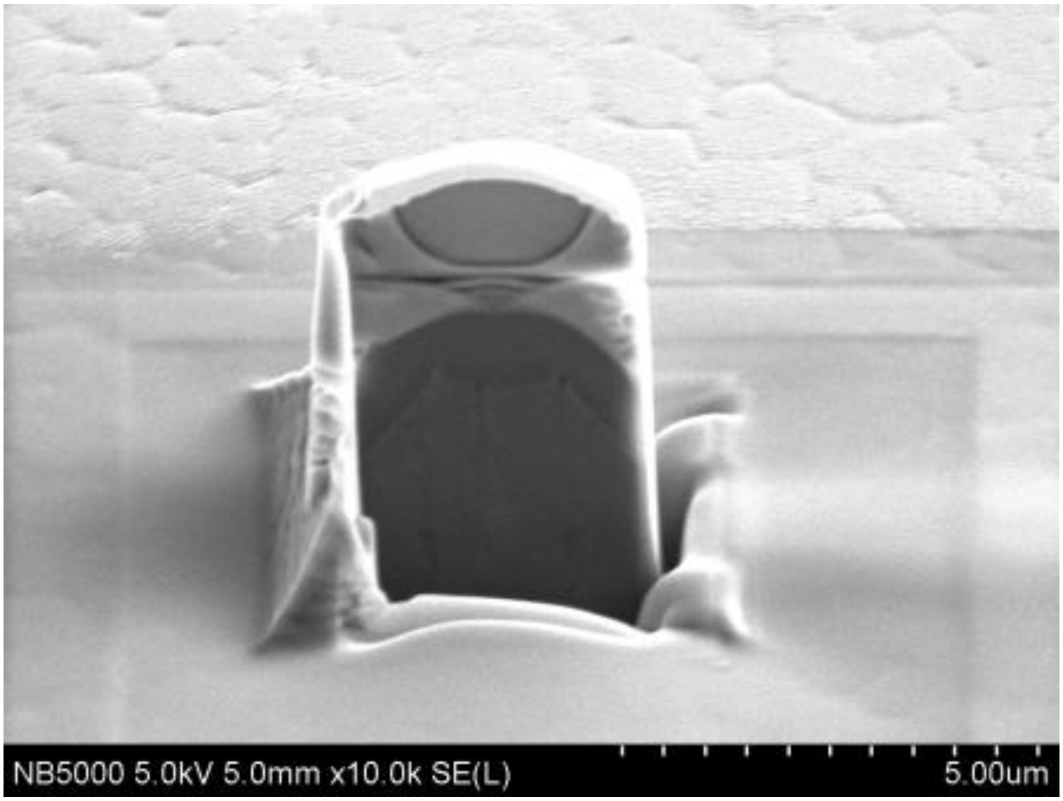

Figure 3-37: Tip 27 from the 100 tip correlation study array midway through removal from the substrate. The bottom and right edges are cut through first, then the FIB probe is attached to the upper right corner of the sample before the left (final) edge is cut.

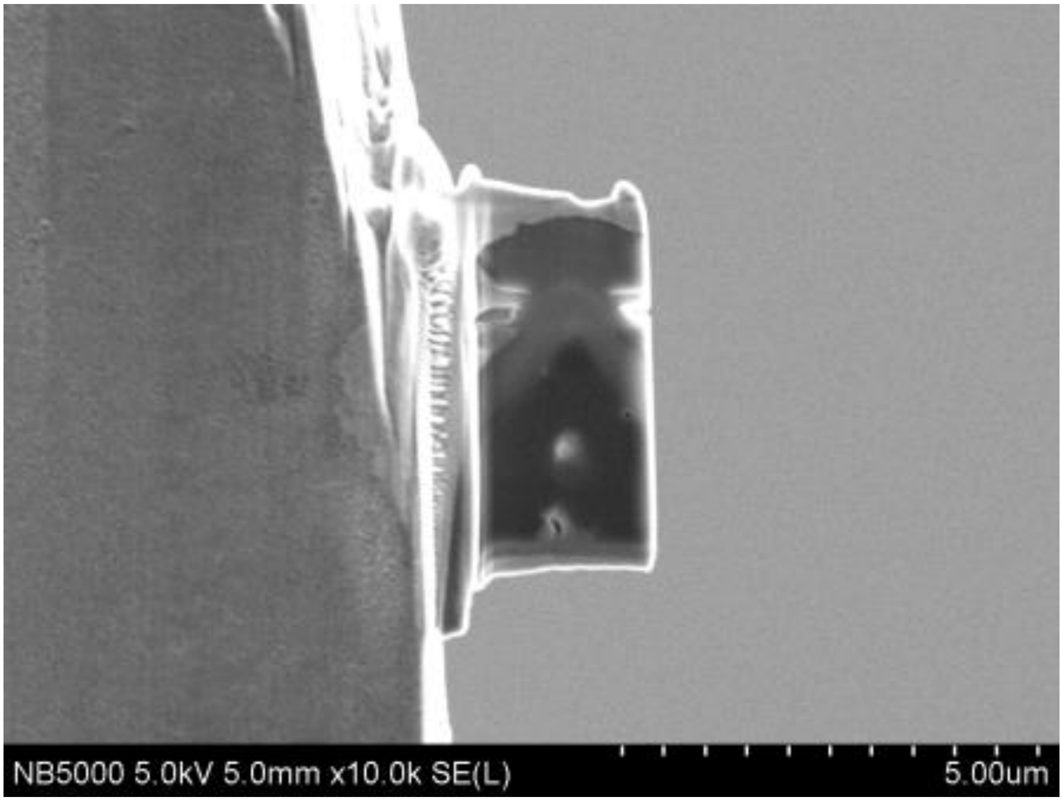

Figure 3-38: Low magnification SEM of the TEM lamella attached to the side of a vertical post on a copper TEM grid. Attachment is achieved by IBID tungsten.

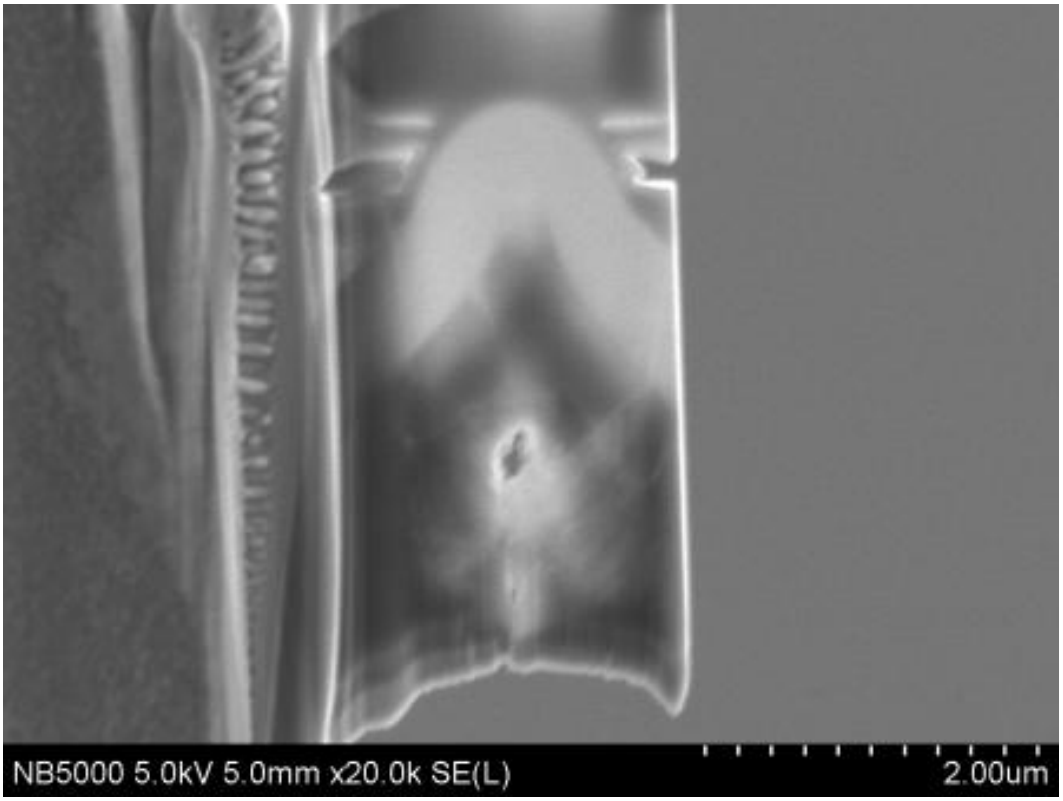

Figure 3-39: Tip 27 from the 100 tip correlation study array following final thinning by FIB. The sample at this point is partially transparent to the SEM electron beam. A void is observed in the center of the pyramid, and it appears that the apex of the pyramid may have been milled away during thinning.

Electron beam induced deposition (EBID) of platinum was necessary to prevent damage induced by the later traditional ion beam induced deposition. EBID platinum and carbon both proved effective preventing gallium sputtering of the diamond surface. EBID parameters used to minimize surface damage were 1kV acceleration voltage at 1nA electron beam current. Deposited thicknesses of 300nm or greater were found to be sufficient. IBID carbon, platinum, and tungsten were all found to be effective protective layers on top of the IBID platinum so long as the thickness exceeded 3µm. See Figure 3-35 as an example of good deposition and Figure 3-32 as an example of insufficient deposition.

FIB milling at 1-3 degrees off normal was found to compensate for a Gaussian ion beam profile producing more perpendicular surfaces and improving uniformity during later steps. Final FIB polishing of lamella surface performed at 0.03 nA of ion beam current at 5KeV resulted in fewer artifacts as compared to final polishing with 0.3 nA ion beam current. To image the actual field emission tip in cross-section, it is critical to thin the FIB lamella equally from each side.

Final cleaning/thinning by argon ion milling (Fischione Instruments Model 1010 Low Angle Ion Milling and Polishing System) helped to achieve thin, artifact free sample surfaces. Ar+ milling at 900V with an incident angle of 10 degrees for 2 minutes followed by 1 minute at 500V gives very satisfactory results.

3.6. TEM OBSERVATIONS

TEM images were taken with a 200kV FEI Tecnai G2, JEOL 2200FS TEM/STEM, and a Philips CM200. High resolution images were collected with the JEOL. Lower magnification images and diffraction patterns were collected with both the FEI and Philips instruments.

3.6.1. Surface graphite on diamond

Figure 3-33 shows a tip viewed under dark-field conditions, wherein bright features indicate graphite aligned parallel to the tip surface. A selected area electron diffraction (SAED) pattern corresponding to this area (Figure 2-18) shows a banded (non-continuous) graphite ring confirming the existence of non-randomly oriented graphite. This graphitic surface termination is an avenue for further exploration of emission non-uniformity, as surface termination is known to be a critical component of field emission[54, 55, 59, 60, 123, 124]. By contrast, Figure 2-19 shows a diffraction pattern from a microdiamond region of the array. The character of the diffraction pattern changes markedly with changes in the grain size of the material. Blurred rings are replaced by bright spots.

High resolution images were collected at with a sub-angstrom probe in a probe-corrected JEOL 2200FS-AC STEM/TEM. Figure 3-40 is a bright field image of a portion of the nanocrystalline diamond layer. It shows a complex microstructure consisting primarily of diamond crystallites. Crystallites on the order of 5 nm in size are evident in this image. Bands of graphite, indicated by a wider lattice spacing (3.55 Å vs. 2.06Å for diamond), are visible. The graphite layers in the image may be specimen preparation artifacts, although the presence of graphitic material in these CVD diamond emitter tips is still an open question.

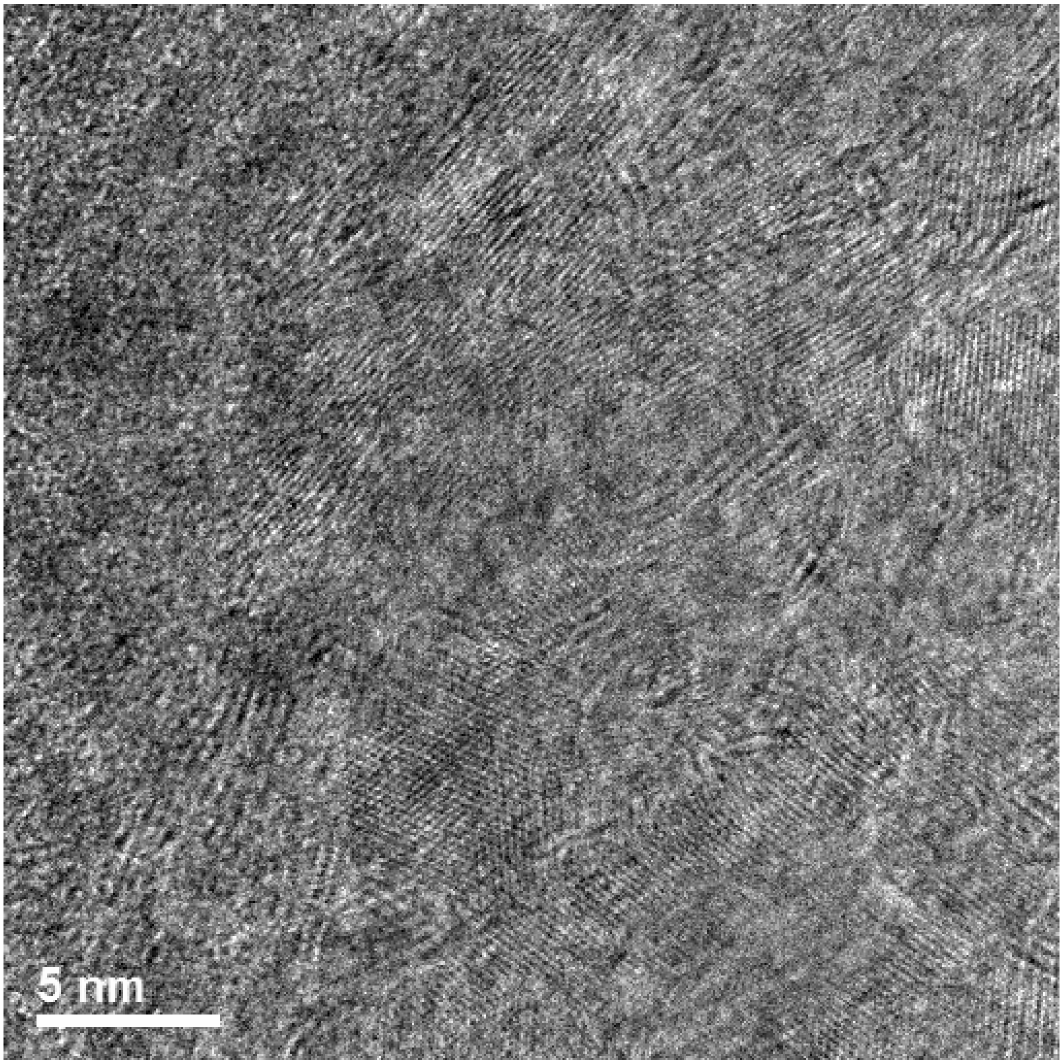

Figure 3-40: TEM image of nanocrystalline layer of the diamond field emitter in which diamond is seen to coexist with graphite. Diamond is characterized by the narrower diffraction lines, while the comparatively wider spacings correspond to graphite. Diamond has lattice fringe distances of 0.201 nm, while graphite shows up as 0.3295 nm.

3.6.2. Surface amorphization

The gallium beam has been shown to amorphize diamond with even minimal exposure. As seen in Figure 3-41, only the briefest exposure in the ion beam imaging mode resulted in 2 nm of amorphized surface material. Later instances of accidental exposure have resulted in 10 nm or more of amorphous material.

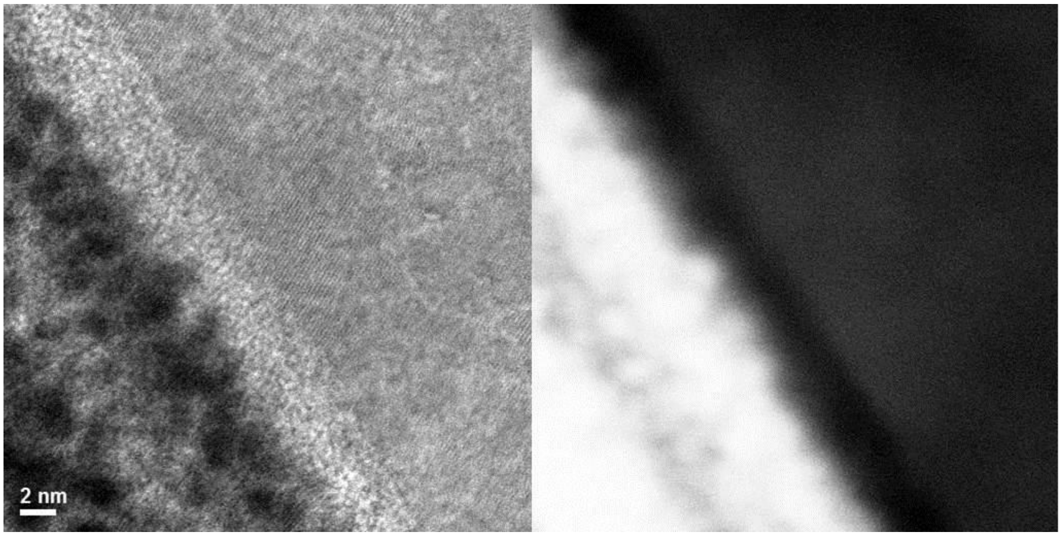

Figure 3-41: Diamond field emitter ultimate surface at high resolution. Bright field image (left) of diamond surface in which the dark region to left is the protective platinum layer and the region to the right is the crystalline diamond layer. Between them is a ~2nm thick region of amorphized carbon. We know this to be carbon due to the matching high angle annular dark field image (right) which is sensitive to atomic weight but insensitive to structure. The amorphized region is dark, indicating that it is made up of the same element as the diamond region.

3.6.3. Voids

In most instances of extracted tips, apparent voids have been exposed where diamond growth structure occluded further growth in that area (Figure 3-39). Voids near the surface have also been observed (Figure 3-32). Given that the various protective capping layers deposited in preparation for extraction cover these voids seamlessly and the fact that they are not visible in pre-extraction images, the voids may be an artifact of TEM sample preparation. The protective layer in Figure 3-32 is platinum. Equivalent results with respect to surface voids have also been seen in EBID amorphous carbon layers as in Figure 3-42.

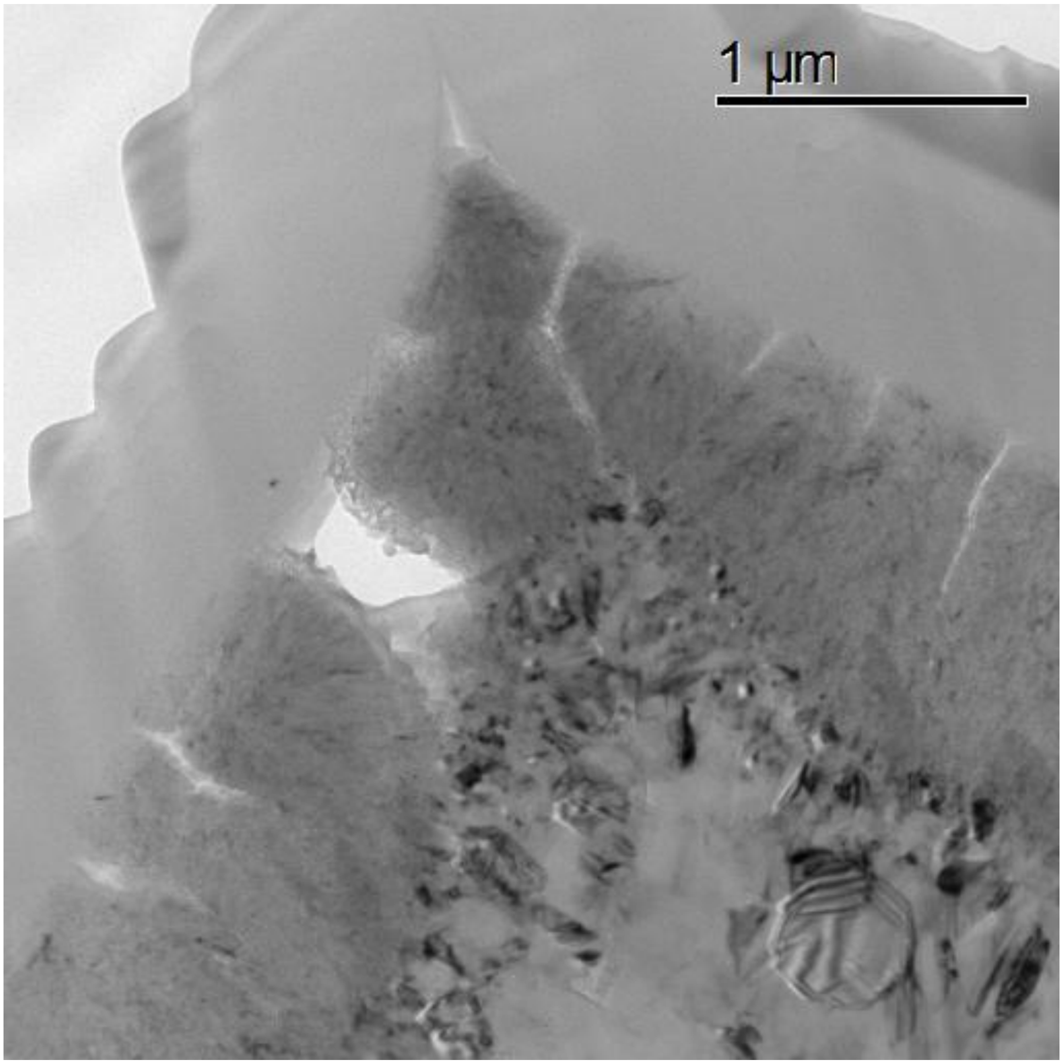

Figure 3-42: TEM image at low magnification of a diamond field emission tip in which a substantial void is observed at the surface. This void has been seamlessly covered by the amorphous EBID layer of carbon.

Initial void observations led to a discussion of the makeup of the material previously located in the void region. The protective deposition of amorphous carbon has behaved in the same way as other overcoat materials implying that the void region of the tip was not previously filled with amorphous carbon. If it had been, the void should not have been etched preferentially as compared to the protective layer. Graphitic content or a contaminant material such as silicon cannot be ruled out.

We have observed that a tip can grow around an impurity particle during growth, as in Figure 3-43. In the instance where an impurity particle is present during or prior to growth, the diamond deposition procedure is robust and is deposited notwithstanding.

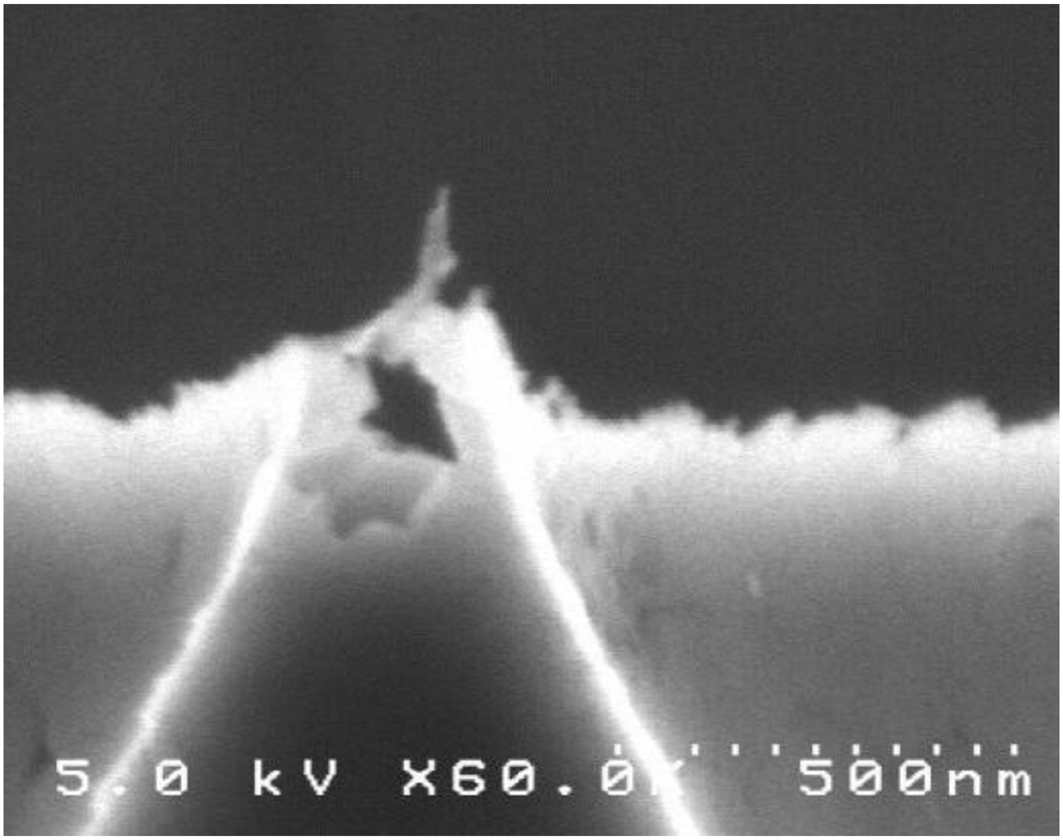

Figure 3-43: Field emission tip in which a contaminant particle (likely silicon) at the tip of the mold was incorporated into the diamond growth process and later etched away after growth. The diamond growth continued around the contaminant irrespective of the particle.

In all cases, but particularly in Figure 3-32 and Figure 3-42, we observe areas of sparse growth between nucleation points, as those regions were starved of chemical reactants during the initial nucleation and growth stage of the diamond deposition. These features are consistent with our current understanding of chemical vapor deposition. A low density of nucleation sites tends to result in wide grain boundaries with substantial non-diamond content. Uniformity in this layer may be improved in the future by increasing the nucleation density.

A detailed analysis of CVD diamond content vs. nucleation density was performed by Butler and Sumant [125]. They compared the “quality” of diamond films with various methods of pre-nucleation treatment. In this case, “quality” refers to how closely the CVD diamond film approaches the thermal, mechanical, and optical properties of bulk single crystal diamond.

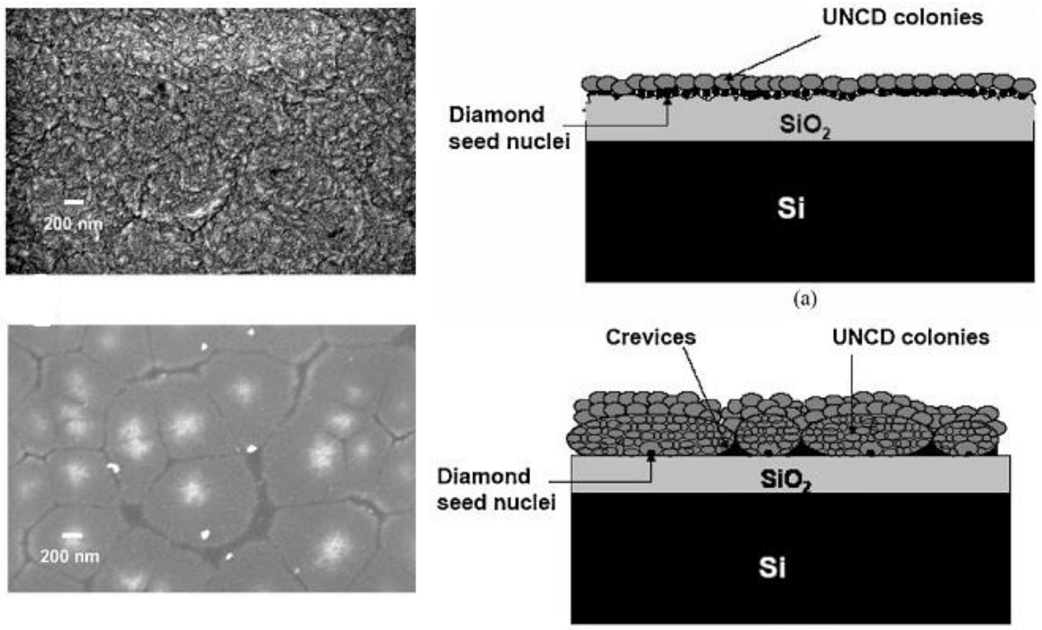

Figure 3-44: Nucleation surface of diamond films grown by the same method but with different nucleation steps. Top left image has a high diamond content, while the lower left image is shown to possess substantially more non-diamond content by near-edge X-ray absorption fine-structure spectroscopy (NEXAFS) and Raman. Image by Butler and Sumant [125, 126]

In recent work by Paul May’s laboratory, they have pioneered a nucleation method to great success [127], which we may consider utilizing in future CVD diamond growth. Their process involves a detonation nanodiamond suspension which is sprayed in a controlled manner onto an electrified, rotating platter. The platter is held at 35 kV to enhance nanoparticle adhesion. A schematic and picture of the apparatus is shown in Figure 3-45. Improved growth around complex features is observed as in Figure 3-46.

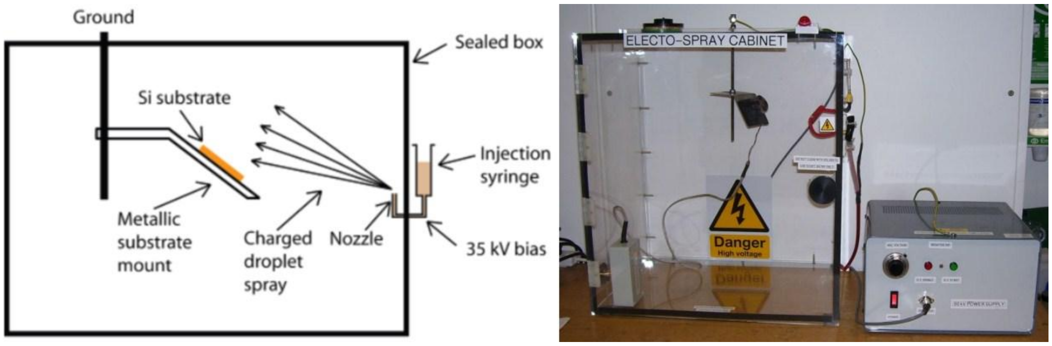

Figure 3-45: Electrospray nanodiamond nucleation setup by Fox et al for seeding CVD diamond growth.

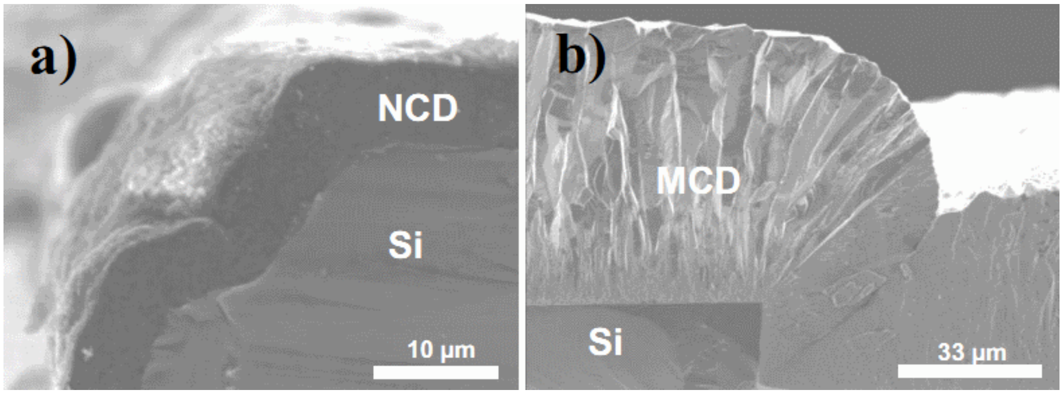

Figure 3-46: Conformal diamond growth as demonstrated by Fox et al [127] with use of new diamond nucleation method. Image b) shows a particularly difficult CVD diamond fill with no voids formed at the step.

3.6.4. Crystal growth observations

A low magnification TEM image of the cross-sectioned pyramidal tip in Figure 3-47 illustrates the two-step fabrication process in which 1-2 µm of nanodiamond is grown to form the emitter tip surface followed by microdiamond that produces the bulk of the tip. In Figure 3-47, nucleation points are visible at the emitter surface as origins of dendritic growth consistent with chemical vapor deposition (see the two arrows) [95, 125]. In these images, we observe areas of sparse growth between nucleation points, as those regions were starved of chemical reactants during the initial nucleation and growth stage of the diamond deposition.

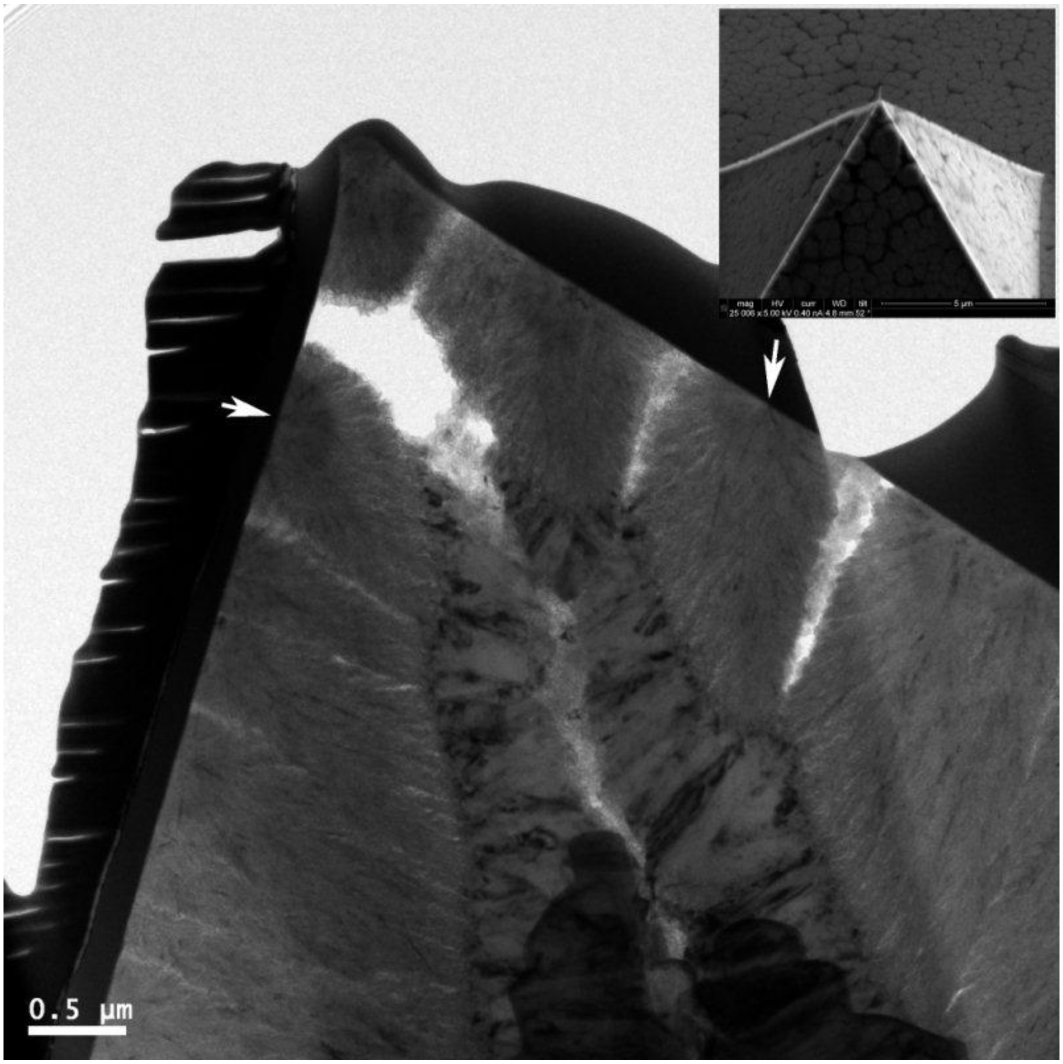

Figure 3-47: TEM image taken at low magnification to emphasize structural growth features. Arrows highlight nucleation points on the emitter surface.

Regions of sparse growth between nanocrystalline diamond colonies have a much higher concentration of non-diamond content due to sheltering of these regions from the plasma chemistry by the nearby grain growth. Large grain boundaries such as these have been directly correlated with high non-diamond content by Butler et al [125].

Nanodiamond crystals are visible in the 1 µm nanodiamond layer at the emitter surface. In Figure 3-48, the crystals have been circled to assist with identification of grain boundary edges. Diffraction patterns taken of nanodiamond regions confirm the presence of many stochastically oriented diamond grains (Figure 3-49).

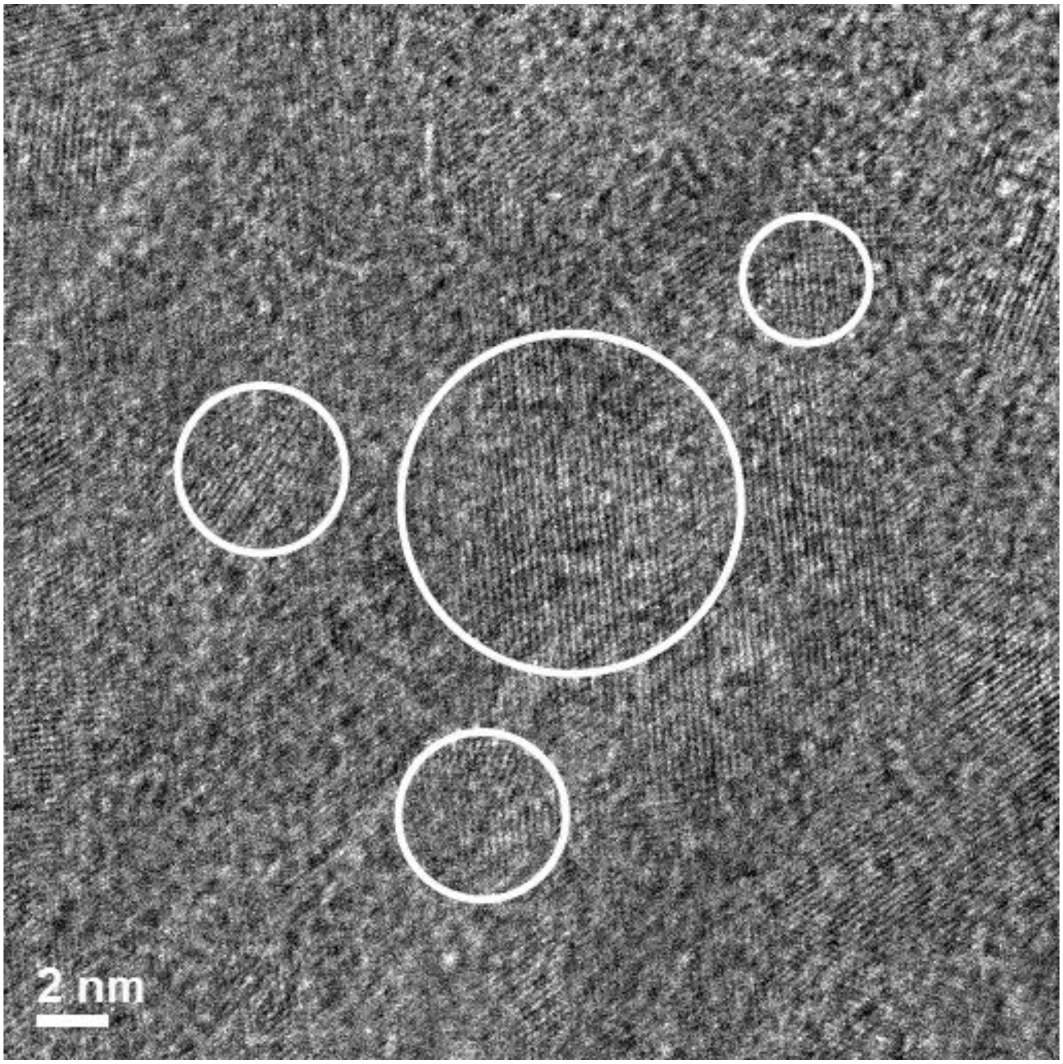

Figure 3-48: TEM image of nanodiamond crystals in the surface layer with outlines.

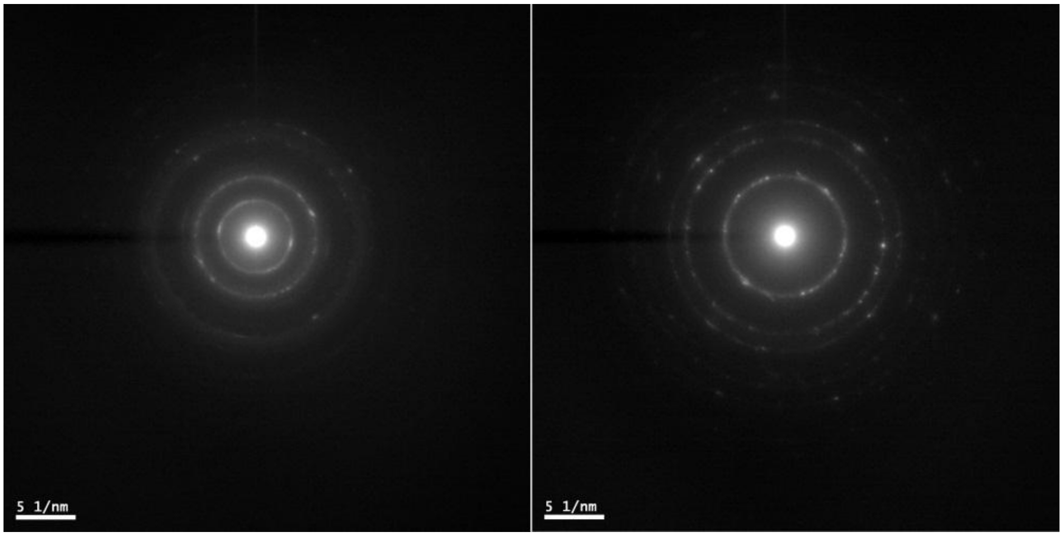

Figure 3-49: Selected area electron diffraction (SAED) patterns of two nanodiamond regions. Left image has an extra inner as compared to the right image. This ring is associated with graphite. In all rings, we see a smooth, blurred ring with occasional bright spots. The rings indicate small (<100 nm) stochastically oriented grains, and the bright spots indicate single domains larger than its neighbors.

In instances where a low nucleation density of the nanodiamond layer led to incomplete surface coverage, the microdiamond layer has sometimes been observed to form an excursion to fill in the gap as in Figure 3-50. In instances where the nanodiamond nucleations grew together late in the process, a void is preserved as described in section 3.6.3.

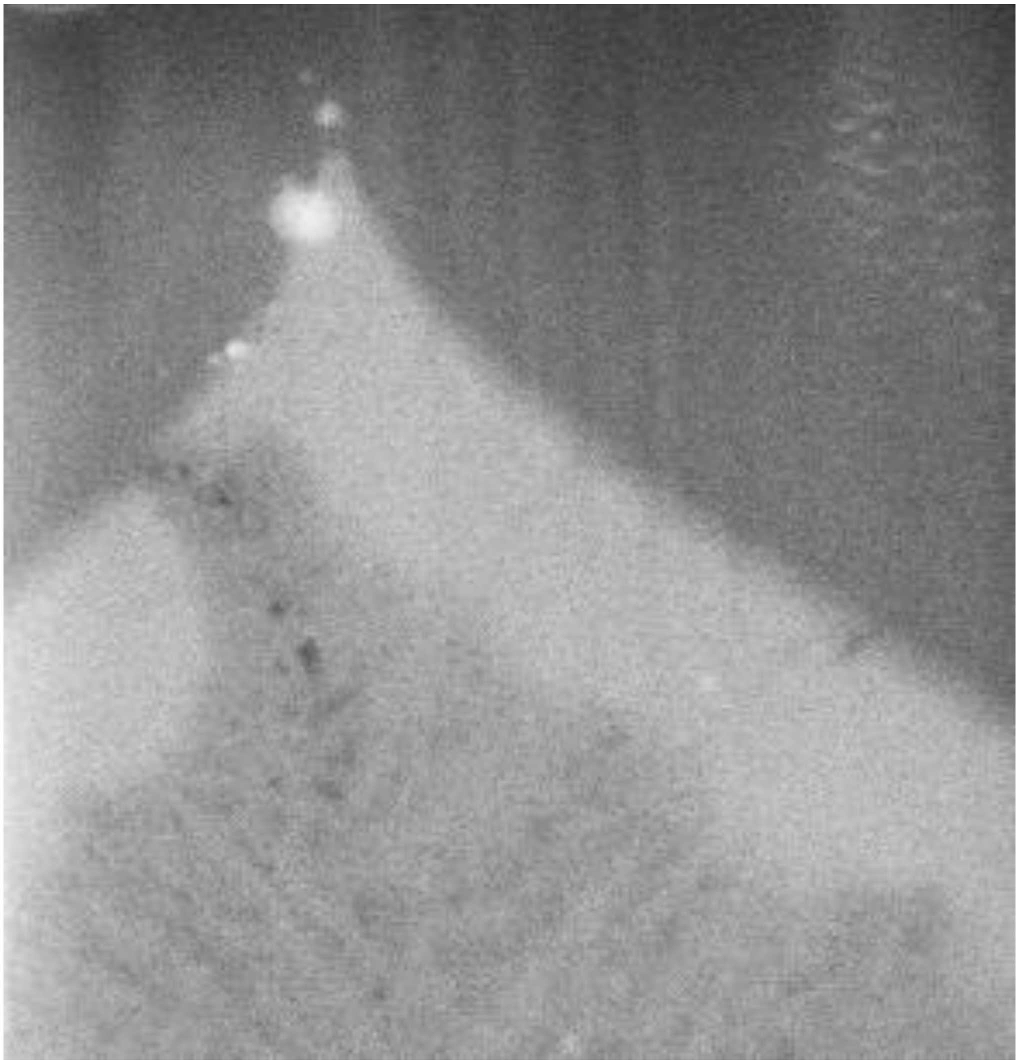

Figure 3-50: TEM image of a diamond field emitter tip in which incomplete nanodiamond coverage allowed the later microdiamond growth step to form an excursion to the surface of the emitter. Bright spots near the tip are contamination spots from earlier TEM examination, and are not real emitter features.

CHAPTER 4

DISCUSSION OF RESULTS

4.1. DEVELOPING A FEEDBACK METHOD FOR CVD DIAMOND GROWTH

Analysis of field emitter structures has the immediate benefit of offering feedback to the fabrication process which has not existed before. Prior to this work, poorly emitting tips lacked explanation unless it was due to dramatic geometric irregularity. Here, we have observed that some of the brightest tips are not the sharpest ones, that low nucleation densities are not a major detractor to emission, and that even tips which are primarily not diamond in content are capable of emitting adequately. More important are the methods developed for analysis of three dimensional diamond structures to enable systematic optimization of emitter structure for current and future fabricators. Also included are some preliminary observations correlating emitter structure to behavior. Correlating structures to emission is expected to be an ongoing process as each evolution of technological development introduces new growth chemistries, geometries, and emitter configurations. As emitter requirements transform over time, the important attributes to be optimized will also likely change, making the methods for inspection of these structures more important than ever.

4.2. TIP CONDUCTIVITY UNDER SEM

In a qualitative assessment, it appears that tips which do not behave as expected often share a common feature under SEM. Since SEM imaging is based on backscattered electron detection, it reflects structural features as well as some indication of the ability of the material to channel away electrons. From this, we can obtain information regarding electrical conductivity of the tip. The tip shown in Figure 4-1 is sharp and appears dark under SEM. Tips that appear dark in contrast to the emitter base are observed to be good emitters. Bright features indicate charging under the SEM beam; it was unable to channel away incident electrons. By comparison, the tip in Figure 4-2 has multiple domains of varying conductivity.

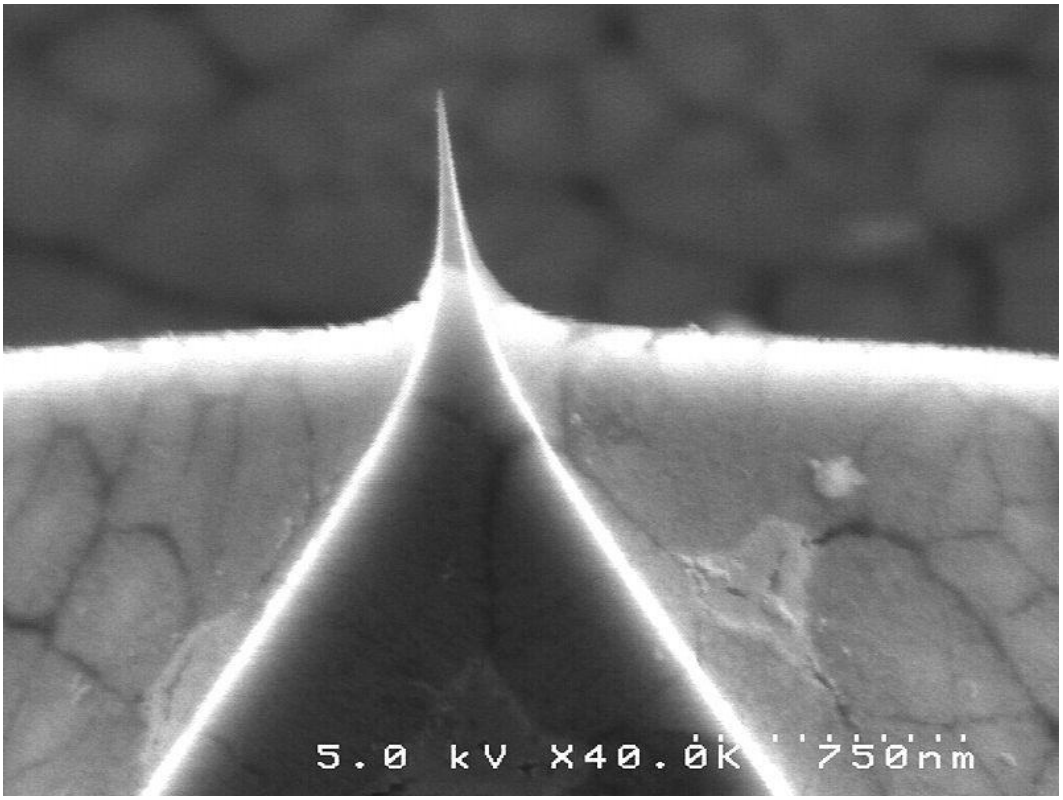

Figure 4-1: SEM image of a sharp, electrically conductive (dark contrast) tip.

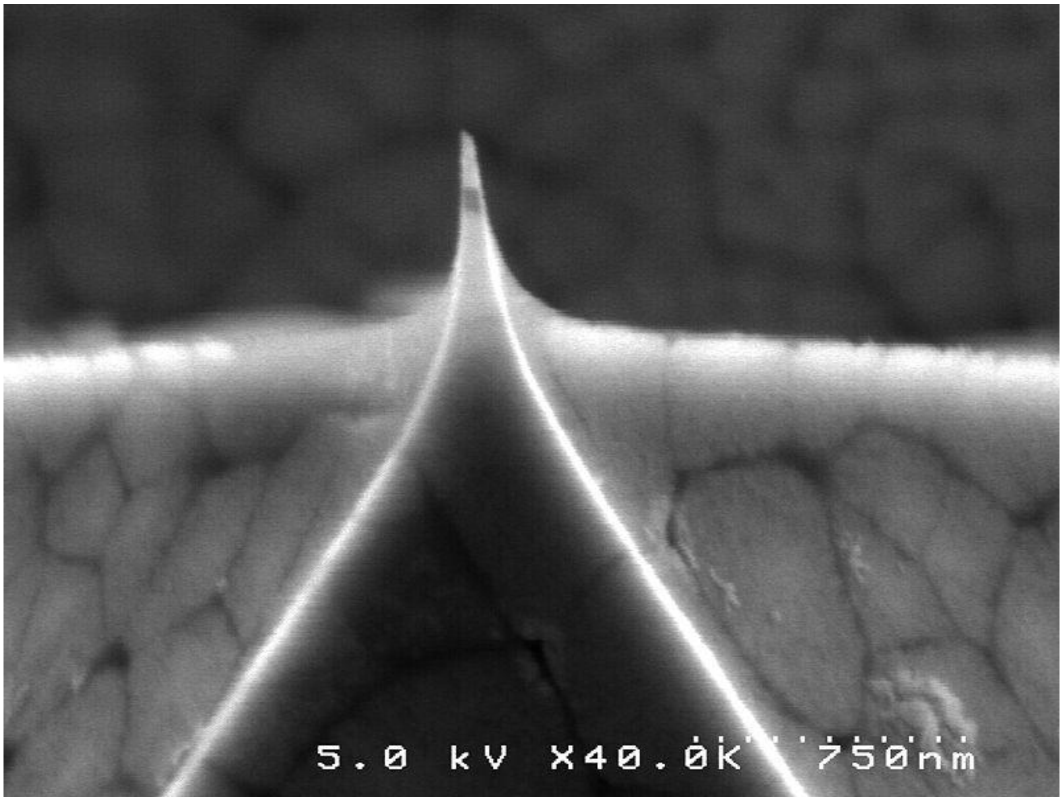

Figure 4-2: SEM image of tip with different multiple contrast features

Another interesting comparison can be made between a pair of tips from the same array. In both Figure 4-3 and Figure 4-4, tips have approximately the same tip size and shape, but the tip in Figure 4-3 is notably darker (indicative of higher electrical conductivity) than Figure 4-4’s speckled structure. Indeed, the tip in Figure 4-3 emitted well while the tip in Figure 4-4 did not.

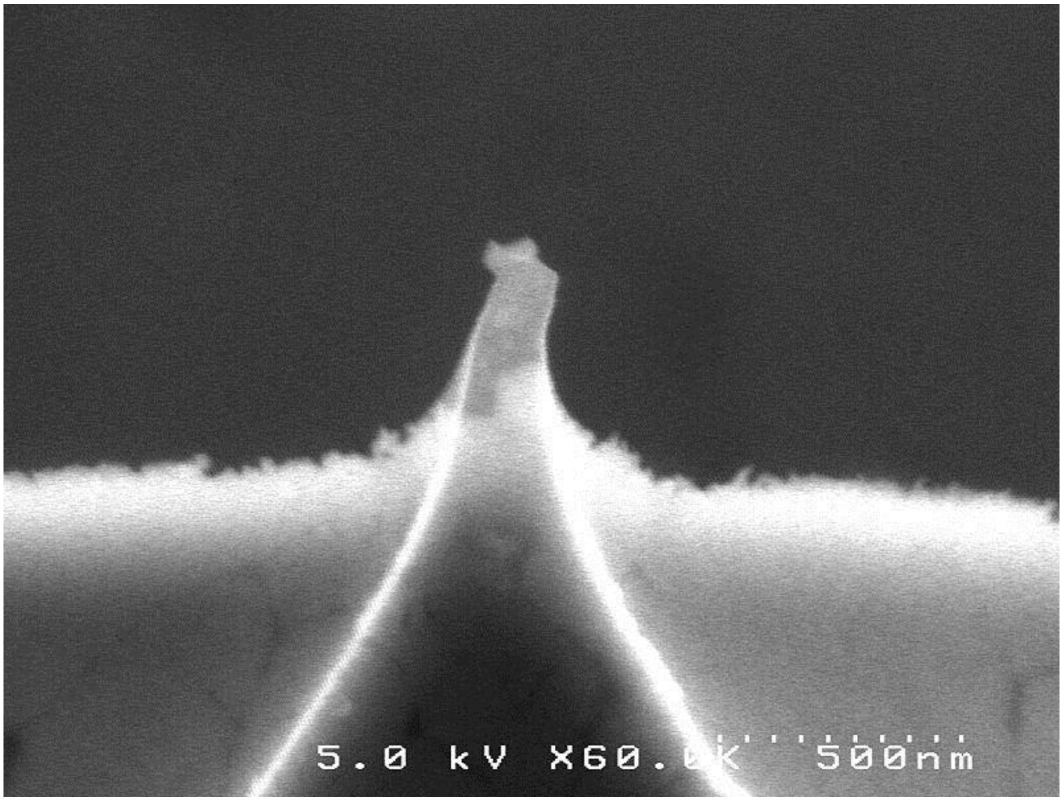

Figure 4-3: SEM of diamond field emission tip 5 from the array in Figure 3-14 with dull, but dark tip features. This tip emitted well.

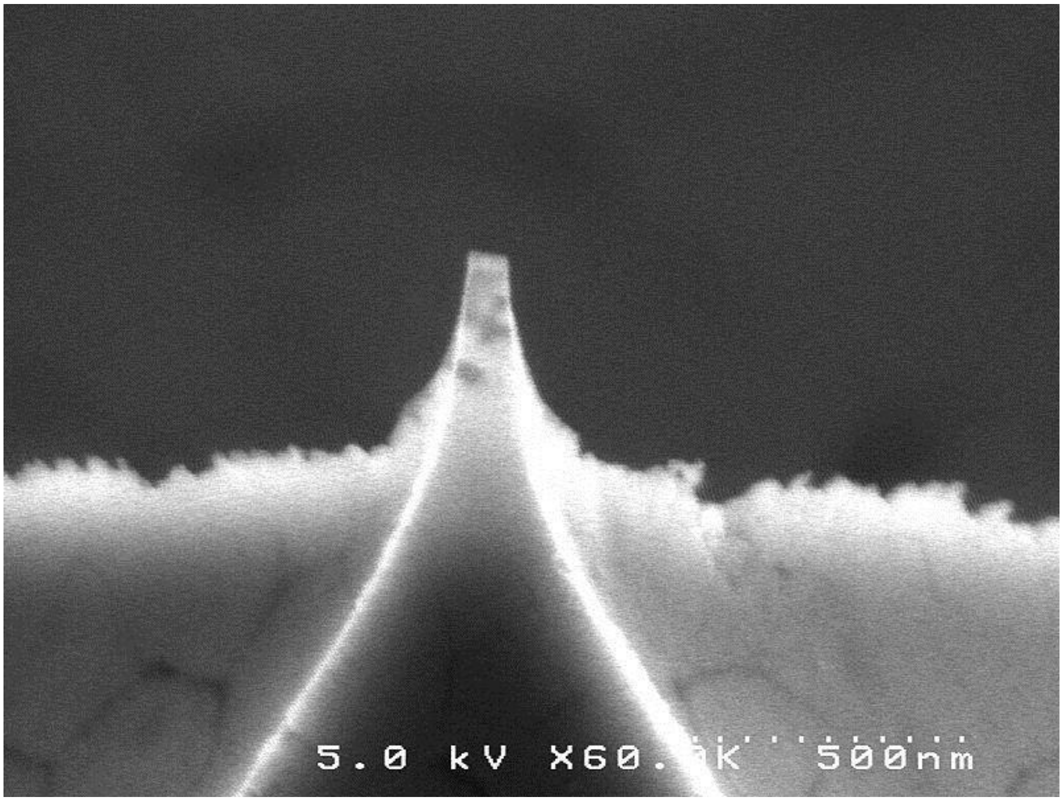

Figure 4-4: SEM of diamond field emission tip 20 from the same array as Figure 4-3. This tip has similar dull features, but the tip contrast is speckled indicating regions of varying conductivity. This tip did not emit.

Due to an insufficient number of samples, TEM measurements were unable to verify this structure-emission relationship pending the completion of a correlational study.

4.3. SURFACE STATES / ADSORBATES

On a clean diamond surface, the reconstructed π bonds form a largely non-reactive and bio-compatible surface. For this reason, adsorbed chemical bonding states that are strong enough to disrupt the reconstructed surface tend to be stable as well. Diederich et al. [61] have observed strong surface dipole effects linked to hydrogen surface adsorption (Figure 4-5). Ultraviolet photoelectron spectroscopy with a helium discharge lamp (21.2 eV) was used to observe the emission spectra of boron-doped type IIa natural diamond crystals. Negative electron affinity (discussed in more detail in Section 2.4.3) was observed with hydrogen termination on (100), (110), and (111) crystal faces, as well as OH termination on (100) faces. Measurement of each face saw an electron affinity of approximately -1.0eV ±0.1.

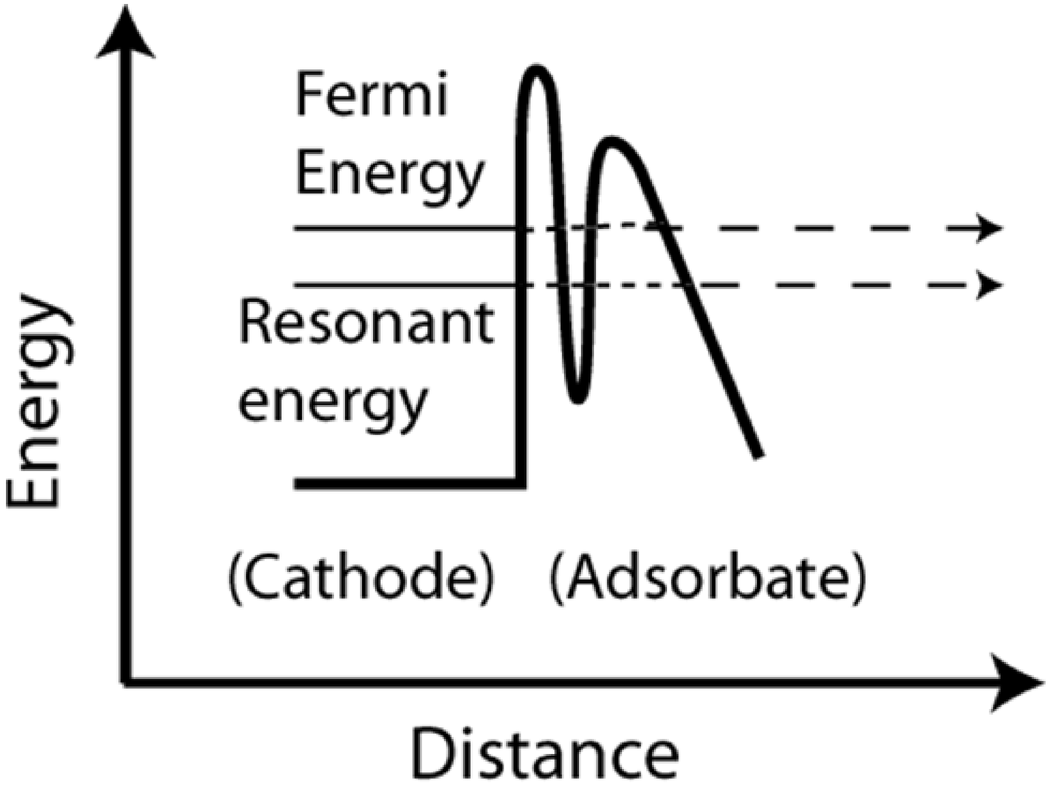

Figure 4-5: Energy diagram illustrating the effect of surface adsorbates on the surface barrier

In the field emission experiments performed in this work, nearly all tips have been observed to “flicker” at a low, random frequency similar to the series of images in Figure 4-6.

Jarvis et al. at Vanderbilt have measured dramatic emission current increases associated with adsorbate motion shown in Figure 4-6 [110]. Through substrate temperature manipulation and energy analysis of the electron beam, Dr. Jarvis was able to determine that the clean surface was the lesser emitting and that the temporary presence of an adsorbate dramatically increased emission. For brief periods, current densities approaching quantum-mechanical limits have been observed [110]. Careful control of adsorbate motion has the potential to dramatically enhance the field emission properties of any field emitter. The unstable nature that gives such dramatic enhancement may prove difficult to regulate.

These observations from carbon nanotubes are consistent with much older results (Figure 4-7) published by Spindt et al [48] on molybdenum cathodes which were unexplained at the time. We now understand that these short term spikes in field emission current are due to the transient behavior of adsorbate molecules which temporarily create an unstable surface dipole. The time scale of these adsorbate “events” tends to 0.1 – 100 seconds.

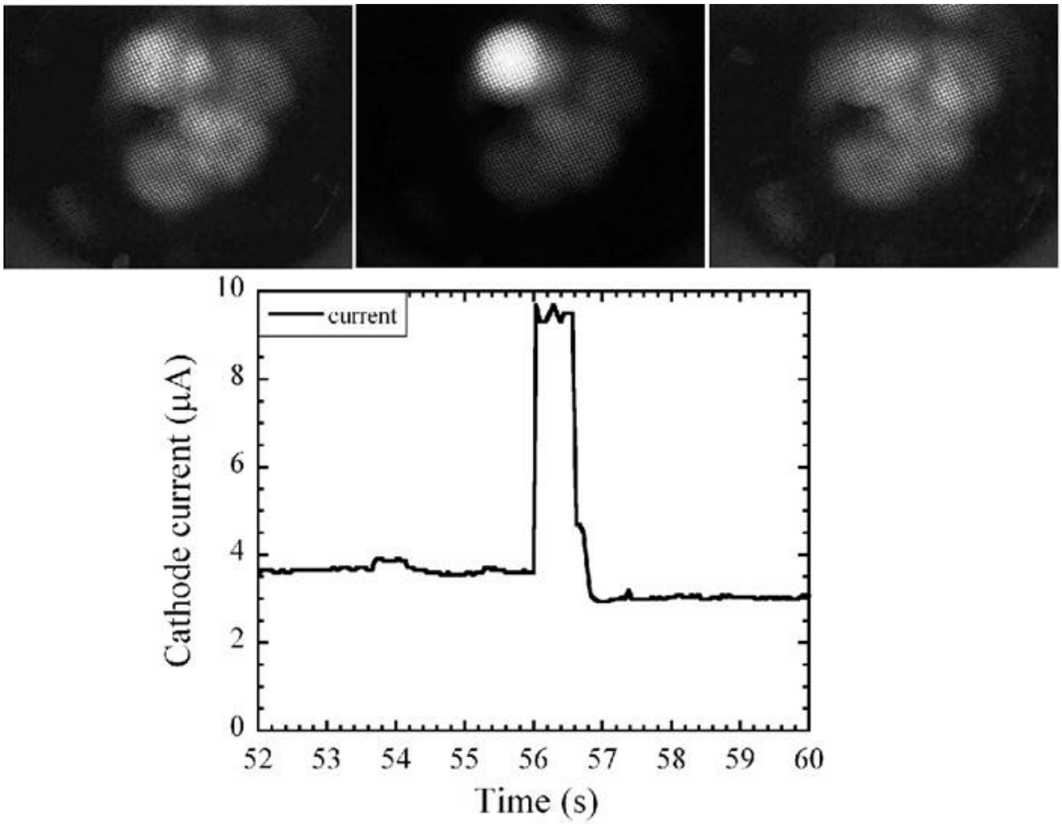

Figure 4-6: Field emission correlated with adsorbate motion on carbon nanotubes.

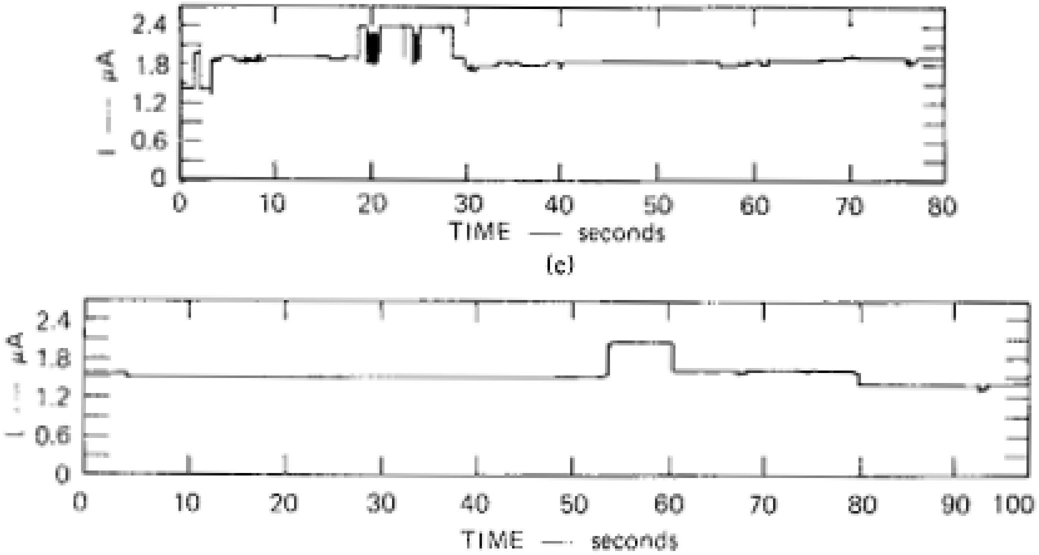

Figure 4-7: Short term current fluctuations as measured by Spindt et al [48]. Spindt did not offer an explanation for this behavior which he referred to as "bistable".

4.4. CORRELATING DIAMOND PROPERTIES THAT CONTRIBUTE TO EMISSION

A diamond field emission array with 100 tips in a 10x10 arrangement has been identified as the first candidate for a correlational study between structure and emission behavior. The array is made up of tips with a nominal 10µm base and 100µm pitch. Approximately half of the tips emitted well when an electric field was applied. Emission measurements and images of this array were performed by Dr. Charlie Brau and Dr. Jonathan Jarvis. The field emission results are visible in Figure 4-8.

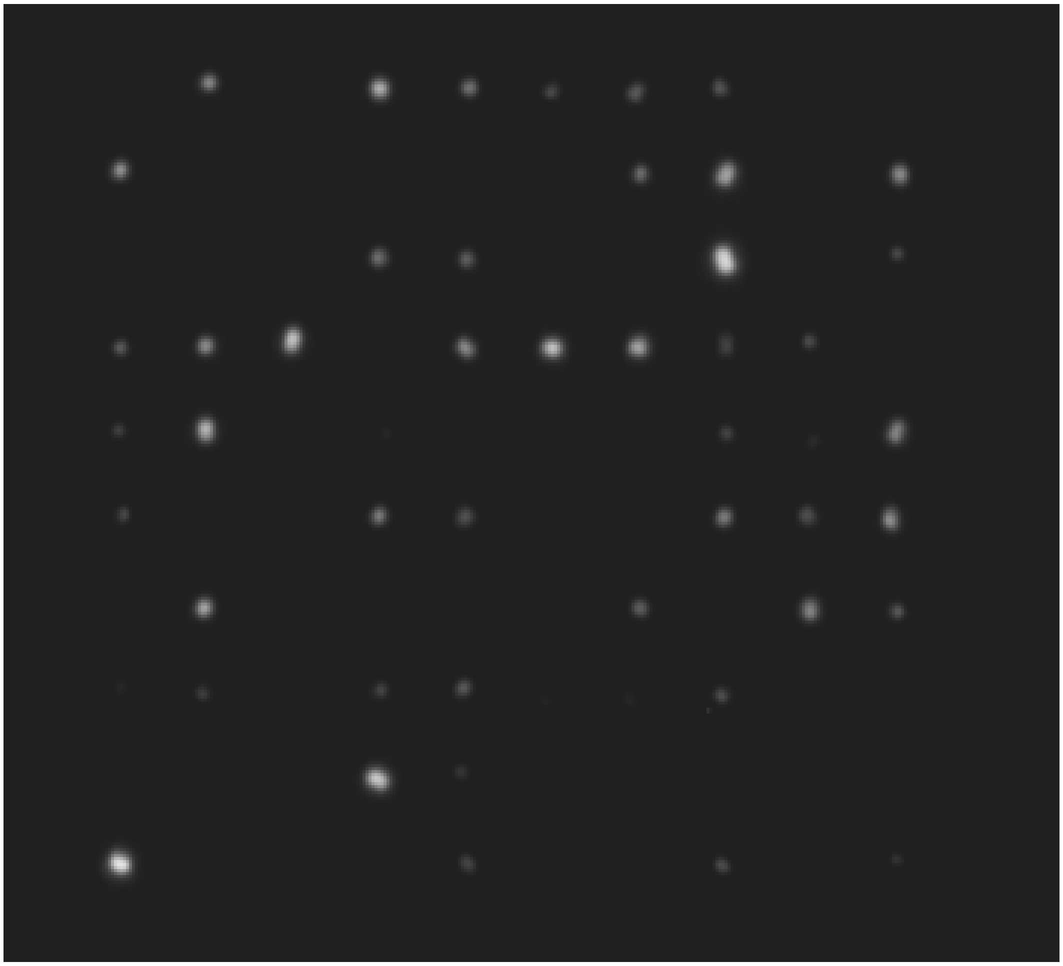

Figure 4-8: Visible light field emission image on phosphor.

All 100 tips were examined by SEM and a number of these have been selected for further examination by TEM. A SEM image of the entire array following emission is shown in Figure

4-9. Higher magnification SEM images of every tip were taken and are aggregated in Figure 4-10.

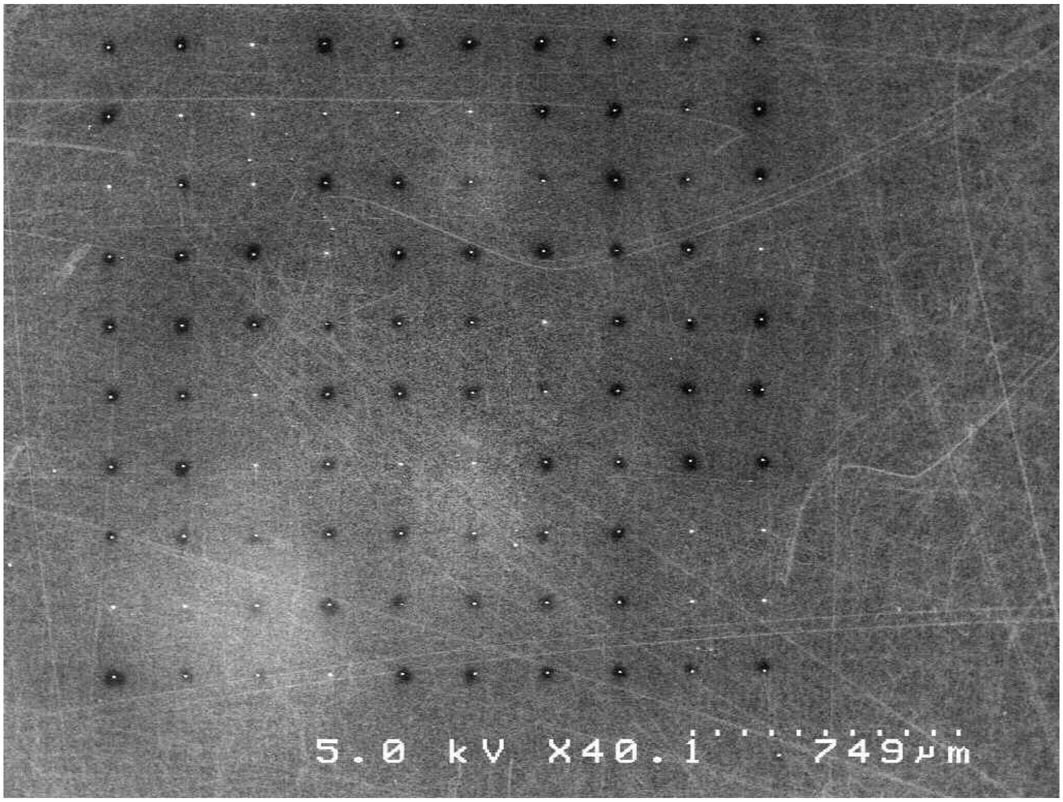

Figure 4-9: SEM image of 10x10 array selected for correlational emission study.

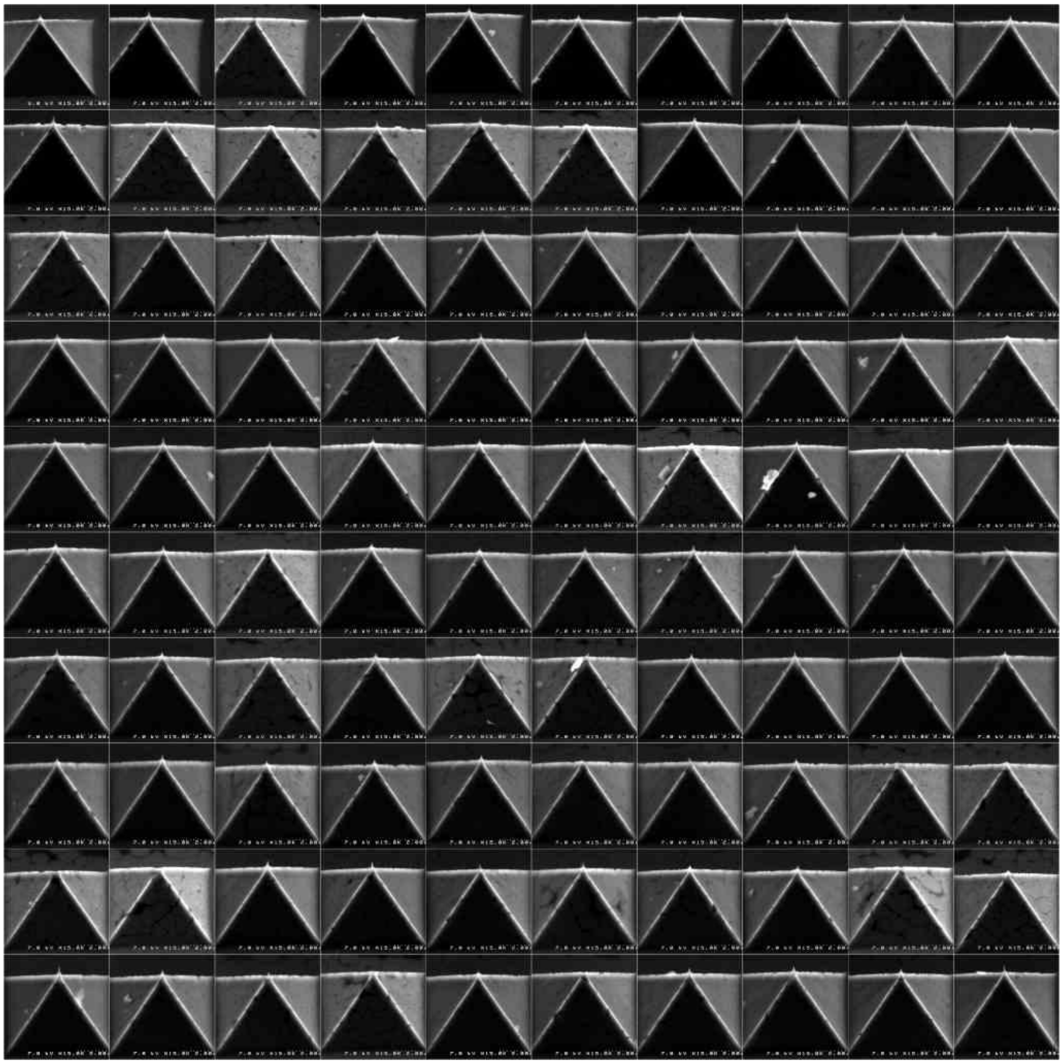

Figure 4-10: Assembled SEM images of 100 field emission tips in an array selected for a correlational study of structure vs. emission current.

It was desirable to examine a combination of tips which failed to emit as expected as well as those that emitted well. Sharp tips which did not emit were especially valued in this examination. Tips selected for further examination are shown in Figure 4-11 through Figure 4-14. Tips 28 and 37 were also selected for further examination, but were lost or destroyed during sample preparation in FIB. Tips 14, 69, and 91 are also interesting and are currently awaiting FIB extraction.

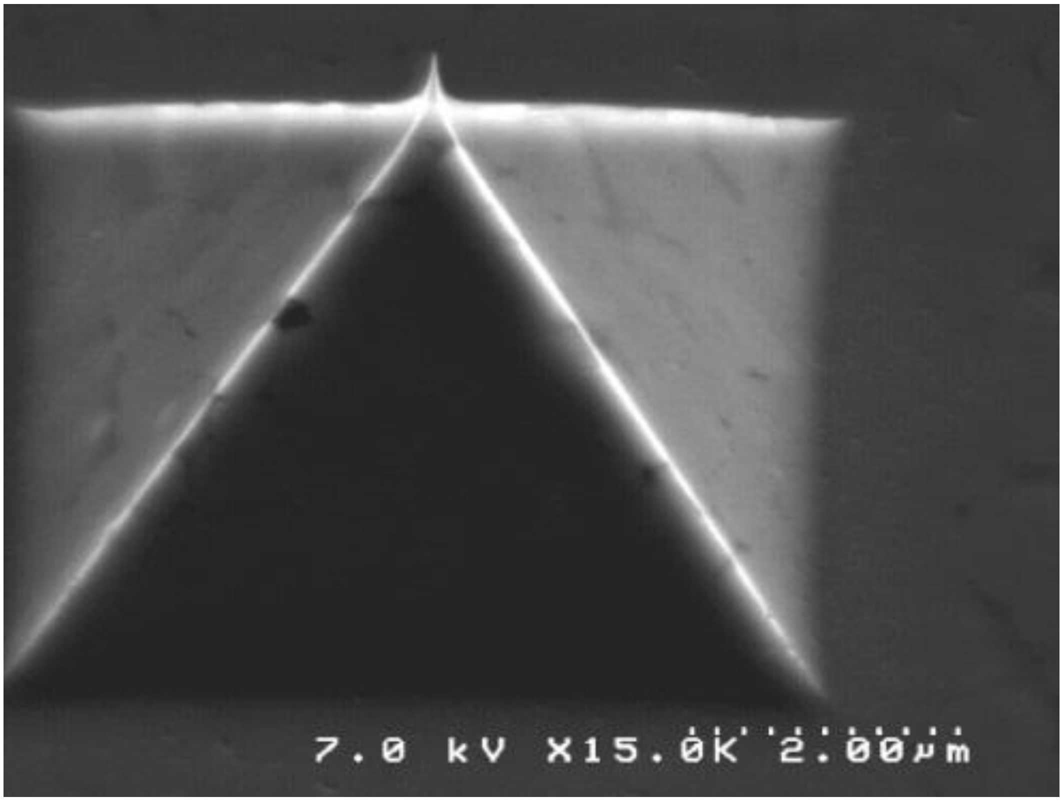

Figure 4-11: Correlational array Tip 2. Bright emission, sharp tip.

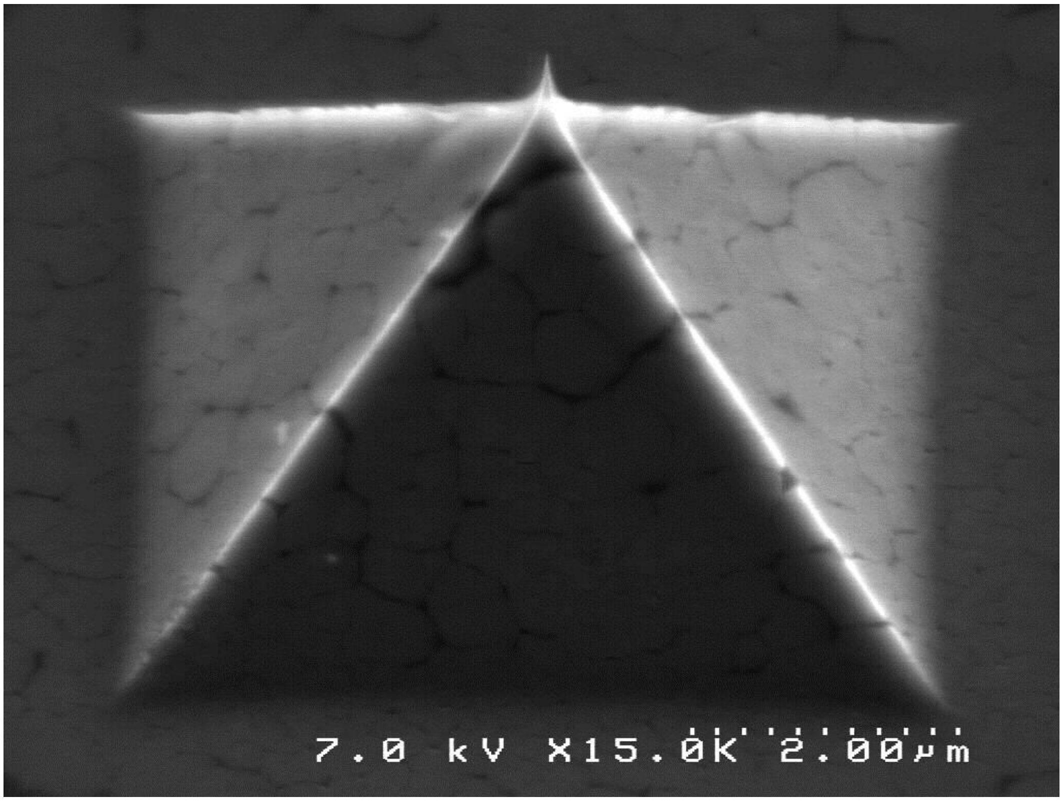

Figure 4-12: Correlational array Tip 15. No emission, sharp tip.

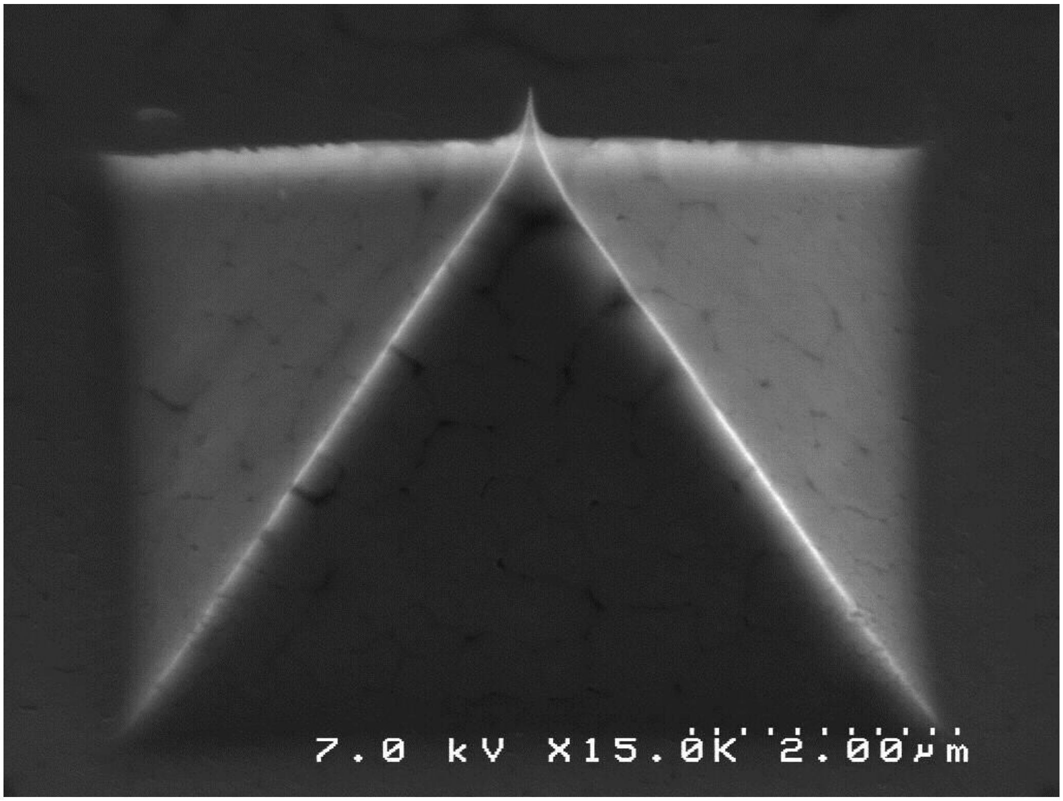

Figure 4-13: Correlational array Tip 27. Some emission, sharp tip.

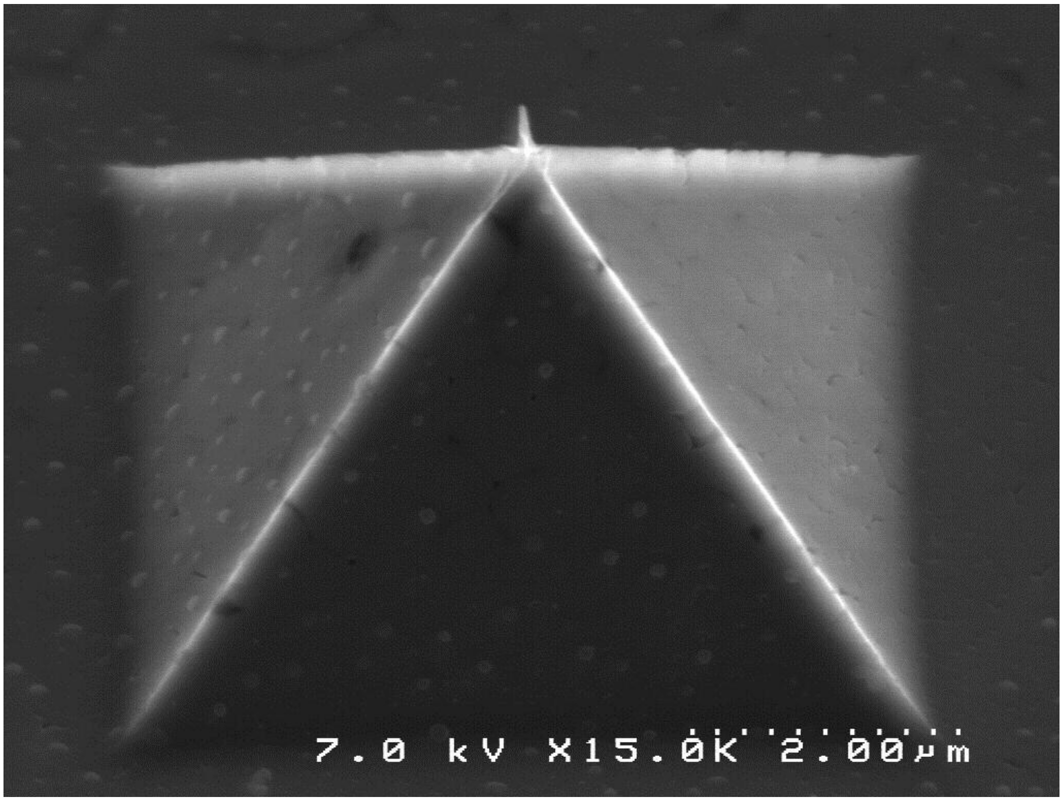

Figure 4-14: Correlational array Tip 84. Very bright emission, reasonably sharp tip.

4.4.1. Tip apex

To date, it appears that geometrical considerations are relevant, if not entirely accurate in predicting tip behavior. Further discussion of comparisons with macro-scale surface features with emission in Section 3.4.1. TEM sample preparation was unable to preserve a sufficient number of tips in order to make an assessment in this regard.

Repeated attempts to preserve the emitter tip apex have proven success very difficult to achieve. In a number of cases, even when the tip appears that it should have been preserved, we see a hollow feature in the protective layer showing where the tip was and should have been. No explanation has been offered to date that explains the apparent preferential milling of the tip material. Even in a worst case scenario in which the tip apex is nothing more than amorphous carbon, there is no reason to expect it to be milled preferentially to the amorphous carbon protective layer.

4.4.2. *Grain boundaries + grain size*

Many previous publications have addressed the role of graphitic boundaries in polycrystalline diamond as a possible conduction path [53, 57, 102, 103, 106, 107, 109, 116].

Ultrananocrystalline diamond (UNCD) films 0.1–2.4 μm thick were conformally deposited on sharp single silicon emitters by Krauss et al. [128], using microwave CH_4–Ar plasma-enhanced chemical vapor deposition. Field emission studies exhibited stable, extremely high (60–100 μA/tip) emission current. Quantum photo-yield measurements of the UNCD films revealed that these films have an enhanced density of states within the bulk diamond band gap that is correlated with a reduction in the threshold field for electron emission. Scanning tunneling microscopy studies indicate that the emission sites from UNCD films are related to minima or inflection points in the surface topography, and not to surface asperities. These data indicate that grain boundaries play a critical role in the electron emission properties of UNCD films, such that these boundaries: (a) provide a conducting path from the substrate to the diamond–vacuum interface, (b) produce a geometric enhancement in the local electric field via internal structures, rather than surface topography, and (c) produce an enhancement in the local density of states within the bulk diamond band gap [128].

Also compelling are the results of Yamada et al. [116] who constructed single crystalline diamond tips of similar dimensions to the CVD pyramidal tips of our own creation (procedures discussed in Section 3.2.4). Since the Yamada cathode does not contain grain boundaries and yet emits similarly, graphitic grain boundaries cannot be the only mode of electron conduction in diamond.

The SEM images in Figure 4-15 and Figure 4-16 shows the range of grain sizes apparent to SEM inspection. TEM studies of these tips indicate that these apparent dark grain boundaries are, in fact, small voids between grains. Such voids appear to be the result of insufficient nucleation density in the nanodiamond layer. As individual nucleation points grow in size during CVD, they grow dendritically. If the space between two nucleation points is large, then the surface between them can be occluded from the CVD plasma media by the adjacent growth.

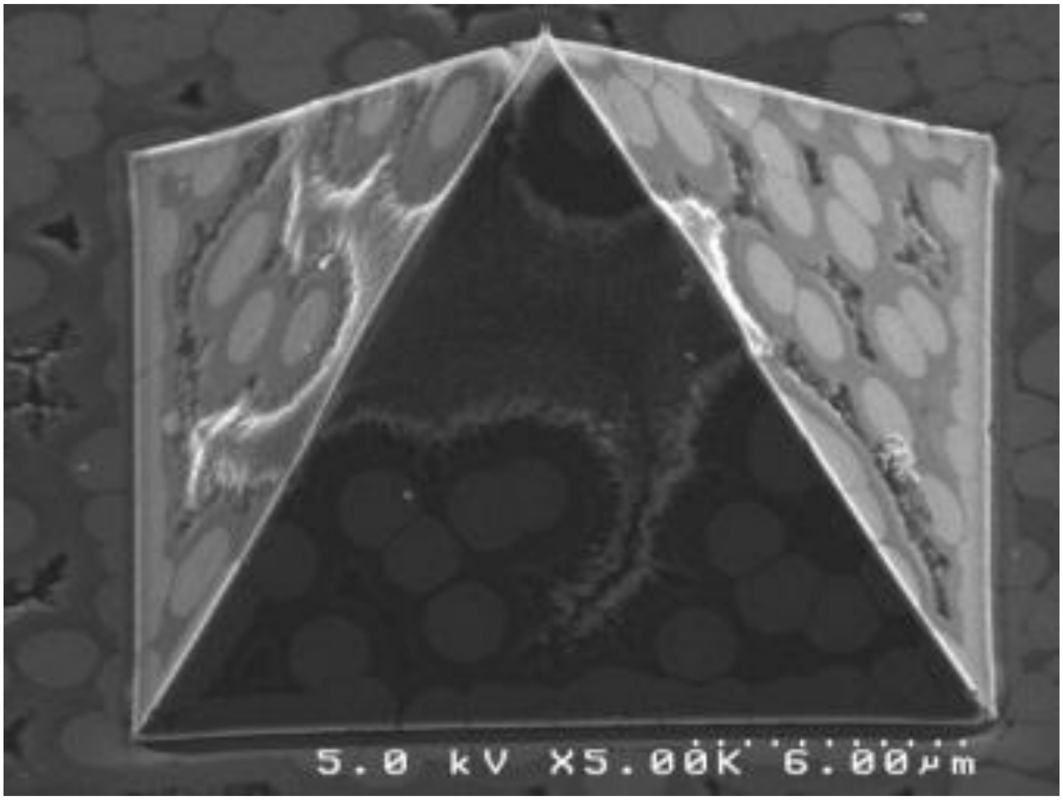

Figure 4-15: SEM image of a diamond field emitter tip made up of large nucleation colonies correlated with a low nucleation density during growth.

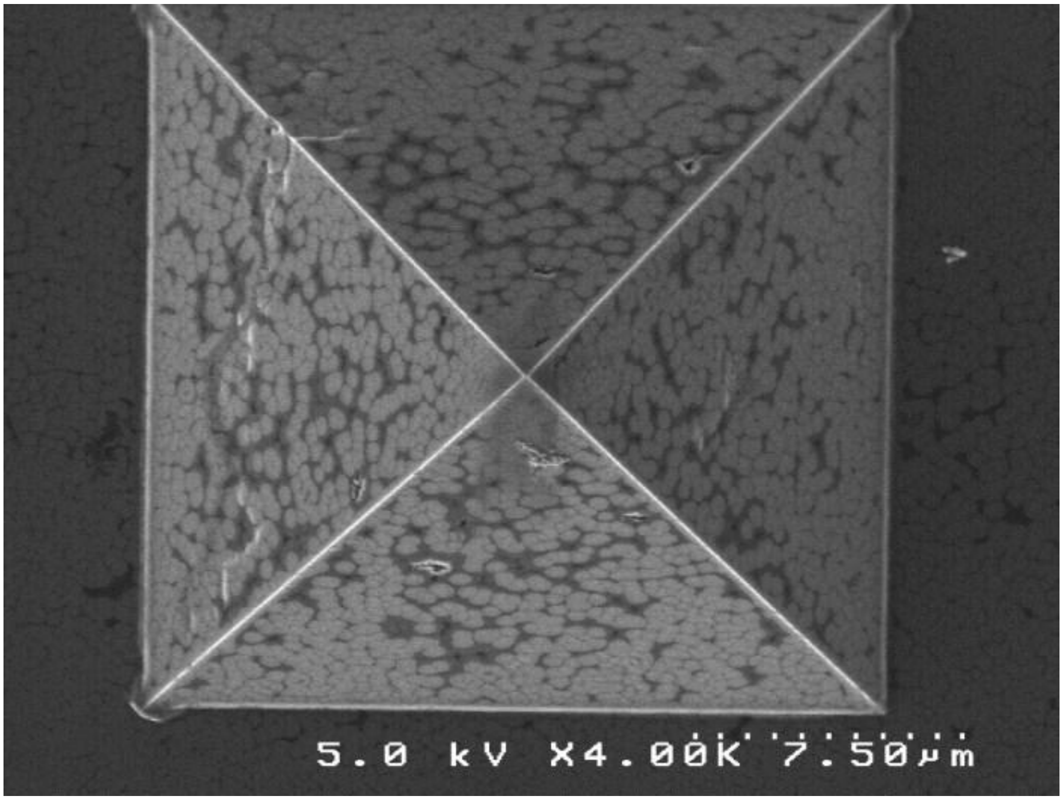

Figure 4-16: SEM image of a diamond field emitter tip (plan-view) made up of many small nucleation colonies associated with a high nucleation density during growth.

In Figure 3-44 on page 97, we see that a high nucleation density results in a tightly textured surface made up of small grains and very narrow grain boundaries between them. Grains that make contact with other grains early in the deposition process do not become large enough to occlude the nearby surface from growth and result in a uniform surface texture lacking the voids associated with low nucleation density [129].

Since the role of grain boundaries is an open question, the presence and quantity cannot be taken to be a direct indicator of the tip's emission characteristics. Indeed, the presence of wide grain boundaries that we now know to be voids in the surface layer most certainly has a deleterious effect on the field emission current. Isolated wide grain boundaries have been observed in bright field emission tips with no apparent effect, but their presence in greater numbers may be a factor.

4.4.3. Surface graphite

Graphite has been observed in early samples at the surface of various tips discussed in Section 3.6. It has not yet been made clear whether the graphite is the result of gallium bombardment during early FIB extraction or if it is a real feature. Sergey Rubanov at the University of Melbourne has stated confidently that gallium amorphizes diamond and cannot graphitize it. It is possible and rather likely that damaged diamond does not reconstruct as graphite, and I have no evidence to the contrary. However, in tips where great care has been taken to protect the tips from gallium, we have not observed surface graphite. In my own observations (Figure 3-41 in Section 3.6.2), cases of known gallium exposure have been directly observed to amorphize diamond. The limited sample size to date prohibits definitive conclusions.

Since we know that graphite has the potential to act as an electrically conductive path in diamond field emitters, the presence of surface graphite may not be a negative thing. Graphitic termination would preclude any arguments for diamond surface dipoles or work function reduction due to diamond surface termination.

4.4.4. Microdiamond excursions to surface

In TEM, low nucleation densities in the nanodiamond layer can leave space for later microdiamond growth to fill in surface features. These microdiamond excursions have not been observed to have a negative effect on field emission. Some emitting tips have been observed to have this feature while it is absent in others. At this time, the presence or absence of a microdiamond excursion region appears to not be a deciding factor regarding the tip's electron emission capabilities. Tip 2 in the 100 tip correlation array (Figure 4-17) has this feature but Tip 84 does not (Figure 4-18). Both were bright electron emitters.

4.4.5. Nucleation Density

Strong field emission results have been observed in tips with even very, very, low nucleation densities. In Figure 4-17, the entire tip is populated by what appear to be only four nanodiamond colonies. Tip 2 was a good emitter in the 100 tip correlational array. Notably, Figure 4-18, which was arguably the brightest emitter in the array did not have the sharpest tip by far. The structure of this tip is unusually uniform lacking the wide grain boundaries, microdiamond excursions, voids, or apparent change in tip material seen in other tips. There is one visible nucleation colony boundary visible in the upper right of the emitter, but uniformity is otherwise excellent. A very bright emitter that does not possess the geometric advantage of an extremely sharp tip is perhaps the best model for examination of subsurface structure.

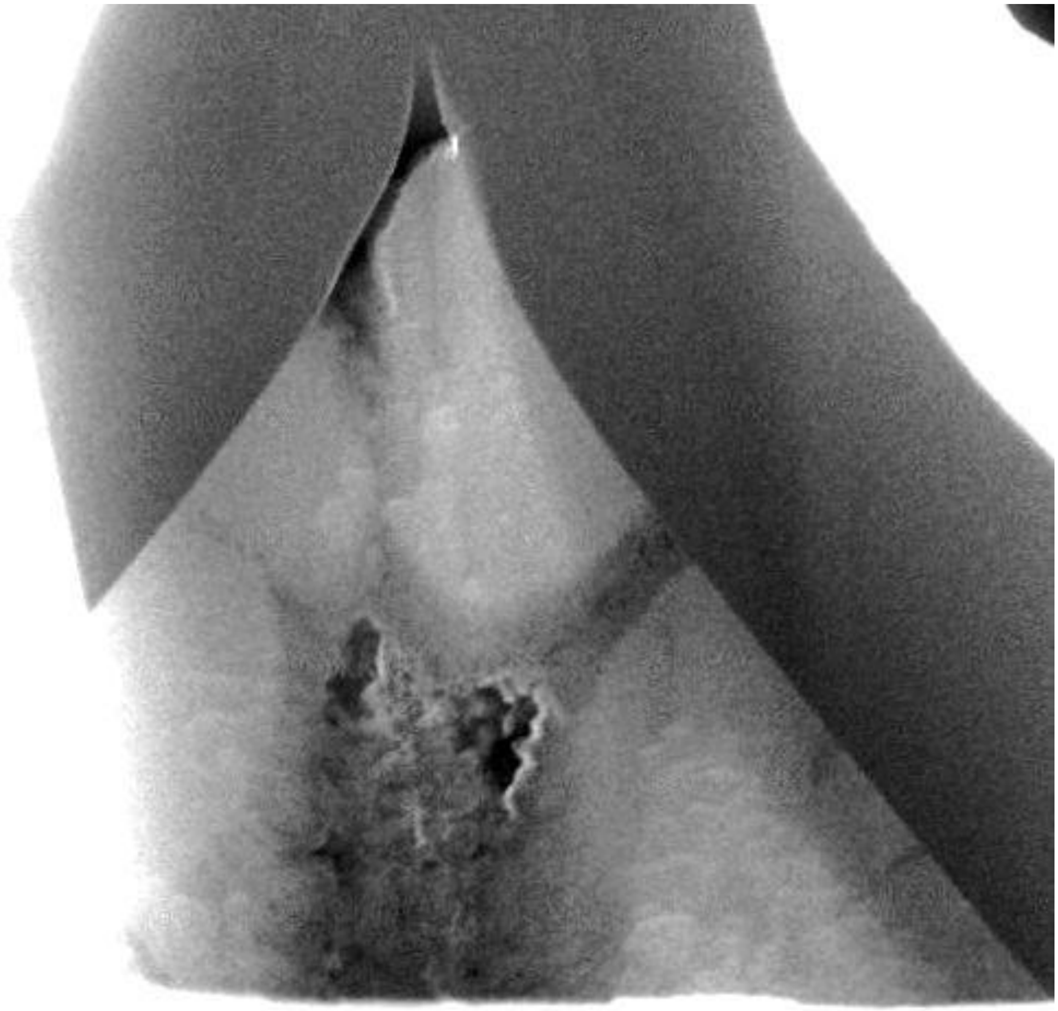

Figure 4-17: TEM image from 100 tip correlational array, Tip 2. The apex appears to be missing, and we observe very large nanodiamond nucleation colonies.

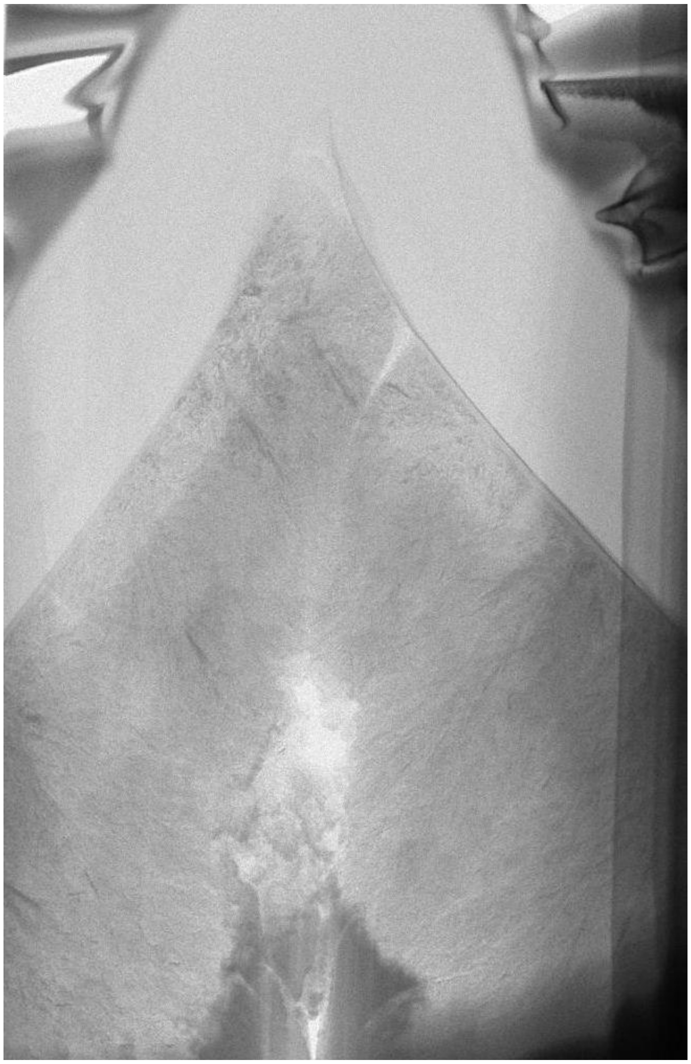

Figure 4-18: TEM image from 100 tip correlational array, Tip 84. The apex was lost due to uneven FIB thinning. Nucleation density is low, but diamond growth in the tip is very uniform with even contrast. Tip SEM images indicate that this tip was less sharp than others (Figure 4-14), but it was one of the very brightest tips in the array. Note the uniformity of contrast and lack of large internal voids.

4.4.1. Graphite incorporation into microdiamond

TEM examination of diamond field emitters has revealed that in some tips, particularly those which have been associated with poor emission properties, have a high graphite content in the microdiamond core. The microdiamond growth parameters are intended to produce large, fast-growing, conductive diamond grains and should not incorporate graphite in large quantities. This observation was first prompted by observing a dramatic density difference between the microcrystalline and nanocrystalline layers. Contrast in the TEM is very sensitive to changes in atomic mass, or lacking that, atomic density. Given that graphite is a lower density material than diamond, regions of lower density were thought to contain higher levels of graphitic content. High magnification investigation of this confirmed our suspicions. Figure 3-50 and Figure 4-19 show this feature. Figure 4-19 is a High Angle Annular Dark Field (HAADF) TEM image in which bright features indicate high atomic mass and high density and vice versa. The inner microdiamond layer clearly shows a lower density than the nanodiamond layer.

Figure 4-19: HAADF TEM of a tip with high contrast observed between the microdiamond and nanodiamond layers which was observed by TEM to correspond to increased graphitic content in the microdiamond layer.

High magnification TEM images of the nanodiamond and microdiamond regions confirm our thoughts on density correlating to material makeup. These features were most evident in the bright field (BF) images. In Figure 4-20, we see the microdiamond region with a substantial amount of incorporated graphite. The graphite is identifiable by two features. First, graphite has a wider spacing between lattice fringes as compared to diamond. Secondly, graphite features often curve, which is not a feature that we ever see in crystalline diamond. Amorphous carbon, when present, does not show lattice fringes. The inset image shows where in the tip this image was taken.

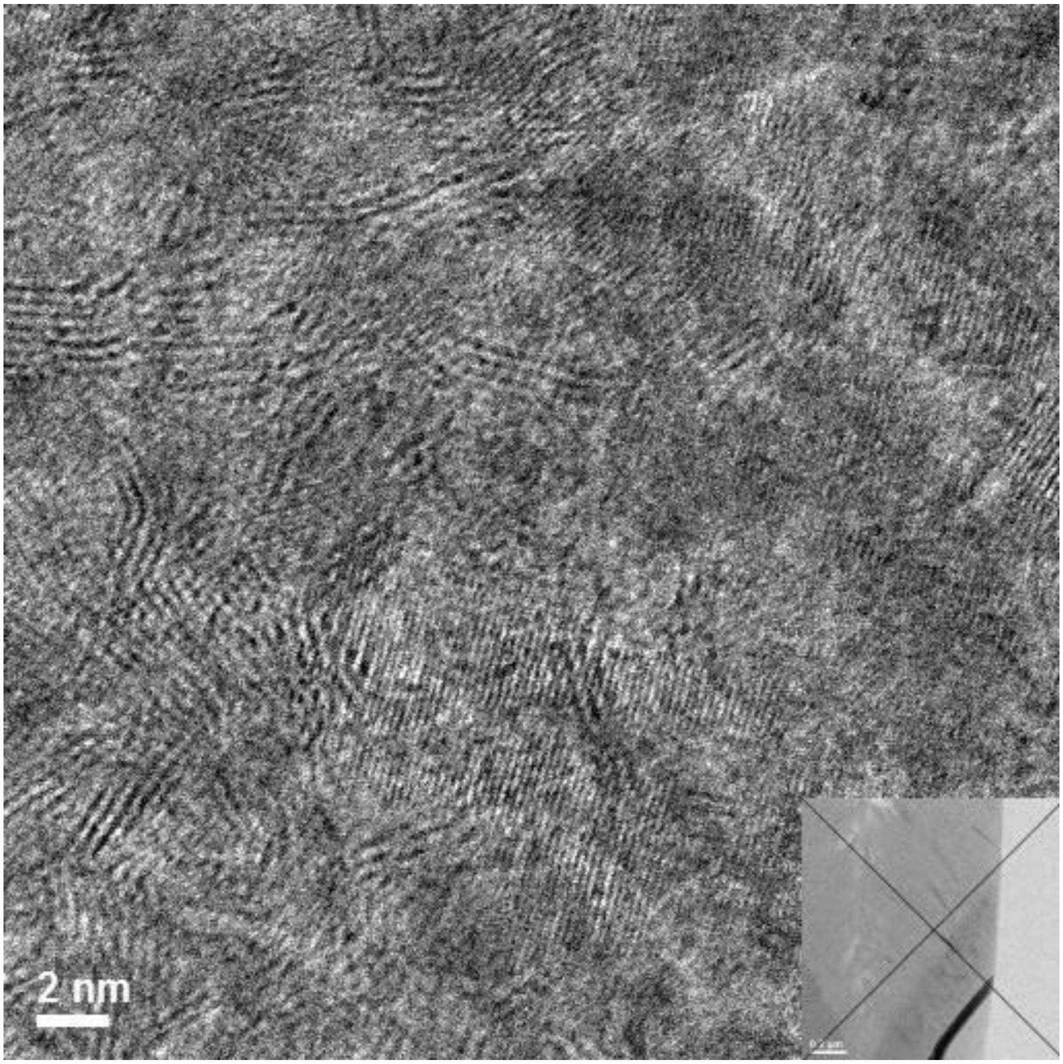

Figure 4-20: High magnification BF TEM image of the microdiamond region of a field emitter tip. The inset image shows an X where this image was taken.

In Figure 4-21, we are looking at a BF TEM image of the nanodiamond region of the tip. Here, we note many locations that show the characteristic lattice fringes associated with diamond, but none of the wider spacing associated with graphite. We note many small grains of various orientations. Again, the inset image shows where this high magnification image was taken. The dark region to the right edge of the image is the protective EBID platinum layer. It is worthwhile to note in this case that we do not observe any amorphized region of diamond at the interface, which indicates that the processing parameters used here have not disturbed/damaged the surface.

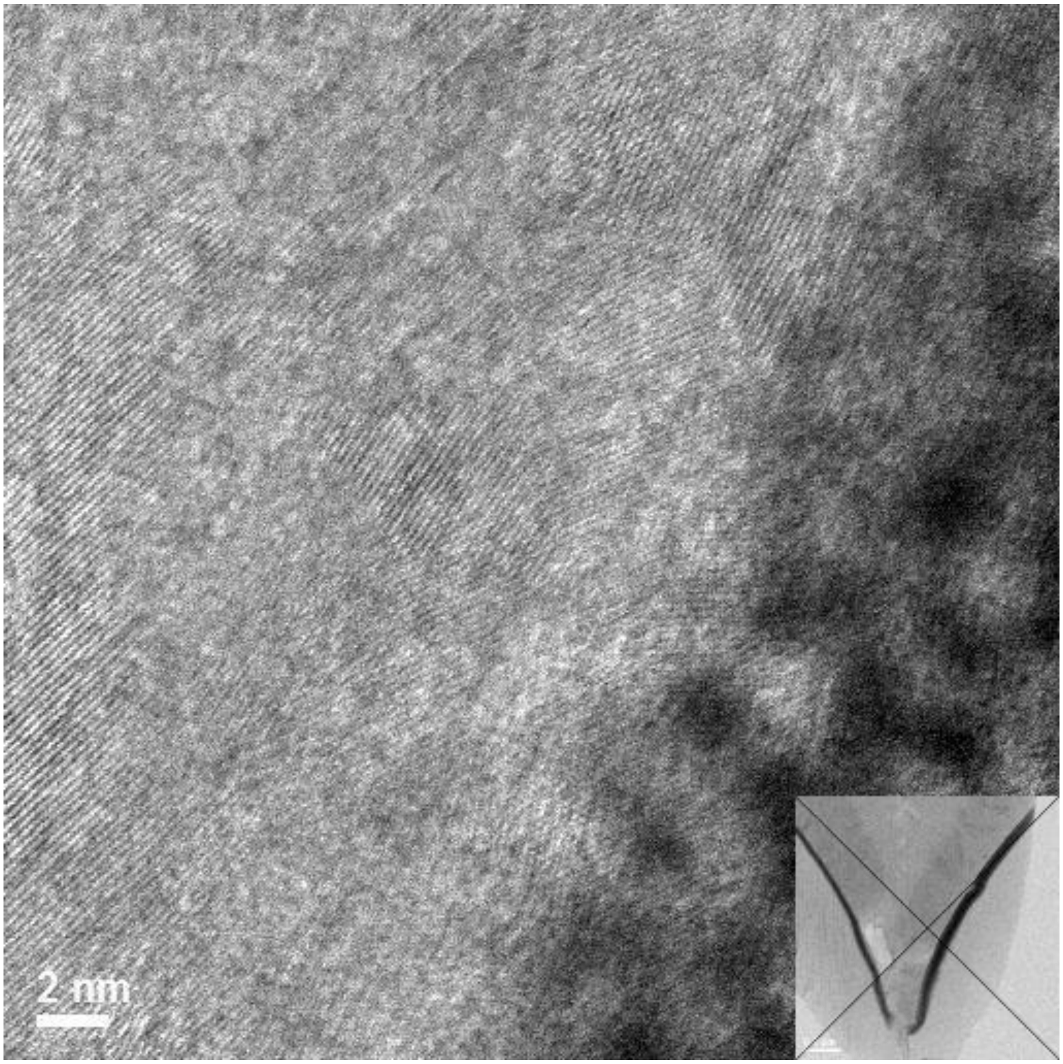

Figure 4-21: High magnification BF TEM image of the nanodiamond region of a field emitter tip. The inset image shows an X where this image was taken.

CHAPTER 5

SUMMARY AND CONCLUSIONS

5.1. SUMMARY

This work addresses a need to understand electron conduction and emission in nanocrystalline diamond tips since they have shown exceptional potential as field emitters. Irregularities in emission behavior between tips were historically attributed to morphological anomalies in the fabrication process: “sharp” vs. “less sharp” tips. However, differences are observed in electron emission thresholds between tips that appear to be equally well formed. By enabling a quantitative analysis of the surface and sub-surface diamond, the methods developed here permit analysis of the diamond growth and provide a feedback procedure for optimization of field emitter properties.

Diamond field emitter arrays have demonstrated tremendous potential and are being actively examined for applications as diverse as wound treatment and more efficient HD televisions to a high power cathode for defensive lasers mounted on surface combat ships. Extended emission tests with diamond arrays have shown lifetimes in excess of 300 hours (Section 3.4.2 and 3.4.3). Decay of emission current over time has been demonstrated to be completely reversible and not associated with macroscopic changes in tip structure. Commercial and military application of these very promising diamond arrays has been hindered by sporadic issues with fabrication yield.

For the first time, cross-sectioned diamond cold cathode field emitters have been imaged by transmission electron microscopy. Diamond has shown itself to be a challenging material to prepare for TEM. Even brief, low-fluence exposure to a gallium ion beam is demonstrated to amorphize the surface. After years of attempting to examine the field emission tip, a method has been developed which has proven successful in preservation of the nanoscale features of interest. Through careful sample preparation, the use of electron beam induced deposition (EBID) of prophylactic materials, a dual-beam FIB, and an argon NanoMill, artifact-free surfaces and nanoscale structures are explored in detail not previously available.

To date, I have observed that the tip apex is not of the same nature as the rest of the tip, as the preservation of that material has proven especially difficult (Section 4.4.1). Naturally, it is a challenge to preserve a nominally 10 nm feature within the ~80 µm cross-sectional lamella being removed. However, even in cases where there is every indication that the proper alignment of the lamella has been achieved, the tip apex has appeared as a hollow in the mold, or as a shadow of what was expected. Given the ease of its destruction, I have come to the conclusion that it is made of some “softer” material than the nanodiamond that supports it. A tip of low-density amorphous carbon is the softest material envisioned, but even this has been ruled out through the observation that an amorphous carbon EBID layer is not removed preferentially and is effective in preserving the region in which the tip formerly existed. The closest I have gotten is shown in Figure 3-33 in which a 40 nm tip feature was preserved and found to be of nanodiamond with a graphitic surface termination. Figure 3-42 provided the most tantalizing look at the emitter tip, but turned out on close inspection to be only a negative depression in the protective layer where a tip should have been.

Field emitters with substantial graphitic content in the sub-surface bulk have been observed (Section 4.4.2) to emit well. Other observations of strongly emitting tips have not shown this feature. Due to a limited number of samples to date, it is unknown whether this is a positive, negative, or inconsequential property. Graphite content is a straightforward function of the growth recipe used. It is one of the more easily manipulated characteristics within the diamond field emitter growth process.

The presence of graphite at the emitter surface has been conclusively observed in some cases and ruled out in others (Section 4.4.3). Graphitic surface termination has not been observed to date in tips for which emission data is available. The presence of graphitic surfaces has important implications for the operation and fabrication of these tips depending on whether it is eventually deemed to be a positive of negative attribute. By virtue of the many publications supporting the theory and some firsthand emission observations in agreement, the surface termination of the tip is of critical importance. Whether adsorbate motion on the surface or the reconstructed surface itself is the dominant factor, the presence of a graphitic termination layer is expected to play a pivotal role.

In tips with a very low nucleation density and incomplete filling of the mold, we have seen regions where the following microdiamond growth stage fills in those voids left open in previous growth steps (Section 3.6.4 and 4.4.4). The preliminary data presented here indicates that the presence of these microdiamond excursions does not appear to be a major factor in emission as some emitting tips have been observed to have this feature while it is absent in others. While too early to determine if this is a trend, the best emitting tip examined to date shows very uniform filling of the mold during the nanodiamond growth and minimal contrast with the microdiamond layer. In this case, internal voids are minimized and graphite content is less abundant as compared to other tips.

The presence of an extremely sharp tip has been shown to be a poor indicator of emission behavior. Examples have been found where both sharp tips do not emit and less sharp tips emit very well. Tips that appear mangled or badly deformed are also sometimes observed to emit well under low fields. Among cross-sectioned tips for which emission data is available, the tip which most closely represented our thoughts of an “ideal” tip geometry was not an exemplary emitter when compared to less “ideal” tips. SEM observations of dark (electrically conductive) field emitter tips seem to correlate well with field emission results (Section 4.2). An SEM-based evaluation of an array attempting to predict its emission behavior would be advised to pay special attention to the apparent contrast differences at the field emitter tip. A tip which appears dark under SEM is a positive attribute. Sharp tips under SEM that have appeared bright in contrast to the tip base have been observed to consistently be poor emitters.

5.2. FUTURE WORK

With the establishment of an effective method for examining previously inaccessible structural information, additional investigations of the correlation between emitter structure and its electron emission properties are underway to identify those structural differences most relevant to electron field emission. Comparison of the nanostructure of emitter tips with variation in field emission characteristics will provide further insight into the influence of the nanocrystalline structure on the electronic properties. Continuation of the correlational studies discussed in this work offer the most obvious and immediate benefit from the preliminary data presented in this work. These measurements provide useful guidelines for future research to further correlate observed structural features with emission behavior.

The newfound ability to preserve the diamond surface for TEM study extends our research capability in ways unrelated to cold cathode field emitters. The study of defect density in diamond being performed by Dr. Tolk's group is correlating implanted defects in single crystal diamond with observations of coherent acoustic phonon (CAP) generation. They have observed that oscillations in laser light reflecting from these acoustic phonons lends information about the transient structure of the material. TEM work is planned to physically extract the damaged diamond region and correlate its observed structural changes to features observed in the CAP signal. In this application, preservation of the sample surface is not of such importance as in the cold cathode study, but accurate knowledge of its location is important to correlate the depth profile of defects.

REFERENCES

1. Cohen, M.L., *Calculation of bulk moduli of diamond and zinc-blende solids.* Physical Review B, 1985. **32**(12): p. 7988.
2. Yin, L.W., Li, M.S., Liu, Y.X., et al., *Synthesis of beta carbon nitride nanosized crystal through mechanochemical reaction.* J. Phys. Condens. Matter, 2003. **15**: p. 309-314.
3. Donnet, C., *Recent progress on the tribology of doped diamond-like and carbon alloy coatings: a review.* Surface & Coatings Technology, 1998. **100**(1-3): p. 180-186.
4. Ali, E. and Christophe, D., *Tribology of diamond-like carbon films: recent progress and future prospects.* Journal of Physics D: Applied Physics, 2006. **39**(18): p. R311.
5. Robertson, J., *Diamond-like amorphous carbon.* Materials Science and Engineering: R: Reports, 2002. **37**(4-6): p. 129-281.
6. Krauss, A.R., Auciello, O., Gruen, D.M., et al., *Ultrananocrystalline diamond thin films for MEMS and moving mechanical assembly devices.* Diamond and Related Materials, 2001. **10**(11): p. 1952-1961.
7. Erdemir, A., *The role of hydrogen in tribological properties of diamond-like carbon films.* Surface and Coatings Technology, 2001. **146-147**: p. 292-297.
8. Touhara, H. and Okino, F., *Property control of carbon materials by fluorination.* Carbon, 2000. **38**(2): p. 241-267.
9. Keyes, R.W., *Figure-of-merit for semiconductors for high speed switches.* Proc. IEEE, 1972. **60**.
10. Collins, A.T. and Lightowlers, E.C., *The Properties of Diamond*, ed. J.E. Field. 1979, San Diego: Academic Press.
11. Shenai, K., Scott, R.S., and Baliga, B.J., *Optimum Semiconductors for High Power Electronics.* IEEE Transactions on Electron Devices, 1989. **36**.
12. Geis, M.W., Efremow, N.N., Woodhouse, J.D., et al., *Diamond cold cathode.* Electron Device Letters, IEEE, 1991. **12**(8): p. 456-459.
13. Trew, R.J., Yan, J.B., and Mock, P.M., *The potential of diamond and SiC electronic devices for ... and millimeter-wave power applications.* Proc. IEEE, 1991. **79**.
14. Buberman, G.S., *The Band Structure of Diamond.* Soviet Physics Uspekhi, 1971. **14**(2).
15. Herman, F., Kortum, R.L., and Kuglin, C.D., *Energy band structure of diamond, cubic silicon carbide, silicon, and germanium.* International Journal of Quantum Chemistry, 1967. **1**(S1): p. 533-566.
16. Kajihara, S.A., Antonelli, A., and Bernholc, J. in *Diamond, Silicon Carbide, and Related Wide Bandgap Semiconductors*. 1990: Material Research Society.
17. Lazea, A., Barjon, J., DHaen, J., et al., *Incorporation of phosphorus donors in (110)-textured polycrystalline diamond.* Journal of Applied Physics, 2009. **105**(8): p. 083545.
18. Landstrass, M.I. and Ravi, K.V., *Resistivity of chemical vapor deposited diamond films.* Applied Physics Letters, 1989. **55**(10).
19. Albin, S. and Watkins, L., *Current-voltage characteristics of thin film and bulk diamond treated in hydrogen plasma.* IEEE Electron Device Letters, 1990. **11**(4): p. 159-161.
20. Davis, R.F., *Diamond Films and Coatings: Development, Properties, and Applications*. 1993, Park Ridge, NJ: Noyes Publications. 429.
21. Noda, T., Araki, H., Suzuki, H., et al., *Isotopic effect on thermal conductivity of diamond thin films.* Materials Transactions, 2005. **46**(Compendex): p. 1807-1809.

22. Ward, A., Broido, D.A., Stewart, D.A., et al., *Ab initio theory of the lattice thermal conductivity in diamond.* Physical Review B, 2009. **80**(12): p. 125203.
23. Novikov, N.V., Podoba, A.P., Shmegera, S.V., et al., *Influence of isotopic content on diamond thermal conductivity.* Diamond and Related Materials, 1999. **8**(8-9): p. 1602-1606.
24. Callaway, J., *Model for Lattice Thermal Conductivity at Low Temperatures.* Physical Review, 1959. **113**(4): p. 1046.
25. Ono, A., Baba, T., Funamoto, H., et al., *Thermal Conductivity of Diamond Films Synthesized by Microwave Plasma CVD.* Japanese Journal of Applied Physics, 1986. **25**(10): p. 808-810.
26. Herb, J.A., Bailey, C., Ravi, K.V., et al. in *First International Symposium on Diamond and Diamond-like Films*. 1989. Pennington, NJ: Electrochemical Society.
27. Seitz, R., *Laser systems with Diamond Optical Elements*, U.P. Office, Editor. 1975: USA.
28. Schumann, W., *Gemstones of the World, 4th Ed*. 4th ed. 2009. 272.
29. Bundy, F.P., *Direct Conversion of Graphite to Diamond in Static Pressure Apparatus.* Science, 1962. **137**.
30. Bundy, F.P., *Melting Point of Graphite at High Pressure: Heat of Fusion.* Science, 1962. **137**(3535): p. 1055-1057.
31. Bovenkerk, H.P., Bundy, F.P., Hall, H.T., et al., *Preparation of diamond.* Nature, 1959. **184**.
32. Yamaoka, S., Komatsu, H., Kanda, H., et al., *Growth of diamond with rhombic dodecahedral faces.* Journal of Crystal Growth, 1977. **37**.
33. DeCarli, P.S. and Jamieson, J.C., *Formation of diamond by explosive shock.* Science, 1961. **133**(3447).
34. Wentorf, R.H.J., *The Behavior of Some Carbonaceous Materials at Very High Pressures and High Temperatures.* Journal of Physical Chemistry, 1965. **69**(9): p. 3063-3069.
35. Wentorf, R.H.J., *Diamond Growth Rates.* Journal of Physical Chemistry, 1971. **75**(12): p. 1833-1837.
36. Strong, H.M. and Chrenko, R.M., *Diamond growth rates and physical properties of laboratory-made diamond.* Journal of Physical Chemistry, 1971. **75**(12).
37. Spear, K.E. and Dismukes, J.P., *Synthetic diamond: emerging CVD science and technology*. 1994, New York, NY: Wiley-Interscience.
38. Zhu, W., *Microwave Plasma Enhanced Chemical Vapor Deposition and Structural Characterization of Diamond Films*, in *Solid State Science*. 1990, Pennsylvania State University: University Park.
39. Zhu, W., Wang, X.H., Badzian, A.R., et al. in *Second International Conference on New Diamond Science and Technology*. 1991. Pittsburgh, PA: Materials Research Society.
40. Haubner, R. and Lux, B., *Effects of microwave plasma deposition parameters on diamond coating formation on SiAlON substrates.* International Journal of Refractory Metals and Hard Materials, 1992. **11**(4).
41. Choi, B.K., Kang, W.P., Davis, I.L., et al., *Thermionic electron emission from chemical vapor deposition diamond by nanosecond laser heating.* Journal of Vacuum Science & Technology B, 2009. **27**(2): p. 557-561.
42. Koeck, F.A.M., Nemanich, R.J., Lazea, A., et al., *Thermionic electron emission from low work-function phosphorus doped diamond films.* Diamond and Related Materials, 2009. **18**(5-8): p. 789-791.

43. Xu, N.S. and Huq, S.E., *Novel cold cathode materials and applications.* Materials Science and Engineering: R: Reports, 2005. **48**(2-5): p. 47-189.
44. Paxton, W.F., Wade, T.C., Howell, M., et al., *Thermionic emission characterization of boron-doped microcrystalline diamond films at elevated temperatures*. 2011, Vanderbilt Univ.
45. Richardson, O.W., *The Electrical Conductivity Imparted to a Vacuum by Hot Conductors*. Phil. Trans. R. Soc. Lond. A, 1903. **201**: p. 497-549.
46. Fowler, R.H. and Nordheim, L., *Electron Emission in Intense Electric Fields.* Proceedings of the Royal Society of London. Series A, Containing Papers of a Mathematical and Physical Character, 1928. **119**(781): p. 173-181.
47. Dyke, W.P. and Trolan, J.K., *Field Emission: Large Current Densities, Space Charge, and the Vacuum Arc.* Physical Review, 1953. **89**(4): p. 799.
48. Spindt, C.A., Brodie, I., Humphrey, L., et al., *Physical properties of thin-film field emission cathodes with molybdenum cones.* Journal of Applied Physics, 1976. **47**(12): p. 5248-5263.
49. Gotoh, Y., Kondo, T., Nagao, M., et al., *Estimation of emission field and emission site of boron-doped diamond thin-film field emitters.* J. Vac. Sci. Tech. B, 2000. **18**(2): p. 1018-1023.
50. Gomer, R., *Field emission and field ionization*. 1961, Cambridge, MA: Harvard University Press.
51. Baumann, P.K. and Nemanich, R.J., *Electron affinity and schottky barrier height of metal-diamond (100), (111), (110) interfaces.* Journal of Applied Physics, 1997. **82**.
52. Wilson, J.I.B., Walton, J.S., and Beamson, G., *Analysis of chemical vapour deposited diamond films by X-ray photoelectron spectroscopy.* Journal of Electron Spectroscopy and Related Phenomena, 2001. **121**(1-3): p. 183-201.
53. Abbott, P., Sosa, E.D., and Golden, D.E., *Effect of average grain size on the work function of diamond films.* Applied Physics Letters, 2001. **79**(17): p. 2835.
54. Diederich, L., Küttel, O.M., Aebi, P., et al., *Electron affinity and work function of differently oriented and doped diamond surfaces determined by photoelectron spectroscopy.* Surface Science, 1998. **418**(1): p. 219-239.
55. Robertson, J., *Electron affinity of carbon systems.* Diamond and Related Materials, 1996. **5**(6-8): p. 797-801.
56. Givargizov, E.I., Zhirnov, V.V., Stepanova, A.N., et al., *Microstructure and field emission of diamond particles on silicon tips.* Applied Surface Science, 1995. **87-88**.
57. Wisitsora-at, A., Kang, W.P., Davidson, J.L., et al., *Efficient electron emitter utilizing boron-doped diamond tips with sp2 content.* Applied Surface Science, 1999. **146**(1-4): p. 280-286.
58. Modinos, A., *Field, Thermionic, and Secondary Electron Emission Spectroscopy*. 1 ed. 1984, New York: Plenum Press. 375.
59. Himpsel, F.J., Knapp, J.A., VanVechten, J.A., et al., *Quantum photoyield of diamond(111)& A stable negative-affinity emitter.* Physical Review B, 1979. **20**(2): p. 624.
60. Van Der Weide, J., Zhang, Z., Baumann, P.K., et al., *Negative-electron-affinity effects on the diamond (100) surface.* Physical Review B, 1994. **50**(8): p. 5803.
61. Diederich, L., Aebi, P., Kuttel, O.M., et al., *NEA peak of the differently terminated and oriented diamond surfaces.* Surface Science, 1999. **424**(2-3): p. L314-L320.

62. Baumann, P.K. and Nemanich, R.J., *Surface cleaning, electronic states and electron affinity of diamond (100), (111), and (110) surfaces.* Surface Science, 1998. **409**: p. 320-335.
63. Baumann, P.K. and Nemanich, R.J., *Negative electron affinity effects and Schottky barrier height measurements of cobalt on diamond (100) surfaces.* Proceedings of the Applied Diamond Conference, 1995. **1**.
64. Bandis, C., Haggerty, D., and Pate, B.B., *Electron emission properties of the negative electron affinity (111) 2x1 diamond TiO interface.* Proc. Material Research Society, 1994. **339**.
65. Pickett, W.E., *Negative electron affinity and low work function surface cesium on oxygenated diamond (100).* Physical Review Letters, 1994. **73**.
66. Koleske, D.D., Gates, S.M., Thoms, B.D., et al., *Hydrogen on polycrystalline diamond films: Studies of isothermal desorption and atomic deuterium abstraction.* J. Chem. Phys., 1995. **102**(2): p. 992-1002.
67. Saparin, G.V., *Microcharacterization of CVD diamond films by scanning electron microscopy: morphology structure and microdefects.* Diamond and Related Materials, 1994. **3**.
68. Lee, W.S., Baik, Y.-J., Eun, K.Y., et al., *Metallographic etching of polycrystalline diamond films by reaction with metal.* Diamond and Related Materials, 1995. **4**.
69. Lin, J.C., Chen, K.H., Chang, H.C., et al., *The vibrational dephasing and relaxation of CH and CD stretches on diamond surfaces: an anomaly.* J. Chem. Phys., 1996. **105**(10): p. 3975.
70. Huang, Z.H., Cutler, P.H., Miskovsky, N.M., et al., *Theoretical study of field emission from diamond.* Applied Physics Letters, 1994. **65**(20).
71. Yamaguchi, H., Saito, I., Kudo, Y., et al., *Electron emission mechanism of hydrogenated natural type IIb diamond (111).* Diamond and Related Materials, 2008. **17**(2): p. 162-166.
72. Zhu, W., Kochanski, G.P., Jin, S., et al., *Defect-enhanced electron field emission from chemical vapor deposited diamond.* Journal of Applied Physics, 1995. **78**(4): p. 2707-2711.
73. Park, K.H., Lee, S., Song, K., et al., *Field emission characteristics of defective diamond films.* Journal of Vacuum Science and Technology B, 1998. **16**(2).
74. Huang, Z.H., Cutler, P.H., Miskovsky, N.M., et al., *A Band-to-band Tunneling Injection Mechanism For Charge Carriers in Composite Wide Bandgap Field Emission Sources.* J. Vac. Sci. Tech. B, 1995. **15**.
75. Reistein, J., Stein, W., and Ley, L., *Defect spectroscopy and determination of the electron diffusion length in single crystal diamond by total photoelectron yield spectroscopy.* Physical Review Letters, 1997. **78**(9).
76. Habermann, T., *Modifying chemical vapor deposited films for field emission displays.* Journal of Vacuum Science & Technology B, 1998. **16**(2).
77. Walter, K.C., Kung, H.H., and Maggiore, C.J., *Improved field emission of electrons from ion irradiated carbon.* Applied Physics Letters, 1997. **71**(10).
78. Wang, C., Garcia, A., Ingram, D.C., et al., *Cold field emission from CVD diamond films observed in emission electron microscopy.* Electronics Letters, 1991. **27**(16): p. 1459-1461.

79. Xu, N.S., Tzeng, Y., and Latham, R.V., *Similarities in the cold electron-emission characteristics of diamond coated molybdenum electrodes and polished bulk graphite surfaces.* Journal of Physics D-Applied Physics, 1993. **26**(10): p. 1776-1780.
80. Humphreys, V.L. and Khachan, J., *Spatial correlation of electron field emission sites with non-diamond carbon content in CVD diamond.* Electron Device Letters, IEEE, 1995. **31**(12).
81. Bobrov, K., Mayne, A.J., and Dujardin, G., *Atomic-scale imaging of insulating diamond through resonant electron injection.* Nature, 2001. **413**(6856): p. 616-620.
82. Saito, T., Kameta, M., Kusakabe, K., et al., *Morphology and semiconducting properties of homoepitaxially grown phosphorus-doped (1 0 0) and (1 1 1) diamond films by microwave plasma-assisted chemical vapor deposition using triethylphosphine as a dopant source.* Journal of Crystal Growth, 1998. **191**(4): p. 723-733.
83. Okano, K., Koizumi, S., Silva, S.R.P., et al., *Low-threshold cold cathodes made of nitrogen-doped chemical-vapour-deposited diamond.* Nature, 1996. **381**(6578): p. 140-141.
84. Robertson, J., Gerber, J., Sattel, S., et al., *Mechanism of bias-enhanced nucleation of diamond on Si*. Vol. 66. 1995: AIP. 3287-3289.
85. Prins, J.F., *n-type semiconducting diamond by means of oxygen-ion implantation.* Physical Review B, 2000. **61**(11): p. 7191.
86. Bhattacharyya, S., Auciello, O., Birrell, J., et al., *Synthesis and characterization of highly-conducting nitrogen-doped ultrananocrystalline diamond films.* Applied Physics Letters, 2001. **79**(10): p. 1441-1443.
87. Koeck, F.A.M. and Nemanich, R.J., *Low temperature onset for thermionic emitters based on nitrogen incorporated UNCD films.* Diamond and Related Materials, 2009. **18**(2-3): p. 232-234.
88. Suzuki, M., Ono, T., Sakuma, N., et al., *Low-temperature thermionic emission from nitrogen-doped nanocrystalline diamond films on n-type Si grown by MPCVD.* Diamond and Related Materials, 2009. **18**(10): p. 1274-1277.
89. Nassau, K., *The Physics and Chemistry of Color*. 1983, New York, NY: Wiley.
90. Prawer, S. and Nemanich, R.J., *Raman spectroscopy of diamond and doped diamond.* Phil. Trans. R. Soc. Lond. A, 2004. **362**: p. 2537-2565.
91. Bragg, W.L., *The Crystalline State, Vol. I,* ed. W.L. Bragg and W.H. Bragg. 1933, London: George Bell and Sons Ltd.
92. Wild, C., Herres, N., and Koidl, P., *Texture formation in polycrystalline diamond films.* Journal of Applied Physics, 1990. **68**: p. 973-978.
93. Kobashi, K., Nishimura, K., Miyata, K., et al. in *First International Symposium on Diamond and Diamond-like Films*. 1989. Pennington, NJ: The Electrochemical Society.
94. Specht, E.D., Clausing, R.E., and Heatherly, L., *Measurement of crystalline strain and orientation in diamond films grown by chemical vapor deposition.* Journal of Material Research, 1990. **5**: p. 2351-2355.
95. Van der Drift, A., *Evolutionary selection, a principle governing growth orientation in vapour-deposited layers.* Philips Research Report, 1967. **22**: p. 267-288.
96. Clausing, R.E., Heatherly, L., Specht, E.D., et al. *Texture Development in Diamond Films Grown by Hot Filament CVD Processes*. in *Second International Conference on New Diamond Science and Technology*. 1991. Pittsburgh, PA: Material Research Society.

97. Meilunas, R., Wong, M.S., Sheng, K.C., et al., *Early Stages of Plasma Synthesis of Diamond Films.* Applied Physics Letters, 1989. **54**(22): p. 2204-2206.
98. Kreigor27 and Wikipedia. *Schematic FIB, Real FIB*. 2009 [cited 2011; Available from: http://en.wikipedia.org/wiki/Focused_ion_beam#Technology.
99. Hill, S.B. and McClelland, J.J., *Atoms on demand: Fast, deterministic production of single Cr atoms.* Applied Physics Letters, 2003. **82**(18): p. 3128-3130.
100. Andrews, K.W., Dyson, D.J., and Keown, S.R., *Interpretation of electron diffraction patterns*. 2nd ed, ed. A. Hilger. 1971, London: Adam Higler LTD. 188.
101. Kang, W.P., Davidson, J.L., Li, Q., et al. *A Novel Low Field Electron Emission Polyerystalline Diamond Microtip Arrays For Sensor Applications*. in *Solid-State Sensors and Actuators, 1995 and Eurosensors IX.. Transducers '95. The 8th International Conference on*. 1995.
102. Kang, W.P., Davidson, J.L., George, M.A., et al., *Characterization of the Microstructure of Diamond Pyramidal Microtip Emitters*, in *International Conference on the New Diamond Science and Technology*. 1996: Tours, France.
103. Kang, W.P., Davidson, J.L., George, M.A., et al., *Physical characterization of diamond pyramidal microtip emitters.* Journal of Vacuum Science & Technology B 1997. **15**(2): p. 460-463.
104. Kang, W.P., Wisitsora-at, A., Davidson, J.L., et al., *Ultralow-voltage boron-doped diamond field emitter vacuum diode.* Ieee Electron Device Letters, 1998. **19**(10): p. 379-381.
105. Kang, W.P., Davidson, J.L., Wisitsora-At, A., et al., *Diamond vacuum field emission devices.* Diamond and Related Materials, 2004. **13**(11-12): p. 1944-1948.
106. Kang, W.P., Davidson, J.L., Wisitsora-at, A., et al., *Diamond and carbon-derived vacuum micro- and nano-electronic devices.* Diamond and Related Materials, 2005. **14**: p. 685-691.
107. Subramanian, K., Kang, W.P., Davidson, J.L., et al., *Enhanced electron field emission from micropatterned pyramidal diamond tips incorporating CH4/H-2/N-2 plasma-deposited nanodiamond.* Diamond and Related Materials, 2006. **15**(4-8): p. 1126-1131.
108. Raina, S., Kang, W.P., and Davidson, J.L., *Field emission from nanodiamond grown with ridge type geometrically enhanced features.* Diamond and Related Materials, 2007. **17**(4-5): p. 790-793.
109. Davidson, J.L., Kang, W.P., Subramanian, K., et al. *Vacuum Cold Cathode Emitter Electronic Devices Comprised of Diamond or other Carbons*. in *University/Government/Industry Micro/Nano Symposium, 2008. UGIM 2008. 17th Biennial*. 2008.
110. Jarvis, J.D., Andrews, H.L., Ivanov, B., et al., *Resonant tunneling and extreme brightness from diamond field emitters and carbon nanotubes.* Journal of Applied Physics, 2010. **108**(9).
111. Birrell, J., Gerbi, J.E., Auciello, O., et al., *Bonding structure in nitrogen doped ultrananocrystalline diamond.* Journal of Applied Physics, 2003. **93**(9): p. 5606-5612.
112. Alves, M.A.R., de Faria, P.H.L., and Braga, E.S., *Current-voltage characterization and temporal stability of the emission current of silicon tip arrays.* Microelectronic Engineering, 2004. **75**(4): p. 383-388.

113. Qi, K.C., Lin, Z.L., Chen, W.B., et al., *Formation of extremely high current density LaB[sub 6] field emission arrays via e-beam deposition.* Applied Physics Letters, 2008. **93**(9): p. 093503-3.
114. Nishibayashi, Y., Ando, Y., Saito, H., et al., *"Nanorods" of single crystalline diamond.* Diamond and Related Materials, 2001. **10**.
115. Hwang, D.S., Saito, T., and Fujimori, N., *New etching process for device fabrication using diamond.* Diamond and Related Materials, 2004. **13**.
116. Yamada, T., Hwang, D.S., Vinod, P.R., et al., *Characterization of field emission from nano-scale diamond tip arrays.* Japanese Journal of Applied Physics Part 2-Letters & Express Letters, 2005. **44**(12-15): p. L385-L387.
117. Lee, H.C. and Huang, R.S., *A theoretical study on field emission array for microsensors.* Electron Devices, IEEE Transactions, 1992. **39**(2): p. 313-324.
118. Ito, T., Nishimura, M., Yokoyama, M., et al., *Highly efficient electron emitting diode fabricated with single-crystalline diamond.* Diamond and Related Materials, 2000. **9**(9-10): p. 1561-1568.
119. Jarvis, J.D., *Personal communication*. 2010.
120. Sommer, A.P., Zhu, D., and Bruhne, K., *Surface Conductivity on Hydrogen-Terminated Nanocrystalline Diamond: Implication of Ordered Water Layers.* Crystal Growth & Design, 2007. **7**(11): p. 2298-2301.
121. Maier, F., Ristein, J., and Ley, L., *Electron affinity of plasma-hydrogenated and chemically oxidized diamond (100) surfaces.* Physical Review B, 2001. **64**(16): p. 165411.
122. Modinos, A., *Field emission from surface states in semiconductors.* Surface Science, 1974. **42**(1): p. 205-227.
123. Geis, M.W., Twichell, J.C., and Lyszczarz, T.M., *Fabrication and Theory of Diamond Emitters.* Lincoln Laboratory Journal, 1995. **8**(2): p. 161-172.
124. Cui, J.B., Ristein, J., and Ley, L., *Electron Affinity of the Bare and Hydrogen Covered Single Crystal Diamond (111) Surface.* Physical Review Letters, 1998. **81**(2): p. 429.
125. Butler, J.E. and Sumant, A.V., *The CVD of nanodiamond materials.* Chemical Vapor Deposition, 2008. **14**(7-8): p. 145-160.
126. Sumant, A.V., Grierson, D.S., Gerbi, J.E., et al., *Surface Chemistry and Bonding Configuration of Ultrananocrystalline Diamond Surfaces and Their Effects on Nanotribological Properties.* Physical Review B, 2007. **76**: p. 235429.
127. Fox, O.J.L., Holloway, J.O.P., Fuge, G.M., et al. *Electrospray deposition of diamond nanoparticle nucleation layers for subsequent CVD diamond growth*. in *Materials Research Society Symposium Proceedings*. 2010.
128. Krauss, A.R., Auciello, O., Ding, M.Q., et al., *Electron field emission for ultrananocrystalline diamond films.* Journal of Applied Physics, 2001. **89**(5): p. 2958-2967.
129. Williams, O.A., Nesladek, M., Daenen, M., et al., *Growth, electronic properties and applications of nanodiamond.* Diamond and Related Materials, 2008. **17**(7-10): p. 1080-1088.